Modeling and Simulation of the Dynamic Behavior of Portable Proton Exchange Membrane Fuel Cells

DISSERTATION

zur Erlangung des akademischen Grades
des Doktors der Naturwissenschaften
(Dr. rer. nat.)
an der Universität Konstanz
Fakultät für Physik

vorgelegt von
CHRISTOPH ZIEGLER

Fraunhofer Institut für Solare Energiesysteme
Freiburg im Breisgau
2005

Tag der mündlichen Prüfung: 21.11.2005
Referent: Priv. Doz. Dr. G. Willeke
Referent: Prof. Dr. P. Leiderer

Zusammenfassung

Die gegenwärtige Entwicklung von miniaturisierten Brennstoffzellen wird wesentlich durch die Möglichkeit angetrieben, höhere Energiedichten im Vergleich zu Batterien und Akkumulatoren zu erreichen. Einleitend werden daher Brennstoffzellen und Batterien miteinander verglichen. Verschiedene Optionen für die Erzeugung und Speicherung von Wasserstoff werden diskutiert.
Der Schwerpunkt dieser Arbeit liegt im Bereich der Modellierung und Simulation von Polymer-Elektrolyt-Membran-Brennstoffzellen. Die mathematische Modellierung von Brennstoffzellen liefert einen wichtigen Beitrag zum Verständnis und zur Weiterentwicklung der Brennstoffzellentechnologie. Wichtige Anwendungsfelder der Brennstoffzellensimulation werden in Kapitel 1 diskutiert.

In Kapitel 2 werden die physikalischen und elektrochemischen Grundlagen hergeleitet, die für die mathematische Beschreibung einer Polymer-Elektrolyt-Membran-Brennstoffzelle notwendig sind. Die elektrochemischen Reaktionen werden mit der Butler-Volmer-Gleichung beschrieben. Am Beispiel der Massenerhaltung wird die Kontinuitätsgleichung eingeführt. Für die Beschreibung der Gasdiffusion werden Ausdrücke zur Beschreibung der binären Diffusion sowie für den Fall der Mehrkomponentendiffusion abgeleitet. Der elektrische Strom in der Brennstoffzelle wird mit Poisson-Gleichungen für Elektronen und Protonen beschrieben. Darüber hinaus werden die Gleichungen für Mehrphasenströmung eingeführt, um die Modellierung des Transportes von flüssigem Wasser in Kombination mit Gastransport vorzubereiten. Die Einführung in die Grundlagen der Brennstoffzellenmodellierung endet mit der Herleitung der Energieerhaltungsgleichung.

Am Fraunhofer Institut für Solare Energiesysteme werden flache selbstatmende Brennstoffzellen in Leiterplattenbauweise entwickelt. Dieser Brennstoffzellentyp ist besonders interessant, da mit der Leiterplattentechnik eine etablierte und kostengünstige sowie robuste und hinsichtlich des Designs flexible Technologie als Plattform dient. Selbstatmende Zellen haben den Vorteil, dass der für die Kathode benötigte Sauerstoff rein diffusiv und nicht gepumpt zur Kathode gelangt. Auf diese Weise kann das Gewicht und das Volumen einer Pumpe einge-

spart werden. Die Geräuschentwicklung wird reduziert und der Systemwirkungsgrad steigt an. Derzeit liegt die typische Leistungsdichte für flache selbstatmende Zellen bei 100 mW/cm^2. Die typische Zellspannung beträgt dabei 0.3 V bis 0.4 V. Um das Betriebsverhalten dieses Zelltyps zu untersuchen, wird ein mathematisches Modell einer flachen selbstatmenden Zelle entwickelt und durch den Vergleich mit Messungen validiert. Das Modell ist zweidimensional und beschreibt ein Symmetrieelement einer flachen Zelle, deren Kathode zu 80% offen ist. Die Mehrkomponentendiffusion der Gase wird berücksichtigt ebenso wie die Kopplungen zwischen Energietransport, Massentransport und den elektrochemischen Reaktionen. Ein Agglomeratmodell wird entwickelt, das die Sauerstoffreduktion in Verbindung mit dem Massentransportwiderstand der porösen Elektrode beschreibt.
Das System gekoppelter partieller Differenzialgleichungen (PDGen) ist in FEMLAB^{TM} implementiert. Für die Diskretisierung der PDGen wird die Galerkin-Finite-Element-Methode verwendet. Das resultierende System nichtlinearer Gleichungen wird mit dem gedämpften Newtonverfahren gelöst.
Zur Validierung des Modells werden die simulierte und die gemessene Strom-Spannungskennlinie miteinander verglichen. Die Leistung von flachen selbstatmenden Brennstoffzellen wird durch die konkurrierenden Effekte von Massentransport und Ladungstransport bestimmt. Insbesondere bei hohen Stromdichten trocknet die Membran-Elektroden-Einheit aus und weist dadurch eine verringerte protonische Leitfähigkeit auf. Bedingt durch die Limitierung des Protonentransportes wird zum Beispiel bei einer Zellspannung von 0.1 V und einer Stromdichte von 730 mA/cm^2 der Katalysator an der Grenzschicht zwischen Membran und Katalysatorschicht neunmal besser genutzt als an der gegenüberliegenden Grenzschicht zwischen Katalysatorschicht und Gasdiffusionsschicht. Nicht nur der Protonentransport, sondern auch der Elektronentransport und der Sauerstofftransport sind wichtig für einen optimalen Betrieb der Katalysatorschicht. Im Falle einer flachen selbstatmenden Zelle mit einer zu 80% offenen Kathode ist die Aktivität der Katalysatorschicht direkt unter den Rändern der Stege in der Kathodenplatte am höchsten. Da die Stege nur 20% der Kathodenfläche bedecken, aber als Stromabnehmer dienen, entsteht eine stark inhomogene Stromdichteverteilung.
Im Betrieb bei kleinen Stromdichten ist die Massentransportlimitierung klein. Daher ist die Verwendung breiter Stege und dünner Gasdiffusionsschichten zu empfehlen. Wenn die Zelle überwiegend im Bereich hoher Stromdichten betrieben wird, sollten die Stege schmal sein, und die Gasdiffusionsschicht sollte einen geringen lateralen Diffusionswiderstand aufweisen. Allerdings sollte die Leitfähigkeit der Gasdiffusionsschicht sehr gut sein, um eine Begrenzung des Ladungstransportes zu vermeiden.

Ein gutes Verständnis der Wasserentstehung und des Wassertransportes in Polymer-Elektrolyt-Membran-Brennstoffzellen ist wichtig, um im Betrieb zuverlässig die Flutung oder Austrocknung der Brennstoffzelle vermeiden zu können.
In Kapitel 4 dieser Arbeit wird daher ein eindimensionales isothermes Modell entwickelt, das den zeitabhängigen Zweiphasentransport in der Brennstoffzelle beschreibt. Neben der Beschreibung der Transportmechanismen im gasförmigen und im flüssigen Zustand werden die elektrochemischen Reaktionen und der Ladungstransport in diesem Modell behandelt. Durch die Kopplung der Zweiphasentransportgleichungen an die Beschreibung der Gasdiffusion und die elektrochemischen Reaktionen wird das Flutungsverhalten der Zelle dynamisch beschrieben. Zusätzlich wird ein Membranmodell entwickelt, das das Schrödersche Paradoxon beschreibt und mit den Zweiphasentransportgleichungen gekoppelt ist.
Das Modell ist in FEMLAB^{TM} implementiert. Die zeitabhängigen PDGen werden hinsichtlich des Ortes mit der Galerkin-Finite-Element-Methode diskretisiert. Durch die Verwendung zeitabhängiger Knotenvariablen erhält man ein System von gewöhnlichen Differenzialgleichungen in der Zeit, das mit dem impliziten Löser ode15s von MATLAB^{TM} gelöst wird.
Das Modell wird durch den Vergleich zwischen Simulationsergebnissen und zeitabhängigen Messergebnissen validiert. Das Anlegen einer periodischen Zellspannung mit einer Periodendauer im Bereich von Minuten führt zu einer Strom-Spannungskurve, die charakteristisch für den Transport flüssigen Wassers in der Zelle ist. Die daraus resultierenden zyklischen Voltammogramme werden simuliert und gemessen. Sowohl in der Simulation als auch im Experiment zeigt sich ein Hystereseeffekt. Die Hysterese wird durch die Akkumulation von Wasser auf der Kathodenseite verursacht. Die Zeitspanne zwischen dem Auftreten der höchsten Stromdichte und dem Maximalwert der Wassersättigung beträgt 70 bis 80 Sekunden. Mit dem mathematischen Modell werden die Frequenzen bestimmt, die charakteristisch für die dynamischen Wassertransportprozesse in der Zelle sind. Der Transport von Wasser in flüssiger Phase durch die Membran kann bei etwa 0.1 Hz beobachtet werden. Bei etwa 1 Hz wird der Wassertransport durch die Gasdiffusionsschicht angeregt. Im Vergleich dazu ist die Gasdiffusion ein schneller Prozess und kann bei etwa 20 Hz beobachtet werden. Die elektrische Impedanz im Zweiphasenregime wird simuliert. Ein Bogen im niederfrequenten Bereich des Spektrums wird durch den Wassertransportwiderstand der Membran verursacht.

Das Fraunhofer Institut für Solare Energiesysteme arbeitet nicht nur an Einzelzellen, sondern auch an Brennstoffzellenstacks für den Einsatz in portablen Geräten. In Kapitel 5 wird ein dynamisches Modell eines Brennstoffzellenstacks entwickelt. Das Modell ist für die Optimierung des Betriebsverhaltens und für den Regelungsentwurf geeignet.
Für die Entwicklung des Stackmodells dienen die Modelle der flachen Zelle aus

Kapitel 3 und das dynamische zweiphasige Modell aus Kapitel 4 als Grundlage. Das Stackmodell berücksichtigt keine Ortsauflösung, und auch die explizite Behandlung des Zweiphasentransportes ist nicht Teil des Modells. Diese Einschränkungen ermöglichen den direkten Vergleich der Lösungsvariablen des Modells mit Messwerten und die Simulation des Stackbetriebs über mehrere Stunden. Das dynamische Modell basiert auf Energie- und Massenbilanzgleichungen. Die elektrochemischen Reaktionen und der Phasenübergang von Wasser sind Teil des Modells. Die Energie- und Massenbilanzgleichungen sind mit der Tafelgleichung und einem Membranmodell gekoppelt, das den effektiven Wassertransport durch die Membran beschreibt.
Das System gewöhnlicher Differenzialgleichungen ist in MATLAB^{TM} implementiert und wird mit dem impliziten Löser ode15s gelöst. Das Modell ist numerisch effizient, so dass eine Betriebszeit von über einer Stunde auf einem Rechner mit 1533 MHz-Prozessor in weniger als einer Sekunde simuliert werden kann.
Die Simulationsergebnisse geben das dynamische Verhalten eines Brennstoffzellenstacks wieder. Beliebige Lastprofile können simuliert werden, was die Anwendung des Modells in der Systemsimulation und der modellbasierten Regelung ermöglicht. Zur Demonstration dieser Modelleigenschaften dient die Simulation eines stufenförmigen Stromdichteprofils. Ein Stack mit einer Nennleistung von 30 W und einer Spitzenleistung von 70 W wird experimentell untersucht. Durch den Vergleich von simulierter und gemessener Stackspannung und Stacktemperatur wird das Modell validiert.

Thesis Abstract

The driving force behind the recent development of small fuel cells is the possibility of achieving higher energy density compared to primary and secondary batteries. Hence, a comparison between portable PEMFCs and batteries is given in Chapter 1. Furthermore, a brief overview on the concepts of hydrogen storage and generation is provided and the operating principle of the PEMFC is introduced.
This thesis focuses on the modeling and simulation of the PEMFC. Chapter 1 concludes with a discussion of the motivation for the development and application of mathematical fuel cell models.

The physical and electrochemical fundamentals necessary for fuel cell modeling are introduced in Chapter 2, starting with the Butler-Volmer approach, which is used to describe the electrochemical reactions in the fuel cell. To prepare the modeling of the different transport processes in the PEMFC, the concept of mass conservation and the equation of continuity are introduced. In order to describe the gas diffusion, the flux expressions for Fick diffusion and Maxwell-Stefan multicomponent diffusion are derived. The description of the electric current inside the PEMFC requires the consideration of both the electron transport and the proton transport. Hence, the charge transport equations for electrons and protons are derived. The phenomenon of liquid water generation and transport in PEMFCs is considered by the introduction of the general multiphase flow equations. Thermal management is important for the operational behavior of PEMFCs. Accordingly, the heat equation for a multicomponent gas mixture is introduced. The consideration of the various couplings between the above-mentioned phenomena is essential for the validity of the simulation results.

Planar self-breathing fuel cells in printed circuit board (PCB) technology are currently being developed at the Fraunhofer Institute for Solar Energy Systems. The robustness and design flexibility of PCB technology makes it suitable for use as a platform. Complex conductor and insulator design is possible. The planar self-breathing design is promising since very few peripheral components are required.

The oxygen is supplied to the cathode not by a pump or fan but solely by diffusion. This allows one to build very small and light-weight fuel cell systems that operate silently. Currently, the typical power density for this type of cell is around 100 mW/cm^2 at 0.3 V cell voltage.
In order to analyze the operational behavior, a mathematical model of planar self-breathing fuel cells is developed and validated in Chapter 3. The geometry of the model is a two-dimensional symmetry element of a planar self-breathing fuel cell with a cathode opening ratio of 80%. The multicomponent transport of the species is considered as well as the couplings between the transport processes of heat, charge, and mass and the electrochemical reactions. Furthermore, to explain the oxygen mass transport limitation in the porous electrode of the cathode side an agglomerate model for the oxygen reduction reaction is developed.
The system of coupled partial differential equations (PDEs) is implemented in FEMLAB^{TM}. For the discretization of the PDEs the Galerkin finite element method is used. The resulting system of nonlinear equations is solved with the Newton method.
The cell model is validated by comparison of the measured overall performance of a planar self-breathing fuel cell with the predictions of the model. Based on the modeling results, a theoretical study of planar and self-breathing fuel cells is presented. The investigation of the operating behavior reveals the most important properties. The performance of this type of cell is determined by the competing effects of mass transfer and charge transfer. In particular, at high current density the membrane electrode assembly (MEA) dries out. Hence, the protonic conductivity of the MEA is limited and leads to a non-uniform charge generation rate in through-plane direction. This causes an inefficient utilization of the platinum catalyst. For example at a cell voltage of 0.1 V and a current density of 730 mA/cm^2 the charge generation rate at the interface between the cathode catalyst layer and the membrane is almost nine times higher than at the interface between the catalyst layer and the gas diffusion layer. Moreover, access to oxygen supply and electron supply is important for efficient use of the catalyst layer. For a planar-self breathing fuel cell with an opening ratio of 80% the charge generation rate is highest close to the edges of the ribs. The current distribution in the cathode is found to have a strong non-uniformity. This is due to the fact that the rib serves as the current collector but covers only 20% of the cathode area. Design guidelines are derived from the modeling results. At low current density, the mass transfer limitation is small and the use of wide ribs and thin gas diffusion layers is preferable. In the high current density regime, the ribs should be thin to reduce the mass transfer limitation. Furthermore, the lateral mass transfer resistance can be reduced by a high effective lateral diffusivity of the gas diffusion layer. However, to avoid significant charge transfer limitations between the ribs the lateral conductivity of the gas diffusion layer should be excellent.

In Chapter 4 the important issue of liquid water generation and transport in PEMFCs is addressed. One of the major tasks when operating this type of fuel cell is avoiding the complete flooding of the PEMFC during operation.
A one-dimensional and isothermal model is developed that is based on a coupled system of partial differential equations. The model contains a dynamic and two-phase description of the proton exchange membrane fuel cell. The mass transport in the gas phase and in the liquid phase is considered as well as the phase transition between liquid water and water vapor. The transport of charges and the electrochemical reactions are part of the model. Flooding effects that are caused by liquid water accumulation are described by this model. The gas saturation is decreased by the presence of liquid water. Important features of the model are that it describes the reduction of the ionic current density due to the presence of liquid water and the liquid water content in the electrodes couples to a dynamic transport process of liquid water in the porous layers. Moreover, the model contains a time-dependent description of the membrane that accounts for Schroeder's paradox. The membrane model is coupled with the two-phase flow equations in the electrodes.
The model is implemented in the software FEMLAB^{TM}. The time-dependent PDEs are discretized in space by using the Galerkin method with time-dependent nodal parameters. The resulting system of ordinary differential equations is solved using the implicit multistep solver ode15s of MATLAB^{TM}.
The validity of the novel model approach for the membrane is shown by the comparison of the measured and the simulated cell resistance. The model is applied to simulate cyclic voltammograms. The application of a time-dependent cell voltage on a time scale of minutes results in a time-dependent current-voltage curve that is characteristic for the liquid water transport processes in the PEMFC. A small test fuel cell is used to measure cyclic voltammograms. A hysteresis effect of the current-voltage relation and a time-dependent current density in the two-phase regime is found in both the simulation and the experiment. The hysteresis is caused by the accumulation of liquid water on the cathode side. The time-span between the highest current density and the maximum value of the liquid water saturation is between 70 s and 80 s. Characteristic frequencies of the liquid water transport through the PEMFC are derived. The liquid water transport across the membrane can be excited in the frequency region around 0.1 Hz whereas the liquid water transport through the gas diffusion layer is faster and can be excited around 1 Hz. Compared to that the gas diffusion is very fast and can be observed in the frequency range around 20 Hz. The model is used to simulate a periodic perturbation of the cell voltage in the two-phase regime. The resulting impedance spectrum indicates that a low frequency arc in impedance spectra is caused by the liquid water transport across the membrane.

Chapter 5 is focused on the dynamic investigation of PEMFC stacks. PEMFC stacks designed for the use in applications such as small robots are currently being developed at the Fraunhofer Institute for Solar Energy Systems. Understanding the dynamic behavior of fuel cell stacks is important for the operation and control of fuel cell stacks.
Using the single cell model of Chapter 3 and the dynamic model of Chapter 4 as basis, a mathematical model of a PEMFC stack is developed. However, due to the complexity of a fuel cell stack, the spatial resolution and dynamic description of the liquid water transport are not accounted for. These restrictions allow for direct comparison between the solution variables of the model and measurement data and for the simulation of hours of stack operation, which could otherwise not be achieved. The model is time-dependent and non-isothermal. It is based on energy and mass balance equations. Heat and mass transfer by convection and conduction within the stack, as well as changes due to the electrochemical reactions and the phase transition of water, are taken into account. The mass and heat transport equations are coupled with an electrical model that is based on the Tafel equation and a membrane model that accounts for the net-transfer of water through the membrane. The mathematical formulation of the model is a coupled differential algebraic equation system that contains ordinary differential equations in time describing the heat and mass transfer. An algebraic equation is used to describe the electrochemical reaction at the cathode.
The model is implemented in MATLAB^{TM}. The system of equations is solved by using the implicit multistep solver ode15s. The model is computationally efficient, i.e. an operation time of one hour can be simulated in a computing time of less than one second on a workstation using an AMD Athlon 1533 MHz processor.
Simulation results that represent the dynamic response of a fuel cell stack on load changes are shown. The mathematical stack model is capable of simulating arbitrary load profiles. These properties facilitate the application of the dynamic PEMFC stack model in system simulation and model-based control. The input parameters of the model are the mass and heat fluxes at the inlet of the stack, the overall current, and the ambient temperature. The solution variables are the heat and mass fluxes at the stack outlet, the temperature of the stack, and the stack voltage. For the validation of the model a PEMFC stack with a nominal power of 30 W and a peak power of 70 W is investigated experimentally. The measurement setup that is used for the validation measurements controls all of the input parameters and records the solution variables of the model. The validity of the model approach is proven by comparing simulated and measured load profiles and stack temperatures.

Acknowledgements

Firstly, I would like to thank Priv. Doz. Dr. Gerhard Willeke for supervising this thesis.

I am grateful to Prof. Dr. Paul Leiderer for his generosity in evaluating this thesis.

I would also particularly like to thank Dr. Jürgen Schumacher. His continuous help and support throughout is gratefully acknowledged. The technical discussions with him contributed substantially to the results of this thesis. I have benefited greatly from his supervision.

I am indebted to Dr. Christopher Hebling for giving me the opportunity to write this thesis in the department of energy technology at the Fraunhofer ISE.

Dr. Carsten Agert's support as a group leader of the fuel cell systems group in the department of energy technology is gratefully acknowledged.

The following members and former members of the fuel cell systems group deserve special mention:
Andreas Schmitz provided fruitful collaboration on the topic of planar and self-breathing fuel cells. The discussions and modeling sessions with him contributed substantially to the results of Chapter 3.
Markus Gnannt did excellent work on the development of a fuel cell system for the power supply of a laptop computer. His work provided valuable insights into the field of fuel cell stack and fuel cell system simulation.
The collaboration with Dr. Hong Mei Yu was important for the validation of the two-phase simulations in Chapter 4. I gratefully acknowledge her patience at the test stand. I would also like to thank her for conducting the ESEM and TEM measurements for this thesis.
Dietmar Gerteisen provided invaluable technical support with the dynamic measurements in Chapter 4.
I expressly thank Simon Philipps for his work on the dynamic modeling of fuel cell stacks. His valuable input is particularly evident in Chapter 5.

I also have benefited greatly from the suggestions of Ed Fontes and Olof Hernell of Comsol AB, Stockholm. I would like to thank Ed Fontes for his generosity during my stays in Stockholm.

Last but not least, I would like to thank my family and my girlfriend Anna for their support and understanding over the last three years.

Contents

List of Figures

Chapter 1

Introduction

1.1 Benefits of portable fuel cells

Portable and remotely located off-grid electronic appliances are usually powered by primary and secondary batteries. The drawback, especially with secondary batteries, is in many cases the insufficient energy density. Miniaturized fuel cells offer benefits as a substitute or supplement for batteries [1]. Recent comparative tests of PEMFC systems and batteries indicate that medium-sized fuel cell systems can supply portable power efficiently when more than 0.5 kWh is required [2, 3]. The possibility of achieving higher energy densities is the main driving force behind the recent development of miniaturized fuel cells.
Batteries and fuel cells generate electricity by an electrochemical reaction. The fuel cell itself is an energy converter that transforms chemical energy into electrical energy. Unlike a battery, where the reactants needed for the electrochemical reaction are an intrinsic part of the device, a fuel cell requires a continuous supply with reactants from an external storage unit. This design difference is an advantage of the fuel cell technology since the capacity and life-span of the fuel storage unit is independent of the energy converter. The overall energy density of the fuel cell system depends on the fuel storage capacity. Different technologies for the storage of fuels are available or under development. In all cases, the energy density of the fuels is excellent compared to batteries [4]. Hydrogen for example can be stored in pressurized gas containers [5]. The use of metal hydrides is another option for the storage of hydrogen. In metal hydrides the hydrogen is chemically bonded to the metal so energy is required to remove the hydrogen from the hydride. Chemical hydrides such as $NaBH_4$ or $NaAlH_4$ represent another possibility for the supply of a fuel cell [6, 7]. In this case, the hydrogen is produced by in-situ decomposition of chemical hydrides on the addition of water. Recent developments in nanotechnology indicate that hydrogen can be stored

in nano-carbon structures such as nano-tubes [8]. Here, the hydrogen is bonded physically, so very little energy is needed to remove the hydrogen from the storage unit. Finally, the use of hydrocarbons and microreformers is an option for fuel cell systems. In this case, fuels with high energy density such as methanol can be used. An empty fuel container can be replaced by a new one or can be refilled, a feature that is advantageous since it increases the energy density of the system. Furthermore, the fuel storage systems can be refilled many times whereas batteries degrade seriously when subjected to frequent charge cycles.
Fuel cells are also preferable in terms of the ecological impact of the technology. Batteries contain toxic materials and usually require several hundred times more energy during the production process than the energy they deliver to the consumer. For low power applications, the proton exchange membrane fuel cell (PEMFC) is by far the most commonly used type of fuel cell. In a PEMFC, a high conversion efficiency can be achieved at low temperatures, since the efficiency of a fuel cell is not limited by the Carnot process but by the Gibbs free energy of the reactants. However, only small quantities of portable fuel cells have been manufactured so far [9]. When considering the energy density of a fuel cell system, the volume of the fuel cell and its peripheral components has to be taken into account. The need for peripheral components such as valves, pumps, humidity regulators and fans reduces the energy density of the fuel cell system significantly [10]. These components have a minimum size and weight. Moreover, the pumps and fans produce noise, which is a disadvantage compared to batteries. In particular, these are issues for the design of small PEMFC systems. Furthermore, hydrogen for use in fuel cells has to be made available to the consumer. Different ways to produce hydrogen are currently under condsideration. Steam reforming of natural gas is the most efficient and widely used process for generating hydrogen. Research is also being conducted on similar processes for biomass and organic waste. Hydrogen can also be produced by the thermocatalytic decomposition of methane or other hydrocarbons. Water is another hydrogen-rich material. Electrolysis, thermochemical production or biophotolysis are some of the processes that could be applied to obtain hydrogen from water [11]. A detailed discussion of a possible hydrogen economy of the future and its implications is given in Ref. [12].
In any scenario, the development of small and efficient fuel cells is one of the keys for the widespread utilization of hydrogen and the PEMFC technology.

1.2 Operating principle of the PEMFC

The PEMFC is continuously supplied with oxygen or air on the cathode side and hydrogen gas on the anode side. The electrodes of the anode side and the cathode side are separated by a proton-conducting polymer membrane. A schematic

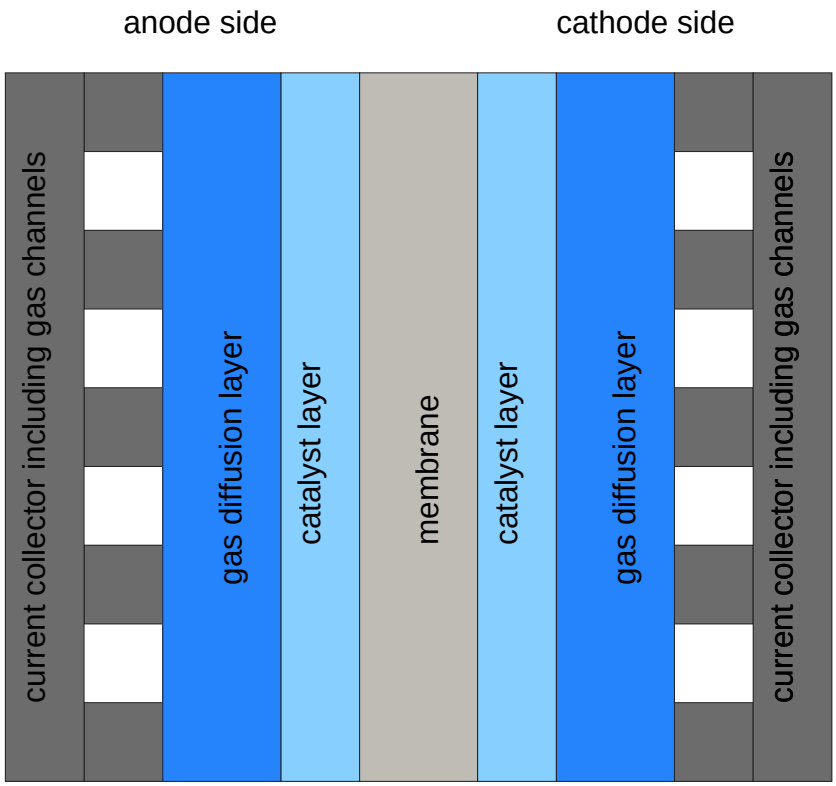

Figure 1.1: Schematic diagram of a PEMFC showing the different components of the fuel cell. The cathode and the anode side each consist of a current collector including the gas channels, a gas diffusion layer and an electrochemically active catalyst layer. The cathode and the anode are separated by the polymer membrane.

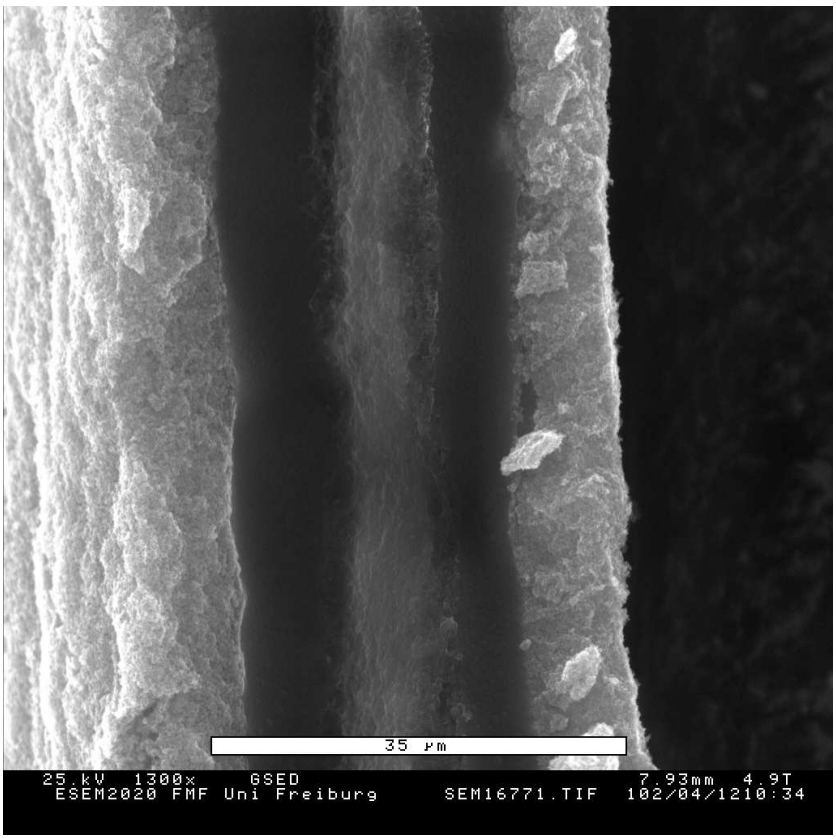

Figure 1.2: SEM image of a cross-section through a MEA. The light gray layers on the surface of the MEA are the catalyst layers that have a thickness of roughly 10 μm each. The dark area between the catalyst layers is the membrane that is about 25 μm thick. The gray feature in the center of the membrane is a PTFE supporting layer.

diagram of a PEMFC is shown in Fig. 1.1. In the overall chemical reaction of a PEMFC that is fueled with hydrogen, water is produced as a result of the exothermal reaction

$$\frac{1}{2}O_2 + H_2 \rightleftharpoons H_2O \; . \tag{1.1}$$

The reaction enthalpy is released as electrical energy and heat. The overall chemical reaction in a fuel cell is split into two separate reactions at the anode

$$H_2 \rightleftharpoons 2H^+ + 2e^- \tag{1.2}$$

and at the cathode

$$\frac{1}{2}O_2 + 2H^+ + 2e^- \rightleftharpoons H_2O \; . \tag{1.3}$$

In the anodic reaction, hydrogen is oxidized whereas in the cathodic reaction, oxygen is reduced. The electrons that are released at the anode can be delivered to the cathode via an external electrical circuit that connects the electrodes and thus delivers electrical power. At the cathode, the electrons combine with oxygen and protons. Water is the only product of the fuel cell reaction.

The membrane consists of a polymer electrolyte which provides good conductivity for protons if it is humidified. Currently the most commonly used class of solid polymer electrolyte materials is sulfonated fluoropolymers. These are co-polymers consisting of a perfluorinated polymer backbone and perfluorinated sidechains ending with sulfonic acid groups. Other important features of the membrane are impermeability for gases and sufficient mechanical and thermal stability. Moreover, the swelling of the membrane due to water uptake should be small.

The catalyst layer of the cathode and anode contains a small amount of Pt that is supported by carbon particles mixed with proton-conducting ionomer. The result is a highly porous layer that conducts electrons and protons and is permeable for gases. In order to improve the electrical contact, the catalyst layer is applied on top of the membrane. The resulting assembly of three layers is called the membrane electrode assembly (MEA). A scanning electron microscope (SEM) image of a MEA is shown in Fig. 1.2.

The reactants are supplied to the cell and distributed within the cell via gas channels. The gas channels are usually machined into the current collector plates. The current collector plates transfer the mechanical forces that are applied to the fuel cell in order to seal it and reduce the contact resistance. If the current collector plates are at the outer surface of the fuel cell, as shown in Fig. 1.1, they are called end-plates. Alternatively, the current collectors can be used for a series connection by stacking single fuel cells on top of each other. In the resulting fuel cell stack, the current collectors are called bipolar plates since they connect the cathode with the anode of adjacent cells. Bipolar plates are commonly made of graphite-polymer composites.

Highly porous gas diffusion layers are inserted between the current collectors and the catalyst layers in order to distribute the reactants homogeneously across the electrodes. Furthermore, the gas diffusion layer provides the electrically conducting connection between the current collector and the catalyst layer. Gas diffusion layers commonly consist of carbon fibers that provide excellent conductivity and high porosity simultaneously. During operation, the gas diffusion layer can get flooded with water that is generated in the fuel cell. Coating the carbon fiber material with hydrophobic PTFE is an option to reduce the flooding effect. Finally, the gas diffusion layer transfers the external force, that is applied in order to seal the fuel cell and reduce the contact resistances between the layers, to the MEA.

1.3 Use of mathematical fuel cell models

Mathematical models are important tools for the development of small and efficient fuel cells. More specifically, mathematical fuel cell models are useful in the following ways:

- To gain understanding and insight:
  In a fuel cell there are various transport processes such as heat transport and mass transport that occur in coupling with the electrochemical reactions. With a mathematical model, the various processes and the important couplings between them can be investigated and understood. Dynamic fuel cell models are valuable for the analysis of the time dependence of the fuel cell behavior. In particular, this is interesting for the investigation of intrinsically time-dependent phenomena like the accumulation and transport of liquid water in the fuel cell.

- To prove or disprove hypotheses:
  A mathematical model contains assumptions about the fuel cell and makes use of certain physical approaches to describe the fuel cell. Comparison of modeling results with measurement results indicates whether the hypotheses underlying the fuel cell model are correct.

- To analyze loss mechanisms:
  Optimum conversion efficiency is an important aim during the design and construction of a fuel cell. The different loss mechanisms such as mass transport resistance, flooding or dry-out of the membrane can be calculated using a fuel cell model. A quantitative measure of different losses and guidelines for their reduction is the result.

- To design experiments:
  Based on model predictions, experiments can be designed more specifically

to address important questions. For example, the two-phase model that is developed in section 4.4 is used for the simulation of cyclo-voltammograms. Subsequently, the cyclo-voltammograms are measured experimentally to investigate the liquid water transport in PEMFCs.

- To calculate distributed variables and parameters:
  It is difficult to measure distributions of important fuel cell variables and parameters such as the gas concentrations and the humidity of the membrane in an operating fuel cell. Using a fuel cell model, the variable and parameter distributions can be calculated. For example, in section 3.7 the spatial distributions of the reactants and the electrochemical potentials in a planar fuel cell are investigated. The numerical analysis of the microstructure elucidates the role of variables and parameters that are inaccessible to in-situ measurements.

- To characterize and design fuel cell components:
  An experimentally validated model can be used to characterize and design fuel cell components such as the gas diffusion layer, the membrane or the porous electrodes. Model-based evaluation of measurement data allows in-situ characterization of materials and components. The impact of microstructural parameters on the performance and behavior of the fuel cell can be investigated. From the results, guidelines for the design of components can be derived.

- To analyze the stability of fuel cell operation:
  Mathematical fuel cell models, particularly time-dependent models, can be used to study the conditions for stable operation of fuel cells. For example, the humidity of the gases and the ambient temperature have a strong impact on the behavior of the fuel cell. Based on a dynamic model, the stability limits can be predicted and the limiting process can be identified.

- To control and design fuel cell system operation:
  Starting with a comprehensive physical model, a simplified model can be derived that is suitable for the simulation of fuel cell stacks and fuel cell systems. A sensitivity analysis can yield the dominating effects for the simplified model. A simplified model can be implemented on a microcontroller for predictive control of a fuel cell system. For example, a simplified model of a fuel cell stack that is suitable for control applications is developed in section 5.3 of this thesis. Moreover, a fuel cell system model helps to identify critical system components prior to the construction of a new system and can provide guidance for the system design.

Chapter 2

Fundamentals of Fuel Cell Modeling

This chapter introduces the physical concepts and governing equations that are used for the mathematical fuel cell models in this thesis. In section 2.1, the Butler-Volmer approach is given, that describes the electrochemical reactions in the fuel cell. The concept of mass conservation and the equation of continuity are introduced in section 2.2. In analogy with the mass conservation equation, continuity equations for entropy, charge and energy are used in the following sections. In section 2.3, the flux expressions for Fick diffusion and Maxwell-Stefan multicomponent diffusion are derived. Based on the laws of electrostatics, the charge transport equations for electrons and protons in the fuel cell are derived in section 2.4. The chapter is completed by the introduction of the general multiphase flow equations in section 2.5 and the heat equation in section 2.6.
For the derivations of the transport equations, a representative elementary volume element (REV) in a bulk phase is considered. The Euler approach is used, in which the REV remains constant in space and time. Furthermore, the REV contains a sufficiently large number of particles to give a statistical basis for thermodynamic calculations. Local equilibrium is assumed in the volume element. This means that the equations of equilibrium thermodynamics can be applied to the REV. Additionally, the assumption of local electroneutrality is used.

2.1 The electrochemical reactions

In this section, a brief derivation of the Butler-Volmer equation is given. Based on activated complex theory, this equation is the standard approach to describe electrochemical reactions.
Consider the charge transfer of an electrochemical reaction

$$S_{ox} + ze^{-} \rightleftharpoons S_{red} \tag{2.1}$$

where z is the number of exchanged electrons in the rate determining step. S_{ox} is the oxidized species and S_{red} the reduced form of species S. Based on activated complex theory the anodic current density of the oxidation reaction and the cathodic current density of the reduction reaction can be expressed as [13]

$$i_a(\triangle\phi) = zFk_{ox}c_{red}exp\left(\frac{-\triangle G_{ox}(\triangle\phi)}{RT}\right) \tag{2.2}$$

$$i_c(\triangle\phi) = -zFk_{red}c_{ox}exp\left(\frac{-\triangle G_{red}(\triangle\phi)}{RT}\right) \tag{2.3}$$

where c_{red} and c_{ox} are the concentrations of the reduced and the oxidized species, respectively. The rate constants for the oxidation of S_{red} and the reduction of S_{ox} are k_{ox} and k_{red}, and $\triangle G_{ox}$ and $\triangle G_{red}$ are the activation Gibbs energy of the oxidation and the reduction reactions, respectively. $\triangle\phi$ is the Galvani potential difference between the electrode, where the potential is ϕ_e, and the electrolyte, where it is ϕ_p

$$\triangle\phi = \phi_e - \phi_p \ . \tag{2.4}$$

The electrochemical potential of the electron-conducting phase ϕ_e and proton-conducting electrolyte ϕ_p is discussed in section 2.4. In the reduction reaction, the electrons are transfered from the electrode to the electrolyte. Therefore, the activation Gibbs energy is the sum of the activation energy in the absence of a potential difference and an electrical contribution to the work [14]

$$\triangle G_{red}(\triangle\phi) = \triangle G_{red}(0) + \alpha zF\triangle\phi \ . \tag{2.5}$$

Thus if the electrode is more positive than the electrolyte, more energy is necessary to form an activated complex from S_{ox}. This is depicted schematically in Fig. 2.1. The parameter α is called the transfer coefficient and is in the range between 0 and 1. Now consider the oxidation reaction of S_{red}. In this case, S_{red} donates electrons to the electrode and hence the activation energy is changed by a corresponding electrical contribution

$$\triangle G_{ox}(\triangle\phi) = \triangle G_{ox}(0) - (1-\alpha)zF\triangle\phi \ . \tag{2.6}$$

When the electrochemical cell is producing current, the electrode potential changes from its equilibrium value $\triangle\phi_{eq}$ to its working value $\triangle\phi$. The difference is called the overpotential

$$\eta = \triangle\phi - \triangle\phi_{eq} \ . \tag{2.7}$$

Using this relation, the anodic and cathodic current densities can be rewritten as

$$i_a = \underbrace{zFk_{ox}c_{red}exp\left(\frac{-\triangle G_{ox}(0)}{RT}\right)exp\left(\frac{(1-\alpha)zF}{RT}\triangle\phi_{eq}\right)}_{=i_0} exp\left(\frac{(1-\alpha)zF}{RT}\eta\right) \tag{2.8}$$

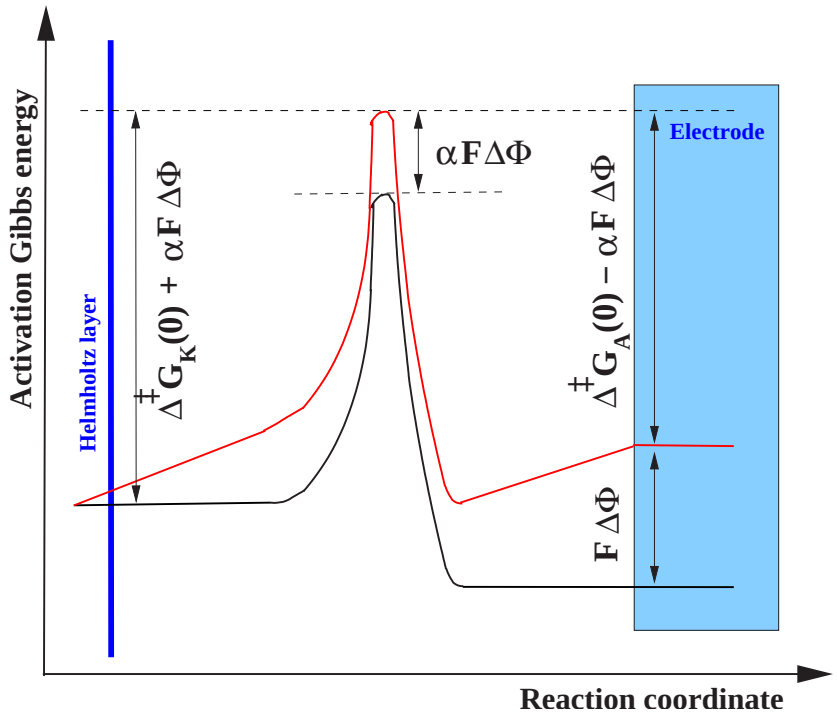

Figure 2.1: Schematic plot of the activation Gibbs energy for an electron during a redox reaction. The reaction coordinate indicates the progress of the electrochemical reaction. The potential difference $\triangle\phi$ shifts the maximum of the activation Gibbs energy by $\alpha F \triangle\phi$. The following substitutions apply: $\triangle^{\ddagger}G_K \equiv \triangle G_{red}$ and $\triangle^{\ddagger}G_A \equiv \triangle G_{ox}$.

$$i_c = -\underbrace{zFk_{red}c_{ox}exp\left(\frac{-\triangle G_{red}(0)}{RT}\right)exp\left(\frac{\alpha zF}{RT}\triangle\phi_{eq}\right)}_{=i_0}exp\left(\frac{\alpha zF}{RT}\eta\right) . \quad (2.9)$$

In equilibrium when $\eta = 0$, there is no net current at the electrode. Hence the two current densities cancel each other out. The modulus of the anodic and the cathodic current density in equilibrium is called the exchange current density i_0. The superposition of the two current densities yields the relation between the net current density and the overvoltage

$$i = i_a + i_c = i_0\left[exp\left(\frac{(1-\alpha)zF}{RT}\eta\right) - exp\left(\frac{-\alpha zF}{RT}\eta\right)\right] . \quad (2.10)$$

This relation is known as the Butler-Volmer equation. In the case of high anodic current density, i.e. if $\eta \gg \frac{RT}{zF}$, the reduction current i_c is negligible. Analogously, at high cathodic current density the oxidation current can be neglected. This results in

$$i = i_c = -i_0 exp\left(-\frac{\alpha zF}{RT}\eta\right) \quad (2.11)$$

which is known as the Tafel approximation.

2.2 The equation of continuity

The equation of continuity is developed by considering the mass balance over a REV through which the fluid is flowing. The size of the REV is allowed to go to zero, thereby treating the fluid as a continuum. The resulting partial differential equation is

$$\partial_t \rho_M + \nabla\cdot(\rho_M\vec{v}) = Q_M . \quad (2.12)$$

where ρ_M is the fluid density and $\vec{v}$ is the mass average velocity. Q_M describes a general fluid source. This is the equation of continuity, which describes the time rate of change of the fluid density at a fixed point in space.
In the next step, a mixture of N species i is considered. Application of the law of mass conservation to each species i yields the equation of continuity for species i in a multicomponent mixture.

$$\partial_t \rho_{i,M} + \nabla\cdot\vec{n}_i = Q_{i,M} \ , \ i = 1,...,N \quad (2.13)$$

Using the combined mass flux $\vec{n}_i = \vec{j}_{i,M} + \rho_{i,M}\vec{v}$, Eq. (2.13) is rewritten including the convective and diffusive fluxes explicitly

$$\partial_t \rho_{i,M} + \nabla\cdot\left(\rho_{i,M}\vec{v} + \vec{j}_{i,M}\right) = Q_{i,M} \ , \ i = 1,...,N . \quad (2.14)$$

This equation describes the change of the density of species i with time. $\vec{j}_{i,M}$ is the mass flux of species i with respect to the mass average velocity, that is, the diffusive mass flux. The term $\rho_{i,M}\vec{v}$ describes convection of species i with respect to the stationary axes of the REV. Addition of all N equations in Eq. (2.14) results in Eq. (2.12), where for the sum of the mass fluxes $\sum_i \vec{n}_i = \rho_M \vec{v}$ and $\sum_i \vec{j}_{i,M} = 0$ and the conservation of the total mass $\sum_i Q_{i,M} = 0$ is used. Alternatively, the equation of continuity for species i can be expressed in molar quantities as

$$\partial_t c_i + \nabla \cdot \vec{N}_i = Q_{i,m} \ , \ i = 1, ..., N \tag{2.15}$$

where c_i is the concentration of species i. $\vec{N}_i$ is the molar flux of species i which is defined by $\vec{N}_i = \vec{J}_i^* + c_i \vec{v}^*$. Inserting this into Eq. (2.15) yields

$$\partial_t c_i + \nabla \cdot \left(\vec{J}_i^* + c_i \vec{v}_i^* \right) = Q_{i,m} \ , \ i = 1, ..., N \tag{2.16}$$

where $\vec{J}_i^*$ is the molar flux with respect to the molar average velocity $\vec{v}^*$. The flux expressions $\vec{j}_{i,M}$ and $\vec{J}_i^*$ are derived in section 2.3.

2.3 Mass transport of gases

The entropy production rate for a REV is derived, starting with Jaumann's entropy balance equation. The entropy production rate determines the conjugate fluxes and forces. The Maxwell-Stefan equation for multicomponent mass fluxes is derived. Additionally, Fick's first law of diffusion, which is appropriate in binary systems, is introduced.
Jaumann's entropy balance equation is given by [15]

$$\rho_M \partial_t \hat{s} + \rho_M \vec{v} \cdot \nabla \hat{s} + \nabla \cdot \vec{s} = g_s \tag{2.17}$$

where ρ_M is the density of the fluid mixture and $\hat{s}$ denotes the entropy per unit mass. $\vec{s}$ is the entropy flux vector and g_s denotes the rate of entropy production per unit volume. An explicit expression for the entropy production rate g_s can be derived, from Eq. (2.17). This requires the use of the Gibbs equation

$$d\hat{U} = T d\hat{s} - p d\hat{V} + \sum_i \frac{\bar{G}_i}{M_i} d\omega_i \ , \ i = 1, ..., N \tag{2.18}$$

where $\bar{G}_i$ is the partial molar enthalpy that is also called the chemical potential, $\omega_i = \rho_i / \rho$ is the mass fraction and $\hat{U}$ and $\hat{V}$ denote the internal energy and the volume per unit mass, respectively. Furthermore the equations of change for mass

and energy are used to express the entropy production rate in terms of fluxes and forces[1]

$$g_s = -\left(\vec{q}\cdot\frac{1}{T^2}\nabla T\right) - \sum_i \left(\vec{j}_{i,M}\cdot\left[\nabla\left(\frac{1}{T}\frac{\bar{G}_i}{M_i}\right) - \frac{1}{T}\vec{g}_i\right]\right) - \sum_i \frac{1}{T}\frac{\bar{G}_i}{M_i} r_i \ . \quad (2.19)$$

This is the sum of conjugate thermodynamic fluxes and forces. $\vec{q}$ denotes the heat flux vector and $\vec{j}_{i,M}$ the mass flux vector, respectively. $\vec{g}_i$ is the external force per unit mass acting on species i. In Eq. (2.19), viscous dissipation is neglected. Furthermore, no external forces and chemical reactions are considered in the following, that is $\vec{g}_i = 0$ and $r_i = 0$. The mass flux vector $\vec{j}_{i,M}$ is the flux of mass per unit area per unit time with respect to the mass average velocity $\vec{v}$. This implies $\sum_i \vec{j}_{i,M} = 0$, that is, there are only $N-1$ independent mass fluxes. Because of the Gibbs-Duhem equation, there are also only $N-1$ independent forces. Taking into account this lack of independence, the entropy production can be written in the following form [15]

$$T g_s = -\vec{q}_h \cdot \nabla ln\ T - \sum_i \vec{j}_{i,M} \frac{cRT}{\rho_i} \vec{d}_i \quad (2.20)$$

where $\vec{q}_h = \vec{q} - \sum_i \frac{\bar{H}_i}{M_i}\vec{j}_{i,M}$ is the heat flux with the diffusional enthalpy flux subtracted. The diffusional driving forces $\vec{d}_i$ have the dimensions of reciprocal length and are given by

$$cRT\,\vec{d}_i = c_i RT \nabla ln\ a_i + (x_i - \omega_i)\nabla p \ . \quad (2.21)$$

According to the linearity postulate, each vector flux must depend linearly on all of the vector forces in the system, that is

$$\vec{j}_{i,M} = -a_{i0}\nabla ln\ T - \rho_i \sum_j \frac{cRTa_{ij}}{\rho_i \rho_j}\vec{d}_j \ , \ i = 1,...,N \ . \quad (2.22)$$

In this equation, the quantities a_{i0} and a_{ij} are phenomenological coefficients. Because there are $N-1$ independent mass fluxes $\vec{j}_{i,M}$ and $N-1$ independent diffusional forces $\vec{d}_i$, the coefficients a_{ij} must be symmetric according to the Onsager reciprocal relations. The phenomenological coefficients can be related to transport coefficients. First a_{i0} is relabelled as D_i^T, the multicomponent thermal diffusion coefficient. The multicomponent Fick diffusivities are defined by $D_{ij} = -cRTa_{ij}/\rho_i\rho_j$. Hence Eq. (2.22) can be written as

$$\vec{j}_{i,M} = -D_i^T \nabla ln\ T - \rho_i \sum_j D_{ij}\vec{d}_j \ , \ i = 1,...,N \ . \quad (2.23)$$

[1] For the intermediate steps, see C.F. Curtiss and R.B.Bird, Ind. Eng. Chem. Research, **38**, 2515-2522 (1999)

These are the generalized Fick equations. When Eq. (2.21) is substituted into Eq. (2.23), there are three contributions to the mass flux vector $\vec{j}_{i,M}$. These are the concentration diffusion term, the pressure diffusion term and the thermal diffusion term

$$\vec{j}_{i,M} = -D_i^T \nabla ln\, T - \rho_i \sum_j D_{ij} \left(x_j \nabla ln\, x_j + \frac{x_j - \omega_j}{p} \nabla p \right) \tag{2.24}$$

where x_j is the molar fraction of species j. Finally, the mass flux is expressed in terms of the mass fraction as follows

$$\vec{j}_{i,M} = -D_i^T \nabla ln\, T - \rho_i \sum_j D_{ij} \left[\nabla \left(\frac{\omega_j / M_j}{\sum_f (\omega_f / M_f)} \right) + \frac{x_j - \omega_j}{p} \nabla p \right] . \tag{2.25}$$

This is equivalent to

$$\vec{j}_{i,M} = -D_i^T \frac{\nabla T}{T} - \rho \omega_i \sum_j D_{ij} \left[\frac{M}{M_j} \left(\nabla \omega_j + \omega_j \frac{\nabla M}{M} \right) + \frac{x_j - \omega_j}{p} \nabla p \right] . \tag{2.26}$$

This formulation of the diffusive mass flux is used for the description of multi-component systems in this thesis.
In isothermal binary systems in which species i is diffusing through species j, the flux expression is described by Fick's law of binary diffusion

$$\vec{J}_i^* = -c \mathtt{D}_{ij} \nabla x_i \tag{2.27}$$

where $\vec{J}_i^*$ is the molar flux with respect to the molar average velocity and $\mathtt{D}_{ij}$ is the binary diffusion coefficient. c is the molar concentration of the binary gas. Equivalently, Fick's law can be expressed in terms of the mass flux of the species $\vec{j}_{i,M}$. This yields

$$\vec{j}_{i,M} = -\rho \mathtt{D}_{ij} \nabla \omega_i \tag{2.28}$$

where ρ is the mass density and ω_i denotes the mass fraction of species i. In binary systems the differential relation between the mass fraction and the molar fraction is given by

$$\nabla \omega_i = \frac{M_i M_j \nabla x_i}{\left(x_i M_i + x_j M_j \right)^2} . \tag{2.29}$$

2.4 Charge transport

In this section the charge transport equation is derived. The assumption of local electroneutrality implies that charge is conserved in the REV. Protons and electrons contribute to the measurable current in the fuel cell. The current for each

species is a superposition of a field current and a diffusion current. The use of Ohm's law and the Einstein relation between the mobility and the diffusion coefficient of a species lead to the electrochemical potential and the transport equations for electrons and protons.
The general charge conservation equation for a REV is given by

$$\partial_t \rho_C + \nabla \cdot \vec{j} = 0 \tag{2.30}$$

where ρ_C is the charge density. The measurable current density $\vec{j}$ is a superposition of the electron current density $\vec{j}_e$ and the proton current density $\vec{j}_p$

$$\vec{j} = \vec{j}_e + \vec{j}_p \tag{2.31}$$

The overall charge density ρ_C is given by the sum of the electron charge density and the proton charge density

$$\rho_C = \rho_{e,C} + \rho_{p,C} \ . \tag{2.32}$$

The assumption of local electroneutrality implies that $\rho_C = 0$ and hence Eq. (2.30) states that the measurable current is constant throughout the fuel cell. The proton current density and the electron current density are combined charge fluxes that contain a current due to the electric field $\vec{j}_{i,E}$ and a concentration-driven current $\vec{j}_{i,D}$

$$\vec{j}_i = \vec{j}_{i,E} + \vec{j}_{i,D} \ , \ i = e, p \ . \tag{2.33}$$

Ohm's law relates the first term of Eq. (2.33) with the electric field $\vec{E}$

$$\vec{j}_{i,E} = \sigma_i \vec{E} = -\sigma_i \nabla \psi \ . \tag{2.34}$$

The electric conductivity σ_i is a property of the conducting material. Since electrons and protons are spatially separated in the fuel cell, the index i denotes not only the species but also the proton-conducting polymer phase and the electron-conducting phases. ψ denotes the electrostatic potential. According to Fick's first law, the diffusion current density can be expressed in terms of the concentration gradient

$$\vec{j}_{i,D} = -\mathtt{D}_i F \nabla c_i \ , \ i = e, p \ . \tag{2.35}$$

The mobility of the charged species can be expressed using the Einstein relation [16]

$$\nu_i = \frac{\sigma_i}{F c_i} = \frac{F \mathtt{D}_i}{RT} \ . \tag{2.36}$$

Combining Eq. (2.33), Eq. (2.34), Eq. (2.35) and Eq. (2.36) yields

$$\vec{j}_i = -\sigma_i \left[\nabla \psi + \frac{RT}{F} \nabla ln c_i \right] = -\sigma_i \nabla \phi_i \ . \tag{2.37}$$

In the last step, ϕ_i is introduced, i.e. the electrochemical potential of species i in phase i. According to Eq. (2.37), the electrochemical potential ϕ_i is defined as

$$\nabla\phi_i \equiv \left[\nabla\psi + \frac{RT}{F}\nabla lnc_i\right] . \tag{2.38}$$

The charge transport equation for the species is obtained by combination of Eq. (2.30), Eq. (2.31), Eq. (2.37) and by use of the assumption of local electroneutrality

$$\nabla\cdot[-\sigma_i\nabla\phi_i] = Q_{i,C} \ , \ i = e,p \ . \tag{2.39}$$

The conservation of charge requires that $\sum_i Q_{i,C} = 0$ holds. With respect to each species, the electrochemical reactions act as sources and sinks that can be described by $Q_{i,C}$. In the time-dependent charge balance equation, the double layer capacitance needs to be considered. The electrochemical double layer can be approximated locally by an electrostatic capacitor. Under open circuit conditions, the maximum voltage appears across the double layer. This corresponds to a charged capacitor. The amount of charge which is accumulated in a capacitor is given by the product of the capacitance and the potential difference across the capacitor. Charging and discharging of the double layer capacitance changes the charge density of protons and electrons in the REV. The time-dependent species charge balance follows from Eq. (2.30), Eq. (2.32) and Eq. (2.39)

$$\partial_t\rho_{i,C} - \nabla\cdot[\sigma_i\nabla\phi_i] = Q_{i,C} \ , \ i = e,p \tag{2.40}$$

where $\sum_i \rho_{i,C} = 0$ and $\sum_i Q_{i,C} = 0$.

2.5 The two-phase flow equations

For the derivation of the general multiphase flow equations, a REV is considered that contains a rigid porous matrix and several immiscible phases. The porosity of the matrix π takes into account that only part of the REV is filled with fluid. The average fluid mass flux is assumed to be much larger than the deviations from this average value. Accordingly, no dispersion effects are considered. The continuity equation for each phase k within a multiphase system is derived by taking into account that phase k does not fill the pore space completely. Hence, the volume fraction π_k for each phase k is used as the storage volume instead of the porosity π [17]

$$\partial_t\left(\pi_k\rho_k\right) + \nabla\cdot\left(\pi_k\rho_k\vec{v}_{ak}\right) = Q_{k,M} \ . \tag{2.41}$$

ρ_k is the density of phase k. If the saturation s_k is defined as the fraction of the pore space which is filled by phase k, the volume fraction for phase k is given by

$\pi_k = s_k\pi$. The average velocity of phase k depends on the Darcy velocity $\vec{v}_k$ and the porosity π and can be written as $\vec{v}_k = \pi_k\vec{v}_{ak}$. Inserting this into Eq. (2.41) yields the continuity equation for phase k

$$\partial_t\left(s_k\pi\rho_k\right) + \nabla\cdot\left(\rho_k\vec{v}_k\right) = Q_{k,M}\ . \tag{2.42}$$

In the multiphase flow literature, Darcy's law is widely used as a macroscopic momentum equation. In all volume averaging schemes presented in the literature, it is shown that the momentum balance can be simplified to Darcy's law [18]. The following assumptions are necessary to derive Darcy's law [19]

- The momentum transfer between phases due to mass transfer is zero.
- The momentum transfer by viscous shear within a phase is negligible.
- Gravity is the only external force. It acts only in the vertical direction.
- The viscous stress follows Newtons's law for incompressible fluids.
- The no-slip condition applies at the interface between the rigid matrix and the fluid.

It has been experimentally proven [20] that the Darcy velocity of each phase in a porous medium can be described by the generalized Darcy law

$$\vec{v}_k = -\frac{\mathbf{K}_k}{\mu_k}\left(\nabla p_k - \rho_k\vec{g}\right)\ . \tag{2.43}$$

The conductivity of phase k, $\mathbf{K}_k$, and the intrinsic permeability, $\mathbf{K}$, are related by $\mathbf{K}_k = k_{rk}\mathbf{K}$ where the relative permeability k_{rk} is a scaling factor that depends on the saturation of the phases present. The generalized Darcy law can thus be written as

$$\vec{v}_k = -\frac{k_{rk}}{\mu_k}\mathbf{K}\cdot\left(\nabla p_k - \rho_k\vec{g}\right) \tag{2.44}$$

In order to derive a system of multiphase flow differential equations, Eq. (2.44) is combined with Eq. (2.42). This yields

$$\pi\rho_k\partial_t s_k + \rho_k s_k\partial_t\pi + \pi s_k\frac{\partial\rho}{\partial p}\partial_t p - \nabla\cdot\left(\rho_k\frac{k_{rk}}{\mu_k}\mathbf{K}\cdot\left(\nabla p_k - \rho_k\vec{g}\right)\right) = Q_{k,M} \tag{2.45}$$

with the constraint $\sum_k s_k = 1$. These equations describe the simultaneous flow of two or more immiscible fluids in a porous medium. In the context of this thesis, Eq. 2.45 is used to describe the transport of liquid water and the gaseous species through the porous components of the fuel cell.

2.6 The energy equation

The law of conservation of energy is an extension of the first law of classical thermodynamics, which concerns the difference in internal energy of two equilibrium states of a REV due to the heat added and work done, that is $\triangle U = Q + W$. Both kinetic and internal energy may enter the REV by convective transport. Here kinetic energy means the energy associated with the observable motion of the fluid, which is $1/2\rho v^2 = 1/2\rho(\vec{v}\cdot\vec{v})$ per unit volume. $\vec{v}$ is the mass average fluid velocity vector. The internal energy per unit mass $\hat{U}$ is the kinetic energy of the constituent molecules with respect to the mass average velocity $\vec{v}$ and the energy associated with vibration, rotation and interaction of the molecules. Heat may enter and leave the REV by heat conduction as well. Work may be done on the fluid by stresses. This includes the work done by pressure forces and by viscous forces. In addition external forces such as gravity can do work on the system. The different contributions to the energy balance are summarized in the equation of energy conservation

$$\partial_t\left(\frac{1}{2}\rho v^2+\rho\hat{U}\right)+\nabla\cdot\underbrace{\left((\frac{1}{2}\rho v^2+\rho\hat{U})\vec{v}+\vec{q}+p\vec{v}+[\tau\cdot\vec{v}]\right)}_{\vec{e}}-\rho(\vec{v}\cdot\vec{g})=Q_E \quad (2.46)$$

where $\vec{e}$ denotes the combined heat flux consisting of the molecular and the convective heat fluxes and Q_E accounts for different energy sources. This is the heat equation for a single fluid. Formally, the same equation describes the mixture of N species i. However, in the case of a multicomponent mixture, the symbols need to be redefined. First the heat flux is rewritten as

$$\vec{q}=-k\nabla T+\sum_i\frac{\bar{H_i}}{M_i}\vec{j}_{i,M}\ ,\ i=1,...,N \quad (2.47)$$

where $\vec{j_i}$ is the mass flux of species i with respect to the mass average velocity. The first term is Fourier's law of heat conduction, which describes the molecular transport of heat in isotropic media. The second term describes the heat transport by each of the diffusing species. The quantity $\bar{H_i}$ is the partial molar enthalpy of species i. The thermal conductivity of the mixture in absence of any mass fluxes is k. In the case of low velocity and low density of the fluids, the terms $1/2\rho v^2$ and $[\vec{\tau}\cdot\vec{v}]$ are negligible. Using the relations $\vec{j}_{i,M}=M_i\vec{J_i}$ between the mass flux and the molar flux with respect to the mass average velocity and $\rho\hat{V}=1$ leads to

$$\vec{e}=-k\nabla T+\sum_i\bar{H_i}\vec{J_i}+\rho\hat{H}\vec{v} \quad (2.48)$$

where $\hat{H} = \hat{U} + p\hat{V}$ is the enthalpy per unit mass. The last term can be rewritten as $\rho\hat{H}\vec{v} = \sum_j c_j H_j \vec{v}$. The use of $\vec{J}_i = c_i(\vec{v}_i - \vec{v})$ and $\vec{N}_i = c_i\vec{v}_i$ yields

$$\vec{e} = -k\nabla T + \sum_i \bar{H}_i \vec{N}_i \ . \tag{2.49}$$

Combination of Eq. (2.46) and Eq. (2.49) leads to the equation of energy conservation for a multicomponent gas mixture

$$\partial_t(\rho\hat{U}) + \nabla \cdot \left(-k\nabla T + \sum_i \bar{H}_i \vec{N}_i \right) - \rho(\vec{v}\cdot\vec{g}) = Q_E \ , \ i = 1, ..., N \ . \tag{2.50}$$

Chapter 3

Modeling Planar Fuel Cells

A theoretical study of planar and self-breathing fuel cells is presented in this chapter. In section 3.1, a review of recent work on modeling PEMFCs is given with a focus on steady-state and single-phase models. The benefits of planar self-breathing fuel cells in printed circuit board (PCB) technology are discussed. A mathematical model of planar self-breathing fuel cells is developed and validated in sections 3.2 to 3.6. The geometry of the model is a two-dimensionally symmetric element of a planar self-breathing fuel cell. The multicomponent transport of the species is considered as well as the couplings between the transport processes of heat, charge and mass and the electrochemical reactions. Furthermore, an agglomerate model for the description of the oxygen reduction reaction is developed. The cell model is validated by comparison of the measured overall performance of a planar self-breathing fuel cell to the predictions of the model. The model is applied to study the behavior of planar self-breathing fuel cells during operation in section 3.7. The results of this study show that the mass transport, the charge transport, the heat transport and the electrochemical reactions are strongly coupled. The consideration of these couplings is essential for the validity of the simulation results. The gas distribution, the potential distribution and the temperature distribution are influenced by the geometric design of the cathode end-plate. Thus the charge generation rate in the active area of the cathode and anode is affected by the ribs of the cathode end-plate. A strong non-uniformity of the current distribution over the cathode is found. Based on the model, improvements of the fuel cell design and the components are suggested.

3.1 Literature review of steady-state modeling

In current research, fuel cells are considered as power supplies for portable electronic devices. A hydrogen-air fuel cell working with a polymer electrolyte can

reach a high volumetric energy density compared to conventional battery systems. The fuel cell system also provides high gravimetric system energy. The energy density of a 10 W Li ion battery system including charger and wires is about 44 Wh/kg. By comparison, a fuel cell system including its periphery reaches an energy density as high as 530 Wh/kg [1].

Mathematical modeling is an important part of the development and design work in fuel cell research. A large amount of work has been published regarding the modeling of the PEMFC. Amphlett et al. [21] developed an empirical model for the Ballard Mark IV cell. Their model combines performance losses in parametric equations based on cell operating conditions. Bernardi and Verbrugge [22, 23] used a numerical approach. They developed a model of a PEMFC from fundamental transport properties. A similar model with an improved description of the cathode was presented by Pisani et al. [24]. Springer et al. [25, 26] also used a numerical approach accounting for the cathode and the membrane of a PEMFC. Kulikovsky [27] presented an analytical along-the-channel model of the proton exchange membrane fuel cell. A similar type of model for generic fuel cell systems was presented by Mann et al. [28]. A simplified engineering model of a PEMFC was published by Marr and Li [29]. Baschuk and Li [30] used this approach to investigate the influence of various degrees of water flooding in the cathode on the cell performance.

Fuller and Newman [31] investigated strategies for heat and water management. Rowe and Li [32] presented a one-dimensional model that accounts for variable membrane hydration, the influence of mass transport limitations, temperature variation, and evaporation and condensation of water. The model was used to investigate different fuel cell designs and operating conditions. Nguyen and White [33] presented a one-dimensional water and heat management model that was used to investigate the effectiveness of various humidification designs. Based on that work, Yi and Nguyen [34] developed an along-the-channel model with an improved description of the heat transfer processes.

A two-dimensional fuel cell model was presented by Bradean, Promislow and Wetton [35]. In that work, a cross-section of the porous cathode taken normal to the gas flow in the channels is modeled. Operation under steady-state conditions is considered. Gurau et al. [36] presented a two-dimensional and non-isothermal model describing the entire sandwich of the fuel cell. The model focuses on the description of momentum transfer. Recent work by Kulikovsky, Divisek and Kornyshev [37] shows the influence of the gas channels in the current collector. Dead and active reaction zones in the catalyst layer depending on the carbon phase conductivity are identified.

A couple of three-dimensional models have been presented recently. A steady-state straight-channel model focusing on heat transfer is presented in Ref. [38]. All major transport phenomena for a similar geometry were modeled by Berning

et al. [39]. Dutta et al. [40] presented a three-dimensional model focusing on the prediction of mass flow between the channels in a PEMFC with a serpentine flow path. Three-dimensional predictions of local current density and membrane conductivity inside a PEMFC with a serpentine flow path were presented by Lee et al. [41].
Printed circuit board (PCB) technology offers an attractive approach for portable fuel cell development [42]. Important advantages of fuel cells in PCB technology include the robustness and reliability of this technology and the fast prototype cycle times. Moreover, the PCBs provide high design flexibility and low weight, and facilitate complex conductor and insulator design. Schmitz and co-workers [43] developed self-breathing fuel cell prototypes in PCB technology. The benefits of self-breathing fuel cells are the silent operation and the small volume and low weight of the system, since very few peripheral components are required. These properties make planar self-breathing fuel cells in PCB technology a strong candidate for use in portable devices.
Despite the large amount of work that has been published on the modeling of PEMFCs, no comprehensive model of a planar self-breathing fuel cell has been published so far. In this chapter a mathematical model is presented that is appropriate to the analysis and optimization of planar self-breathing fuel cells. The model is validated using a self-breathing fuel cell in PCB technology. The measured fuel cell characteristic is compared to the simulation results. Furthermore, the model is applied to analyze the influence of the cell design on the behavior of the cell. The distribution of gaseous species, the potential distribution and charge transfer rate, the temperature distribution and the conjugate fluxes are investigated at a typical point of operation.

3.2 Model description

The PEMFC model presented here is a two-dimensional, non-isothermal, steady-state model of a complete cell sandwich of a self-breathing planar fuel cell. This type of fuel cell is described in Ref. [44]. A detailed description of the following transport phenomena is provided within the model:

- conduction of electrons through the carbon support of the catalyst layers and the gas diffusion layers
- migration of protons through the polymer phase of the catalyst layers and the membrane
- diffusion of oxygen, water vapor and nitrogen through the openings, the gas diffusion layer and the catalyst layer of the cathode

- diffusion of hydrogen and water vapor through the gas channel, the gas diffusion layer and the catalyst layer of the anode
- convection of hydrogen and water vapor through the gas channel of the anode
- diffusion of water through the membrane
- electro-osmotic drag of water through the membrane
- conductive heat transfer through the membrane, the electrodes and cathode and anode plates of the fuel cell

The electrochemical reactions are described using a Tafel approach. The oxygen reduction reaction is assumed to occur in reactive agglomerated zones which are filled with water. The diffusion of the oxygen into these zones is described using an agglomerate model. The membrane model contains both the protonic conductivity and the diffusivity of water as a function of membrane humidity and temperature. The dependence of the electro-osmotic drag on the membrane humidity is considered.

Model assumptions

A fuel cell is a complex system involving both microscopic and macroscopic geometric features, coupled transport processes and the electrochemical reaction. For the numerical implementation of a fuel cell model, simplifying assumptions have to be made. The main assumptions used in this model are as follows:

- The fuel cell operates under steady-state conditions.
- The electrochemical reactions are described using Tafel kinetics.
- The phase change of water is neglected.
- Product water is assumed to be generated in the gas phase.
- The membrane humidity is assumed to be a linear function of the water vapor activity in the electrodes.
- Mass transport in the electrodes and charge transport is described using an effective medium approach for the catalyst layers and the gas diffusion layers.

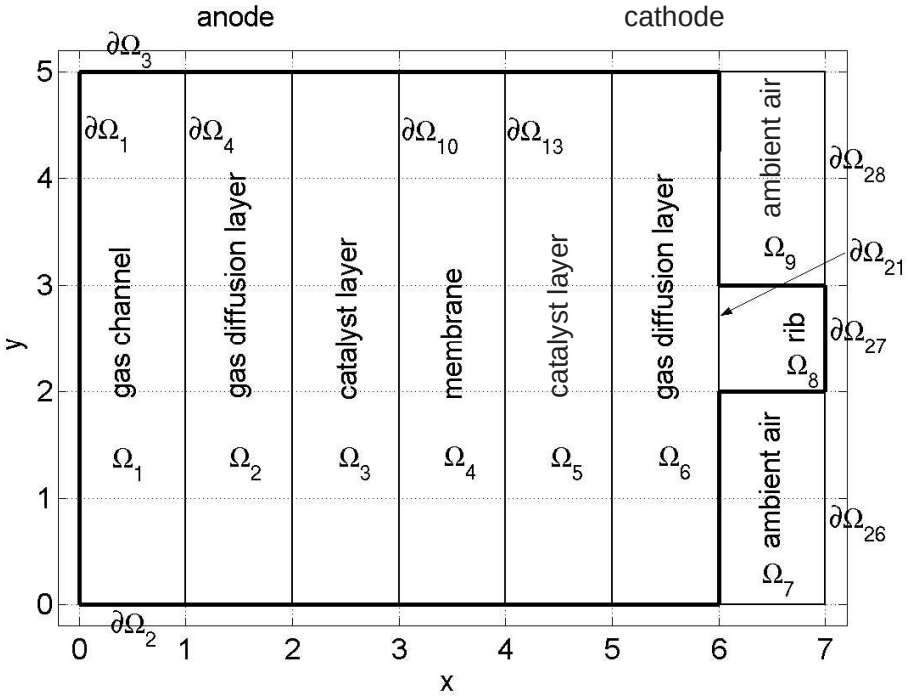

Figure 3.1: The geometry of the computational domain is shown using normalized coordinates. Subdomains are labelled as Ω_i, boundaries are labelled as $\partial\Omega_i$. The model equations are scaled resulting in subdomains of equal thickness. The overall thickness of the cell is 3.055 mm. The length of the domain along the y-direction is 5.0 mm.

- In the assembled cell, the components are compressed. Spatial variation in this compression caused by the structure of the cathode end plate is not considered.
- Contact electrical losses at the interfaces between different components of the cell are not part of the model.
- Contact thermal resistances are neglected.

3.3 Computational domain

The computational domain of the fuel cell model is shown in Fig. 3.1. The domain represents a cross-section through a planar and self-breathing fuel cell of the type developed and investigated in [44]. In this thesis, an opening ratio of 0.8 is used for both the simulation and the test cell. The symmetry of the planar fuel cell

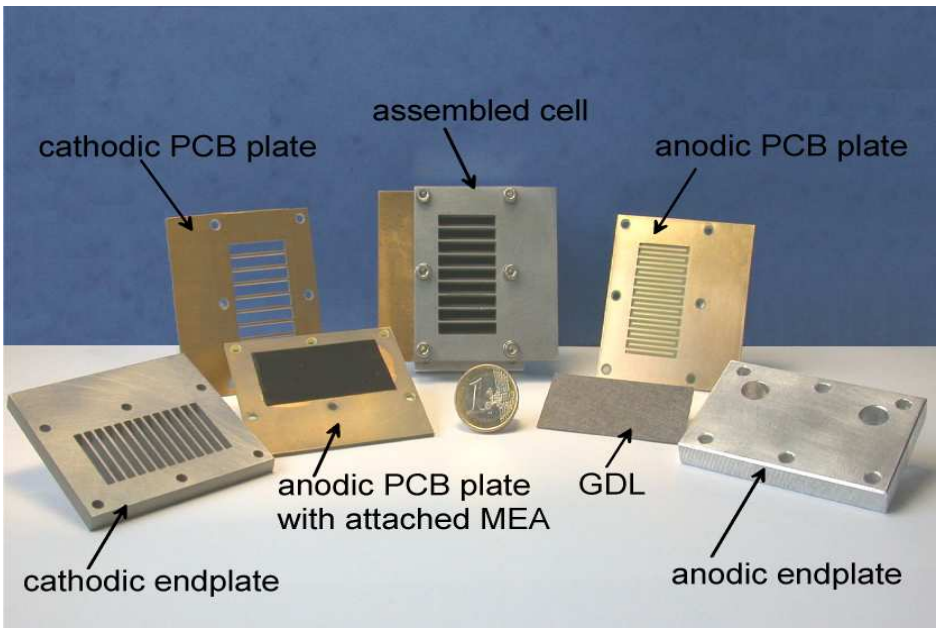

Figure 3.2: The type of reference fuel cell which was used to validate the fuel cell model. The photo shows the components of the cell and the assembled planar self-breathing fuel cell. The symmetry of the open cathode is exploited in Fig. 3.1 where a cross-section through the planar cell is shown.

shown in Fig. 3.2 is reflected in the geometry of the computational domain. The computational cost of the simulations is reduced by introducing the symmetric computational domain instead of a computational domain for the whole fuel cell. The domain is divided into different subdomains Ω_i, which describe the hydrogen gas channel Ω_1, the gas diffusion layers $\Omega_{2/6}$, the catalyst layers $\Omega_{3/5}$ and the membrane Ω_4. The geometry of the cathode openings, including one rib Ω_8 of the cathode plate and regions filled with ambient air $\Omega_{7/9}$ completes the description of the fuel cell. The subdomains are coupled with each other via appropriate boundary conditions at the boundaries denoted by $\partial\Omega_i$. As a second measure to improve the computational efficiency, the equations have been scaled. Equally thick subdomains resulting in a very simple geometry are obtained. The computational domain can therefore be easily discretized, resulting in a mesh of good quality. The scaling of the electrode regions is of particular importance to improve the numerical stability of the model. The domain depicted in Fig. 3.1 corresponds to a physical domain of the cell which extends 5 mm along the y-direction. The thickness of the gas channel is 0.8 mm. The cathode end plate is 1.5 mm thick. In the computational domain, the end-plate is represented by one rib Ω_8 surrounded by air denoted as Ω_7 and Ω_9. A 350 μm thick diffusion layer is used on both sides. The membrane electrode assembly has a polymer thickness of 35 μm and active regions which are 10 μm in thickness each. Hence the overall thickness of the modeled cell is 3.055 mm.

3.4 Steady-state model equations

3.4.1 Agglomerate model of the porous cathode

The description of the oxygen reduction reaction is critical due to the relatively high activation overvoltage on the cathode side of a hydrogen-air PEMFC. The dispersed catalyst (Pt/C) within the catalyst layer forms agglomerated zones filled with electrolyte. These zones contain water-flooded channels into which the oxygen is dissolved. The reactant gas subsequently diffuses to the reaction site. A schematic diagram of the catalyst layer is shown in Fig. 3.3. The divergence of the ionic current density $\vec{j}_c$ in the cathode is related to the average current density i_{aggl} at the surface of the agglomerated catalyst particles

$$\nabla \cdot \vec{j}_c = \Lambda i_{aggl} \ , \tag{3.1}$$

where Λ is the surface area of the agglomerates per unit volume. This can be expressed as

$$\Lambda = n_{aggl} S_{aggl} \ , \tag{3.2}$$

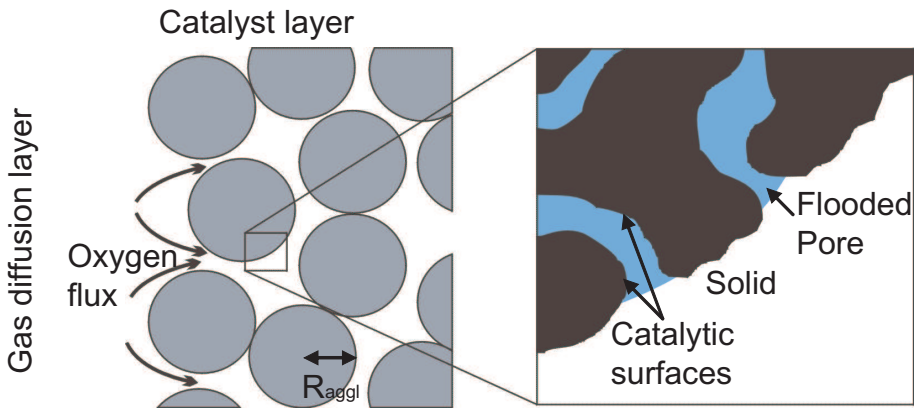

Figure 3.3: This figure schematically shows the structure of the catalyst layer. The dispersed catalyst and the polymer form agglomerated zones that contain small pores. These pores are filled with water. The oxygen that enters the catalyst layer dissolves and diffuses through the water to the catalytic sites where the electrochemical reaction occurs. Compare also with the TEM image of the catalyst layer in Fig. 4.4

where n_{aggl} is the number of agglomerates per unit volume and S_{aggl} is the outer surface area of one agglomerate. The total charge transfer in an agglomerate at steady state has to be balanced by a corresponding influx of oxygen through the agglomerate-gas phase interface. Hence, the average current density on the surface of the agglomerate particles is

$$i_{aggl} = N_{O_2} 4F \ , \tag{3.3}$$

where N_{O_2} is the average oxygen diffusion flux in the liquid phase at the surface of an agglomerate. The solid phase fraction of a spherical agglomerate is calculated as follows

$$1 - \pi_5 = n_{aggl} \frac{4\pi R_{aggl}^3}{3} \ , \tag{3.4}$$

where π_5 is the gas porosity of the catalyst layer and R_{aggl} is the average radius of an agglomerate. The rate of oxygen conversion in a single agglomerate particle can be expressed according to Bird, Stewart and Lightfoot [15] as

$$W_{ARc} = 4\pi R_{aggl} D_A [O_2]^s \left(1 - \sqrt{\frac{k_c'' a}{D_A}} R_{aggl} \coth \sqrt{\frac{k_c'' a}{D_A}} R_{aggl} \right) , \tag{3.5}$$

where a is the available catalytic surface area per unit volume within the agglomerate particle. Here, it is assumed that the oxidant reaches the surface of the

flooded pores of the agglomerate, dissolves according to Henry's law implying $[O_2]^s = p_{O_2}/H_{O_2}$, and then diffuses to the catalyst particles with a diffusion constant D_A. A Tafel approach according to Eq. (2.11) is used for the oxygen reduction reaction with a reaction rate constant k_c''

$$k_c'' = \frac{i_{0,c}}{4F}\frac{1}{[O_2]^{ref}}\exp\left(-\frac{\alpha_c z_c F}{RT}\left(\Phi_e - \Phi_p - \Delta\Phi_{c,eq}\right)\right), \tag{3.6}$$

where $i_{0,c}$ is the exchange current density of the oxygen reduction reaction under reference conditions and α_c and z_c are the symmetry factor and the number of electrons transfered in the rate-determining step, respectively. The dissolved oxygen concentration under reference conditions is written as $[O_2]^{ref}$. There is a difference between the electron and proton potential of $\Delta\Phi_{c,eq}$ under reference equilibrium conditions. The rate of conversion of oxygen in a single agglomerate can be expressed as

$$W_{ARc} = S_{aggl}\, N_{O_2}. \tag{3.7}$$

Combining Eqs. (3.1), (3.2), (3.3), (3.4) and (3.7) leads to

$$\nabla\cdot\vec{j_c} = \frac{3(1-\pi_5)}{4\pi R_{aggl}^3}\, W_{ARc}\, 4F. \tag{3.8}$$

Combining Eqs. (3.5), (3.6) and (3.8) yields

$$\begin{aligned}\nabla\cdot\vec{j_c} = (1-\pi_5)&\frac{3}{R_{aggl}^2}\, 4F\, D_A\, [O_2]^s \\ &\left(1-\sqrt{\tfrac{i_{0,c}}{4F}\tfrac{1}{[O_2]^{ref}}\exp\left(-\tfrac{\alpha_c z_c F}{RT}\left(\Phi_e-\Phi_p-\Delta\Phi_{c,eq}\right)\right)\tfrac{a}{D_A}}R_{aggl}\right. \\ &\left.\coth\sqrt{\tfrac{i_{0,c}}{4F}\tfrac{1}{[O_2]^{ref}}\exp\left(-\tfrac{\alpha_c z_c F}{RT}\left(\Phi_e-\Phi_p-\Delta\Phi_{c,eq}\right)\right)\tfrac{a}{D_A}}R_{aggl}\right).\end{aligned} \tag{3.9}$$

In the following, the right-hand side of Eq. (3.9) is denoted as *RHS*9.

3.4.2 Anodic reaction

In the anodic catalyst, it is assumed that the active surface area is well exposed to the stream of hydrogen. The molar rate of conversion is given by the product of the available surface area and the surface reaction rate [15]

$$W_{ARa} = \frac{4}{3}\pi R_{aggl}^3\, a\, (-k_a''[H_2]^s). \tag{3.10}$$

The hydrogen oxidation is described using a Tafel equation

$$k_a'' = \frac{i_{0,a}}{2F}\frac{1}{[H_2]^{ref}}\exp\left(\frac{\alpha_a z_a F}{RT}\left(\Phi_e - \Phi_p - \Delta\Phi_{a,eq}\right)\right). \tag{3.11}$$

For the divergence of the current density, it follows in analogy to Eq. (3.8) that

$$\nabla \cdot \vec{j}_a = \frac{3(1-\pi_3)}{4\pi R_{aggl}^3} W_{ARa}\, 2F. \tag{3.12}$$

Combining Eq. (3.10), Eq. (3.11) and Eq. (3.12) yields

$$\nabla \cdot \vec{j}_a = -(1-\pi_3)\, a\, i_{0,a} \frac{[H_2]^s}{[H_2]^{ref}} \exp\left(\frac{\alpha_a z_a F}{RT}\left(\Phi_e - \Phi_p - \Delta\Phi_{a,eq}\right)\right). \tag{3.13}$$

In the following, the right-hand side of Eq. (3.13) is denoted as $RHS13$.

3.4.3 Charge transport

The electrochemical potential of the proton-conducting polymer and the electron-conducting phase is evaluated by the Poisson equation, Eq. (2.39). In the anodic catalyst layer, electrons are transfered from hydrogen molecules to the conduction band of the electron-conducting carbon phase by the hydrogen oxidation reaction. The electrons are transfered via the external electric circuit to the cathode side. Consequently the following equation is defined in subdomains $\Omega_2, \Omega_3, \Omega_5$ and Ω_6

$$\nabla \cdot [-\sigma_{e,\kappa} \nabla \phi_e] = Q_{e,C} \; in \; \Omega_\kappa \; , \; \kappa = 2,3,5,6. \tag{3.14}$$

The electrical potential of the carbon phase is ϕ_e. $\sigma_{e,\kappa}$ denotes the electronic conductivity of subdomain κ. The source term of the charge balance is defined as

$$Q_{e,C} = \begin{cases} RHS13 & in\ \Omega_3 \\ RHS9 & in\ \Omega_5 \\ 0 & elsewhere. \end{cases} \tag{3.15}$$

The boundary conditions for the electron current balance are

$$\phi_e = \begin{cases} 0 & at\ \partial\Omega_4 \\ V_{cell} & at\ \partial\Omega_{21} \end{cases} \tag{3.16}$$

and

$$[-\sigma_{e,\kappa} \nabla \phi_e] \cdot \vec{n} = 0 \tag{3.17}$$

at $\partial\Omega_{10}$, $\partial\Omega_{13}$ and the remaining outer boundaries of the gas diffusion layers and the catalyst layers. $\vec{n}$ represents the outward pointing normal vector of each boundary. At the interfaces between gas diffusion layers and catalyst layers, the continuity of the electron current density and the potential ϕ_e holds. A similar equation for the proton transport is used in the membrane and the catalyst layers

$$\nabla \cdot [-\sigma_{p,\kappa} \nabla \phi_p] = Q_{p,C} \; in \; \Omega_\kappa \; , \; \kappa = 3,4,5. \tag{3.18}$$

Again, ϕ_p and $\sigma_{p,\kappa}$ denote the potential and the conductivity of the proton-conducting phase in subdomain κ, respectively. The source terms are defined as

$$Q_{p,C} = \begin{cases} -RHS13 & in\ \Omega_3 \\ -RHS9 & in\ \Omega_5 \\ 0 & elsewhere. \end{cases} \tag{3.19}$$

The boundary conditions for the ionic current balance are

$$[-\sigma_{p,\kappa}\nabla\phi_p]\,\vec{n} = 0 \tag{3.20}$$

at all outer boundaries of the membrane and the catalyst layers as well as at the interfaces between the catalyst layers and the gas diffusion layers. At the interfaces between the membrane and the catalyst layers, the continuity of ϕ_p and the ionic current density holds.

3.4.4 Multicomponent mass transport

Cathode

The cathode side of the fuel cell model consists of the subdomains $\Omega_5, \Omega_6, \Omega_7$ and Ω_9. The mass balance at the cathode is described by the divergence of the diffusive mass flux. The cathodic gas diffusion layer is open to ambient air. No external gas pressure is applied. Hence the convective motion of the species within the cathode is neglected. The diffusive mass flux of species i, where $i = O_2, H_2O, N_2$, is described using the Maxwell-Stefan equation. The derivation of this equation is given in section 2.3. In contrast to the general formulation of Eq. (2.26), the cross-effects of pressure diffusion and thermal diffusion are neglected. The pressure diffusion is negligible due to the very small pressure difference [15]. The thermal diffusion, which is known as the Soret effect, can be neglected for the temperature gradients that typically occur in PEMFCs. This yields

$$\nabla\cdot\left[-\rho_c w_i \sum_{j=1}^{N} D_{ij}\frac{M_c}{M_j}\left(\nabla w_j + w_j\frac{\nabla M_c}{M_c}\right)\right] = Q_{i,M}\ in\ \Omega_k\ , \tag{3.21}$$

where $\kappa = 5,6,7,9$ and ρ_c denotes the density of the gas mixture

$$\rho_c = M_c\frac{P_{ref}}{RT}. \tag{3.22}$$

M_c is the total molar mass of the gas mixture given by

$$M_c = M_{O_2}\,x_{O_2} + M_{H_2O}\,x_{H_2O} + M_{N_2}\,x_{N_2}. \tag{3.23}$$

M_j denotes the molar mass of species j, where $j = O_2, H_2O, N_2$. The mass fraction of species j is denoted as w_j. Since

$$w_{O_2} + w_{H_2O} + w_{N_2} = 1 \tag{3.24}$$

only two independent equations of the form of Eq. (3.21) remain, which were chosen to be the equations for oxygen and water vapor. The multicomponent Fick diffusivities D_{ij} are functions of the gas composition. They are given by the expressions

$$D_{O_2O_2} = -\frac{\frac{(w_{H_2O}+w_{N_2})^2}{x_{O_2}\,\mathcal{D}_{H_2ON_2}} + \frac{w_{H_2O}^2}{x_{H_2O}\,\mathcal{D}_{O_2N_2}} + \frac{w_{N_2}^2}{x_{N_2}\,\mathcal{D}_{O_2H_2O}}}{\frac{x_{O_2}}{\mathcal{D}_{O_2H_2O}\,\mathcal{D}_{O_2N_2}} + \frac{x_{H_2O}}{\mathcal{D}_{O_2H_2O}\,\mathcal{D}_{H_2ON_2}} + \frac{x_{N_2}}{\mathcal{D}_{O_2N_2}\,\mathcal{D}_{H_2ON_2}}} \tag{3.25}$$

and

$$D_{O_2H_2O} = \frac{\frac{w_{O_2}\,(w_{H_2O}+w_{N_2})}{x_{O_2}\,\mathcal{D}_{H_2ON_2}} + \frac{w_{H_2O}\,(w_{O_2}+w_{N_2})}{x_{H_2O}\,\mathcal{D}_{O_2N_2}} - \frac{w_{N_2}^2}{x_{N_2}\,\mathcal{D}_{O_2H_2O}}}{\frac{x_{O_2}}{\mathcal{D}_{O_2H_2O}\,\mathcal{D}_{O_2,N_2}} + \frac{x_{H_2O}}{\mathcal{D}_{O_2H_2O}\,\mathcal{D}_{H_2ON_2}} + \frac{x_{N_2}}{\mathcal{D}_{O_2N_2}\,\mathcal{D}_{H_2ON_2}}}\,. \tag{3.26}$$

The multicomponent diffusivities for different combinations of species are obtained by permutation of indices. The $\mathcal{D}_{ij}$ denote the Maxwell-Stefan diffusivities that can be estimated from the kinetic theory of gases. It is assumed that only binary collisions occur. The mean free path length is assumed to be much longer than the molecular diameter. According to [45], the temperature and pressure dependence of the Maxwell-Stefan diffusivities is given by

$$\mathcal{D}_{ij} = 3.16 \cdot 10^{-8} \frac{T^{1.75}}{p\,(v_i^{1/3} + v_j^{1/3})} \left(\frac{\pi_\kappa}{\tau_\kappa}\right) \left(\frac{1}{M_i} + \frac{1}{M_j}\right)^{1/2}. \tag{3.27}$$

The diffusion volume of species i is denoted as v_i. π_κ and τ_κ are the porosity and tortuosity of subdomain κ. In Eq. (3.21), $Q_{i,M}$ is the source term for the mass balance of species i at the cathode side

$$Q_{O_2,M} = \begin{cases} \frac{M_{O_2}}{4F} \cdot RHS9 & in\ \Omega_5 \\ 0 & elsewhere \end{cases} \tag{3.28}$$

$$Q_{H_2O,M} = \begin{cases} -\frac{M_{H_2O}}{2F} \cdot RHS9 & in\ \Omega_5 \\ 0 & elsewhere\,. \end{cases} \tag{3.29}$$

Ambient air diffuses into the cell at the boundaries $\partial\Omega_{26}$ and $\partial\Omega_{28}$. The weight fraction of oxygen and water vapor at the outer cell surface are $w_{O_2}^{in}$ and $w_{H_2O}^{in}$. Hence the boundary conditions are

$$w_{O_2} = w_{O_2}^{in} \; at \; \partial\Omega_{26}, \partial\Omega_{28} \tag{3.30}$$

$$w_{H_2O} = w_{H_2O}^{in} \; at \; \partial\Omega_{26}, \partial\Omega_{28}. \tag{3.31}$$

The interface between the cathode catalyst layer and the membrane is boundary $\partial\Omega_{13}$. The following boundary condition for the weight fraction of water is applied

$$\begin{aligned} w_{H_2O}^{c} = &\left(M_{H_2O} M_{RSO} P_{sat} w_{H_2O}^{m} \left(M_{O_2}\left(w_{O_2} - 1\right) - M_{N_2} w_{O_2}\right)\right) \cdot \\ &\cdot \Big(M_{O_2}(M_{N_2} M_{RSO} P_{sat} w_{H_2O}^{m} + M_{H_2O}(Z M_{N_2} P_{ref} \cdot \\ &\cdot \left(w_{H_2O}^{m} - 1\right) - M_{RSO} P_{sat} w_{H_2O}^{m}))\Big)^{-1}. \end{aligned} \tag{3.32}$$

The derivation of this formula is given in the appendix. For the weight fraction of oxygen at the interface $\partial\Omega_{13}$,

$$\left[-\rho_c w_{O_2} \sum_{j=1}^{N} D_{O_2 j} \frac{M_c}{M_j} \left(\nabla w_j + w_j \frac{\nabla M_c}{M_c}\right)\right] \cdot \vec{n} = 0 \, . \tag{3.33}$$

Symmetric boundary conditions apply for the remaining outer boundaries of the cathode compartment:

$$\left[-\rho_c w_i \sum_{j=1}^{N} D_{ij} \frac{M_c}{M_j} \left(\nabla w_j + w_j \frac{\nabla M_c}{M_c}\right)\right] \cdot \vec{n} = 0 \; , \; i = O_2, H_2O, N_2 \, . \tag{3.34}$$

Anode

The anode side consists of the subdomains Ω_1, Ω_2 and Ω_3. The gaseous species that are present at the anode are H_2 and H_2O. In analogy to the description of the cathode, a mass balance is set up using the Maxwell-Stefan approach. Unlike Eq. (3.21), the mass balance for the anode side contains an additional term that accounts for the convective flux of hydrogen within the gas channel. The mass balance on the anode side is given by

$$\nabla \cdot \left[-\rho_a w_i \sum_{j=1}^{N} D_{ij} \frac{M_a}{M_j} \left(\nabla w_j + w_j \frac{\nabla M_a}{M_a}\right) + \rho_a w_i \vec{u}\right] = Q_{i,M} \; in \; \Omega_k, \tag{3.35}$$

where $\kappa = 1,2,3$. The density of the gas mixture at the anode side ρ_a is given by

$$\rho_a = M_a \frac{P_{ref}}{RT}. \tag{3.36}$$

M_a denotes the total molar mass of the gas mixture, that is

$$M_a = M_{H_2} x_{H_2} + M_{H_2O} x_{H_2O}. \tag{3.37}$$

The source terms for hydrogen are given by

$$Q_{H_2,M} = \begin{cases} \frac{M_{H_2}}{2F} \cdot RHS13 & in\ \Omega_3 \\ 0 & elsewhere. \end{cases} \tag{3.38}$$

The electrochemical reaction on the anode side does not produce any water. Hence the source term of water is given by

$$Q_{M_{H_2O},M} = O \tag{3.39}$$

in all subdomains of the anode compartment. Since $w_{H_2} + w_{H_2O} = 1$, one independent equation of the form of Eq. (3.35) remains. The symmetric diffusivities are

$$D_{H_2H_2} = -\frac{w_{H_2O}^2}{x_{H_2} x_{H_2O}}\ \mathcal{D}_{H_2H_2O} \tag{3.40}$$

and

$$D_{H_2H_2O} = -\frac{w_{H_2} w_{H_2O}}{x_{H_2} x_{H_2O}}\ \mathcal{D}_{H_2H_2O}\ . \tag{3.41}$$

The Maxwell-Stefan diffusivity is given by Eq. (3.27).
In the gas channel, the convective flux is calculated using Hagen-Poiseuille's law. The velocity of the hydrogen and water mixture is $\vec{u} = e_x u_x + e_y u_y$ where $u_x = 0$ and

$$u_y = \begin{cases} -4x(x-1)\Delta p\, d^2/16\, l\, \mu & in\ \Omega_1 \\ 0 & elsewhere. \end{cases} \tag{3.42}$$

The Cartesian co-ordinate x ranges from $x = 0$ to $x = 1$. Δp represents the pressure difference applied between the channel inlet and outlet. The length and width of the channel are denoted as l and d, respectively. μ is the dynamic viscosity of the gas.
At boundary $\partial\Omega_2$, the hydrogen is fed into the gas channel, resulting in

$$w_{H_2} = w_{H_2}^{in}\ at\ \partial\Omega_2. \tag{3.43}$$

At boundary $\partial\Omega_3$, the gas leaves the cell by convection. At the interface between anode and membrane $\partial\Omega_{10}$, the following boundary condition applies:

$$w_{H_2} = 1 - (M_{H_2O} M_{RSO} P_{sat} w^m_{H_2O}) \cdot \cdot \left(Z M_{H_2} M_{H_2O} P_{ref} \left(1 - w^m_{H_2O}\right) + M_{RSO} P_{sat} w^m_{H_2O} \left(M^m_{H_2O} - M_{H_2}\right)\right)^{-1}. \quad (3.44)$$

The derivation of this formula is given in the appendix. The following boundary condition applies at the interfaces $\partial\Omega_1$, $\partial\Omega_5$, $\partial\Omega_6$, $\partial\Omega_8$ and $\partial\Omega_9$:

$$\left[-\rho_a w_{H_2} \sum_{j=1}^{N} D_{H_2 j} \frac{M_a}{M_j} \left(\nabla w_j + w_j \frac{\nabla M_a}{M_a} \right) + \rho_a w_{H_2} \vec{u} \right] \cdot \vec{n} = 0. \quad (3.45)$$

Membrane

Three species, H_2O, H^+ and RSO representing the polymer, are assumed to be present within the membrane. The migration of protons through the membrane is given as the solution of Eq. (3.18). The transport of water through the membrane is a superposition of diffusive and hydraulic transport and electro-osmotic drag. In this model, an approach based on the work of Fuller and Newman [31] is used. The mass balance of water within the membrane is consequently described by the divergence of the water flux due to diffusion and electro-osmotic drag

$$\nabla \cdot \left[-\rho_m w_i \sum_{j=1}^{2} D_{ij} \frac{M_m}{M_j} \left(\nabla w_j + w_j \frac{\nabla M_m}{M_m} \right) + \Gamma_{drag} \right] = 0 \ in \ \Omega_4. \quad (3.46)$$

ρ_m denotes the density of the membrane given by

$$\rho_m = M_m \frac{P_{ref}}{RT}. \quad (3.47)$$

M_m means the total molar mass of the membrane defined by

$$M_m = M_{RSO}\, x_{RSO} + M_{H_2O}\, x_{H_2O}. \quad (3.48)$$

Again M_j denotes the molar mass of species j, where j can be H_2O or RSO. Since $w_{H_2O} + w_{RSO} = 1$, the mathematical model contains just the equation describing the water flux. The symmetric diffusivities follow by analogy from Eqs. (3.40) and (3.41). The Maxwell-Stefan diffusivity $\mathcal{D}_{ij}$ is a function of the membrane humidity λ and the temperature T. According to [46], the $\mathcal{D}_{ij}$ can be expressed as

$$\mathcal{D}_{H_2O\ RSO} = \mathcal{D}^0_{H_2O\ RSO}(T^0) \cdot \lambda \ \exp\left[-\frac{E^A_{H_2O,RSO}}{R} \left(\frac{1}{T} - \frac{1}{T^0} \right) \right]. \quad (3.49)$$

The membrane humidity λ is defined as the number of water molecules per sulfonic acid group

$$\lambda = \left(\frac{x_{H_2O}}{1 - x_{H_2O}} \right), \tag{3.50}$$

where x_{H_2O} is the molar fraction of water within the membrane. The electro-osmotic drag is accounted for by the vector Γ_{drag}, defined as

$$\Gamma_{drag} = \begin{pmatrix} M_{H_2O}\, n_{drag}\, \sigma_{p,4} F^{-1} \nabla_x \phi_p \\ 0 \end{pmatrix}. \tag{3.51}$$

M_{H_2O} and F denote the molar mass of water and the Faraday constant, respectively. ϕ_p is the protonic potential and $\sigma_{p,4}$ the protonic conductivity in subdomain Ω_4. The work of Lee, Shimpalee and Van Zee [41] indicates that the constitutive equations for conductivity and electro-osmotic drag developed by Springer et al. [25] for Nafion can be applied to Gore membrane electrode assemblies. Schmitz et al. [44] used a PRIMEA 5510 from Gore Associates for the cell modeled in this work. Hence the number of water molecules dragged across the membrane per proton is given by

$$n_{drag} = \frac{2.5}{22}\, \lambda\,. \tag{3.52}$$

The protonic conductivity $\sigma_{p,4}$ of the membrane used in Eq. (3.51) depends on the water content according to

$$\sigma_{p,4} = 10^2 \exp\left[1286 \left(\frac{1}{303} - \frac{1}{T} \right) \right] (0.005139\lambda - 0.00326). \tag{3.53}$$

The membrane equations are coupled to the electrode equations via boundary conditions. In this study, it is assumed that the water content of the membrane is determined by the humidity of the gases within the electrodes. The boundary condition of the mass balance at the cathode interface $\partial\Omega_{13}$ is

$$\begin{aligned} w^m_{H_2O} = {} & (Z M_{H_2O} M_{N_2} M_{O_2} P_{ref} w^c_{H_2O}) \cdot \\ & \cdot \Big(M_{N_2} M_{O_2} M_{RSO} P_{sat} w^c_{H_2O} + M_{H_2O} (M_{N_2} M_{RSO} P_{sat} w_{O_2} + \\ & + M_{O_2} (Z M_{N_2} P_{ref} w^c_{H_2O} - M_{RSO} P_{sat} (w^c_{H_2O} + w_{O_2} - 1))) \Big)^{-1}. \end{aligned} \tag{3.54}$$

At the anode interface $\partial\Omega_{10}$ it is

$$\begin{aligned} w^m_{H_2O} = {} & (Z M_{H_2} M_{H_2O} P_{ref} w^a_{H_2O}) \cdot \\ & \cdot \Big(M_{H_2} M_{RSO} P_{sat} w^a_{H_2O} + M_{H_2O} (Z M_{H_2} P_{ref} w^a_{H_2O} + \\ & + M_{RSO} (P_{sat} - P_{sat} w^a_{H_2O})) \Big)^{-1}. \end{aligned} \tag{3.55}$$

The physical meaning of $w^m_{H_2O}$ is the mass fraction of water in the membrane. The derivation of Eq. (3.54) and Eq. (3.55) is given in the appendix. Symmetric boundary conditions are set at the remaining boundaries of the membrane

$$\left[-\rho_m w_{H_2O} \sum_{j=1}^{2} D_{H_2Oj} \frac{M_m}{M_j} \left(\nabla w_j + w_j \frac{\nabla M_m}{M_m} \right) + \Gamma_{drag} \right] \cdot \vec{n} = 0 \tag{3.56}$$

where $\vec{n}$ denotes the outward pointing normal vector of the interface.

3.4.5 Heat transport

The heat transport equation is solved for all parts of the cell. To be consistent with the description of the mass transfer, the convective heat transfer is neglected. The dominating process is heat conduction. The heat balance equation that results from Eq. (2.50) is

$$\nabla \cdot [-k_\kappa \nabla T] = Q_H \text{ in } \Omega_\kappa, \tag{3.57}$$

where k_κ denotes the thermal conductivity of subdomain κ. The heat balance is solved for all parts of the fuel cell corresponding to $\kappa = 1,2,3,4,5,6,8$. In the reaction layers, heat is generated due to the reaction entropy, activation energy loss and resistive heating. Within all other conductive subdomains, only resistive heating is accounted for. Accordingly the source terms are defined as

$$Q^H = \begin{cases} -\sigma_{e,2} [\nabla \phi_e]^2 & \text{in } \Omega_2 \\ \frac{\Delta S_a T}{2F} \cdot RHS13 - \eta_a \cdot RHS13 - \sigma_{e,3} [\nabla \phi_e]^2 - \sigma_{p,3} [\nabla \phi_p]^2 & \text{in } \Omega_3 \\ -\sigma_{p,4} [\nabla \phi_p]^2 & \text{in } \Omega_4 \\ \frac{\Delta S_c T}{4F} \cdot RHS9 + \eta_c \cdot RHS9 - \sigma_{e,5} [\nabla \phi_e]^2 - \sigma_{p,5} [\nabla \phi_p]^2 & \text{in } \Omega_5 \\ -\sigma_{e,6} [\nabla \phi_e]^2 & \text{in } \Omega_6 \\ 0 & \text{elsewhere.} \end{cases} \tag{3.58}$$

In Eq. (3.58), the overvoltage at the anode and cathode is given by $\eta_a = \phi_e - \phi_p$ and $\eta_c = \phi_e - \phi_p - \Delta\phi_{c,eq}$ respectively. The boundary conditions of the heat transfer equation reflect the heat exchange between the fuel cell and its surroundings by free convection and radiation. Due to the large surface-to-volume ratio of planar fuel cells, the temperature of the cell is low and free convection dominates. At the outer boundaries of the solid parts of the cell, the heat flux is given by

$$[-k_\kappa \cdot \nabla T] \cdot \vec{n} = -\alpha_w (T - T_S) - \varepsilon_b \sigma_{SB} (T^4 - T_S^4) \, . \tag{3.59}$$

Here α_w denotes the heat transfer coefficient of free convection, σ_{SB} the Stefan-Boltzmann constant, ε_b the emissivity of the fuel cell surface and T_s the temperature of the surrounding air. In Eq. (3.59), the first term on the right hand side

describes the heat exchange between the fuel cell and the surrounding air. The second term accounts for the radiative heat exchange between the fuel cell and its surroundings. At all other boundaries, the following condition applies:

$$[-k_\kappa \nabla T] \cdot \vec{n} = 0 \; . \tag{3.60}$$

3.5 Numerical solution method

The system of coupled partial differential equations was solved using the software package FEMLAB^{TM} [47]. Within the solution algorithm, the partial differential equations are coupled locally and solved simultaneously. The solution technique is based on the finite element method, where second-order Lagrange elements are used. Since the problem posed by the governing equations of this model is diffusion-dominated, a stiff differential equation system is obtained. In particular, the source terms of the charge balance used in this work represent strong non-linearities. Hence a non-linear solver based on an affine invariant form of the damped Newton method is used. Optionally, the solver applies a Broyden update formula according to a proposal by Deuflard [48]. It should be noted that the convergence behavior of this non-linear solver depends strongly on a carefully selected initial estimate of the solution.

3.6 Model validation and model parameters

As a result of the high complexity of the fuel cell, many parameters appear in the governing equations of the model outlined above. The results shown are obtained using a set of baseline parameters and constants listed in Tables Ia to Id. All material properties are set to values which describe the type of cell developed in [44]. Parameters responsible for the description of the electrochemical reaction and the water transport across the membrane are based on literature values. The references are indicated in Tables Ia to Id. A detailed discussion of important fuel cell model parameters is given in section 4.6. The model is validated by comparison of a measured current-voltage curve to the predictions of the model. The results are shown in Fig. 3.4. Excellent agreement is obtained between the measured IV-curve (a) and the simulated IV-curve (b). The model predictions of the overall cell performance in a range down to a cell voltage of 0.4 V are validated. At high current density, the formation of liquid water has to be taken into account. However, two-phase effects are beyond the scope of this model. A mathematical model that accounts for the transport of liquid water and the flooding of the gas diffusion layer is presented in the following chapter.
The cathode of the reference cell that is used in this work is covered partly by the

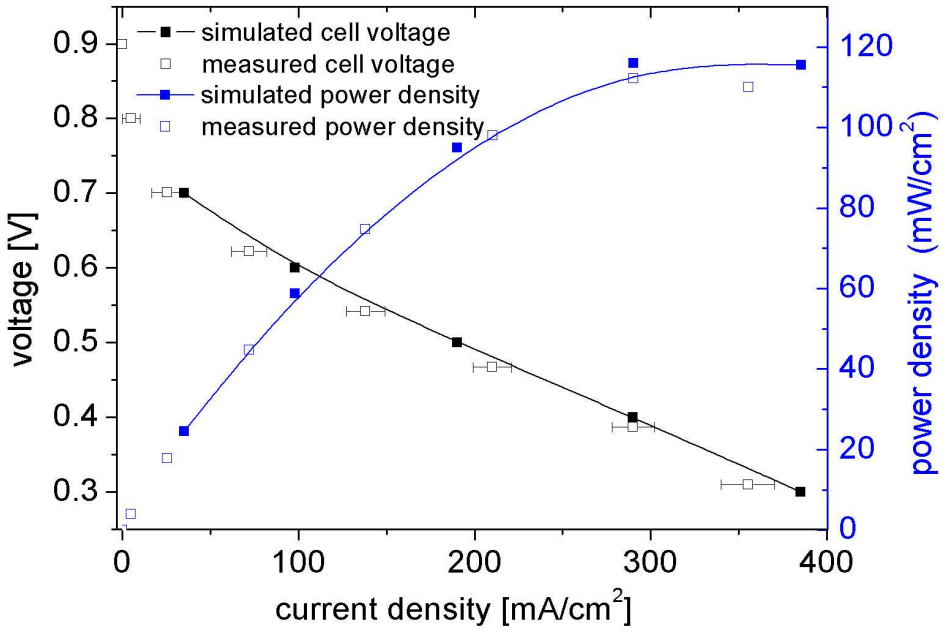

Figure 3.4: Comparison of measurement and simulation showing the excellent agreement between the measured values and the modeling results. In the simulation the cell voltage was varied in steps of 0.1 V between 0.7 V and 0.3 V. The high cell voltage region is omitted since the Tafel approximation is not valid there. The simulated current density is indicated by solid black squares. The simulated IV curve is indicated by the black interpolation line. The measured current density indicated by hollow black squares is corrected for losses due to the contact resistance. The bars indicate the standard deviation of the measured values. The simulated power density of the planar fuel cell is indicated by solid blue squares. The interpolation line indicates the simulated power density curve. The measurement values are indicated by hollow blue squares. The results of the simulation agree very well with the experimental values.

cathode end-plate but 80 % of the cathode area is exposed to ambient air. Hence, for this type of cell, the assumption is reasonable that two-phase effects are negligible at least down to a cell voltage of 0.4 V corresponding to a current density of about 300 mA/cm^2.
It is emphasized at this point that the geometry of the model domain shown in Fig. 3.1 corresponds to the geometry of the fuel cell used for the measurements. The reference fuel cell is shown in Fig. 3.2. Since the properties of the cell components and the cell geometry are known, the significance of the comparison between experiment and simulation is enhanced compared to the use of measurement data from literature sources for the purpose of validation. The power density of the cell is also depicted in Fig. 3.4. A planar self-breathing cell will probably be operated in the voltage range between 0.5 V to 0.4 V where the power density is highest. Therefore the model is used to study the behavior of the cell at a voltage of 0.4 V.

3.7 Operating behavior of planar fuel cells

In Fig. 3.5, the potential of the carbon phase ϕ_e is shown for the catalyst layer and the gas diffusion layer of the cathode side. The influence of the potential boundary condition $\phi_e = 0.4\,V$ applied at the rib in the cathode plate at $\partial\Omega_{21}$, is clearly visible. The potential of the carbon phase rises to about $0.42\,V$ between the ribs. The boundary condition at $\partial\Omega_{21}$ causes a potential gradient in the gas diffusion layer. Since the distance between two adjacent ribs is much larger than the thickness of the gas diffusion layer, the shape of the potential ϕ_e is dominated by the increase of ϕ_e between the ribs. Eq. (3.9) and Eq. (3.13) induce a coupling of the potential of the carbon phase ϕ_e and the potential of the polymer phase ϕ_p. The electric potential of the polymer phase ϕ_p is depicted in Fig. 3.7. The potential distribution of ϕ_p reflects the coupling of ϕ_e and ϕ_p causing a potential gradient of the polymer phase in the y-direction near the rib that is visible in Fig. 3.7. The shape of the potential distribution is dominated by the gradient of ϕ_p in the x-direction $\nabla_x\phi_p$, which is one order of magnitude larger than $\nabla_y\phi_p$. The reason is that the conductivity of the polymer phase is very low compared to the conductivity of the gas diffusion layer. On the anode side, there is only a potential gradient of the polymer phase in the x-direction. The potential of the polymer phase is lowest in the region under the rib, where the potential of the carbon phase is also lowest.
The electron current is shown in Fig. 3.8 using the conventional flow notation, i.e. the arrows point in the flow direction of positive charges. In the gas diffusion layer of the anode, the direction of the current is along the x-direction perpendicular to the membrane. The electrons are produced in the catalyst layer of the anode and move to boundary $\partial\Omega_4$ where ϕ_e is equal to 0 V. In the cathode, the fact that

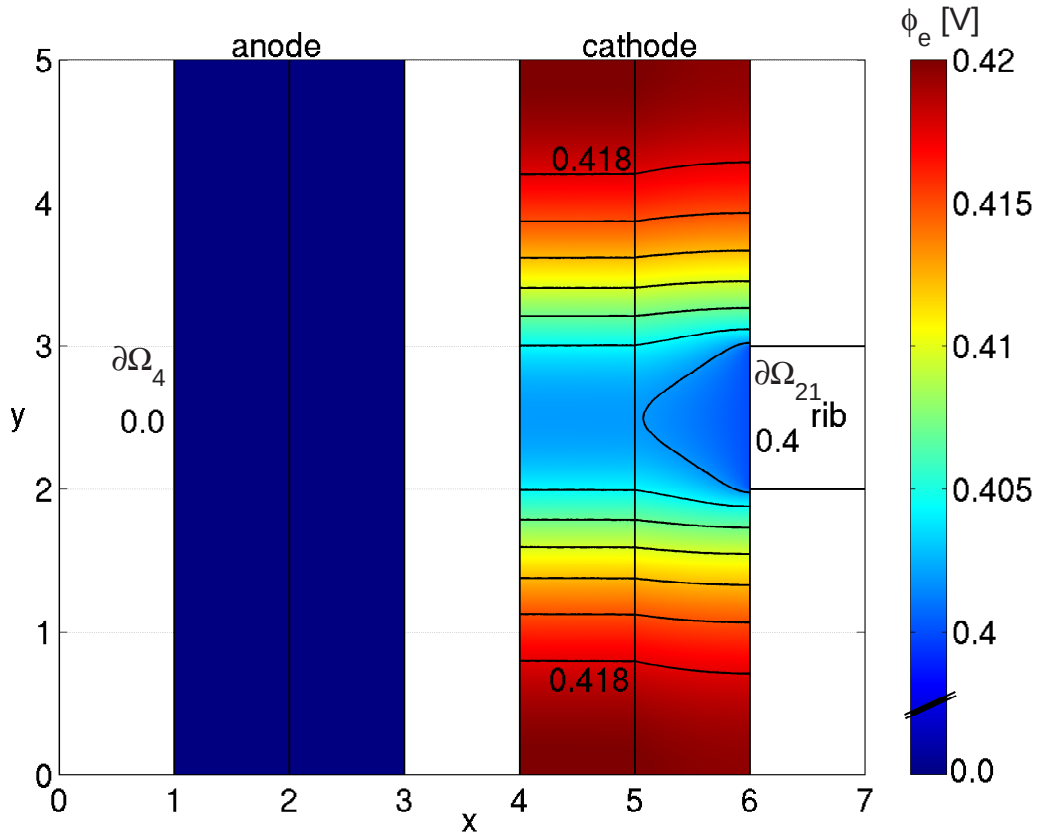

Figure 3.5: Distribution of the electrochemical potential in the carbon phase ϕ_e. Each point of the current-voltage curve corresponds to a fixed potential difference between the cathode side and the anode side. On the cathode side which is shown on the right hand side of the graph, the potential is applied at the rib in the cathode end-plate. This causes an increased potential in the areas between the ribs. The potential gradient along the *x*-direction is negligible compared to the gradient in the *y*-direction on the cathode side. Compared to the cathode side, ϕ_e is nearly constant on the anode side since the voltage is applied over the whole length of the geometrical domain. Normalized co-ordinates according to Fig. 3.1 are used.

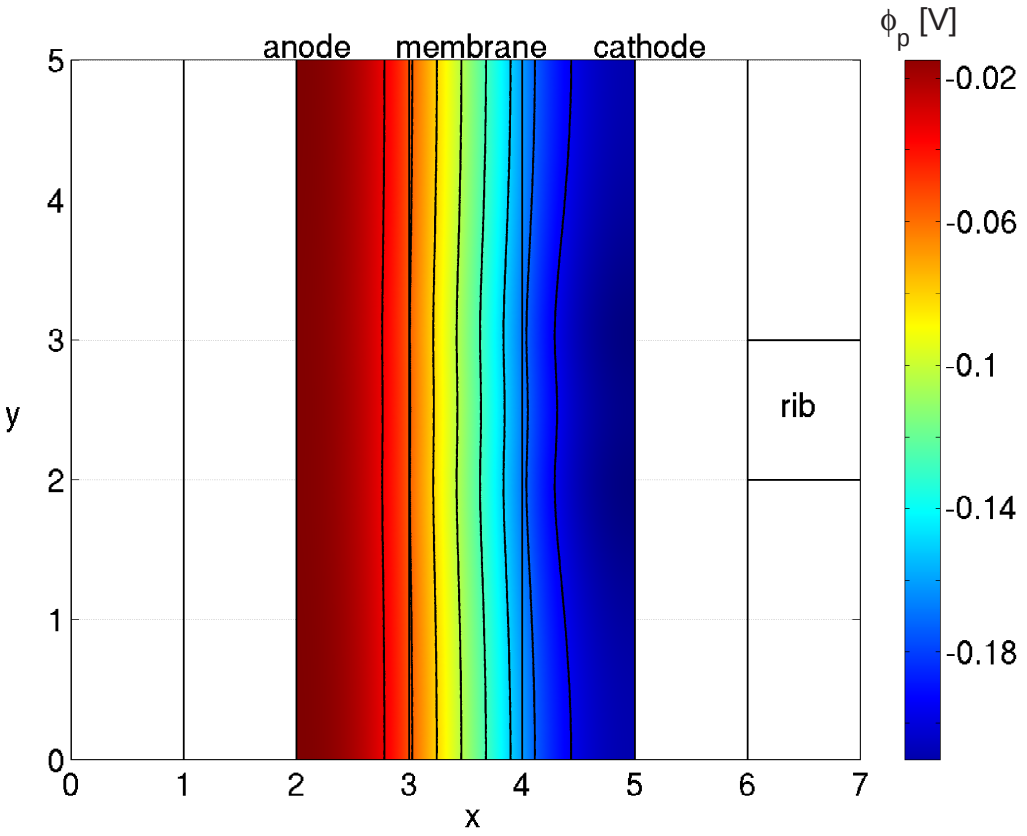

Figure 3.6: Distribution of the electrochemical potential in the polymer phase ϕ_p. Due to the coupling of ϕ_e and ϕ_p, the potential of the polymer phase ϕ_p is lowered in the catalyst layer under the rib. This drop of ϕ_p is significant for the activity of the catalyst layer. Normalized co-ordinates according to Fig. 3.1 are used.

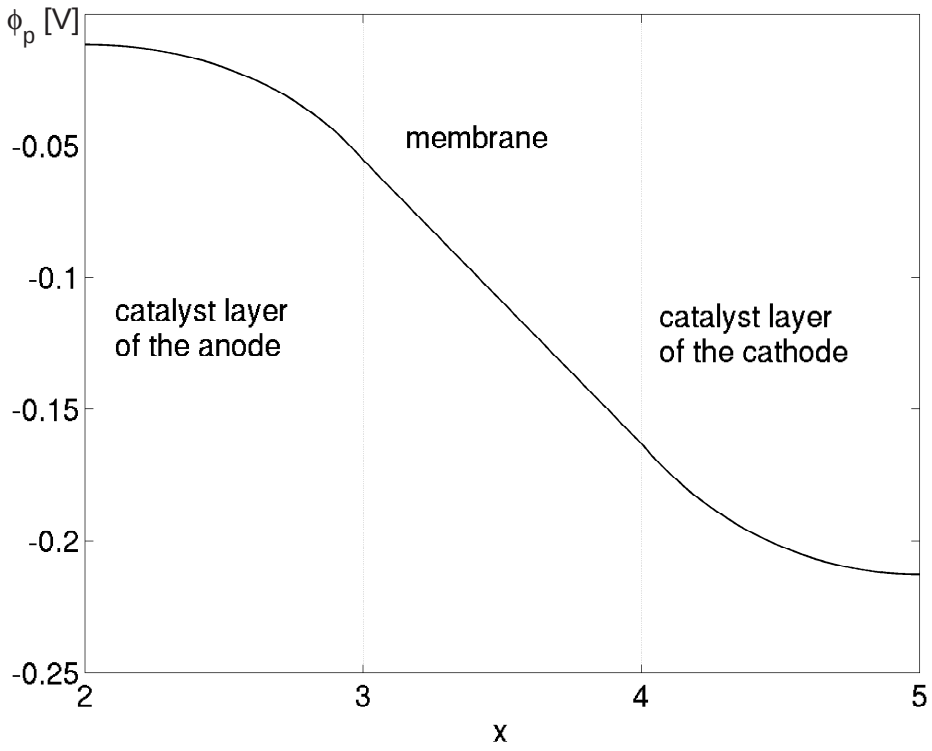

Figure 3.7: Cross-section of the electrochemical potential in the polymer phase ϕ_p at $y = 1$. Protons are generated by the hydrogen oxidation reaction in the catalyst layer of the anode side. No protons leave the catalyst layer of the anode towards the gas diffusion layer. Hence the gradient of ϕ_p at $x = 2$ is zero. A constant proton flux is transported through the membrane to the cathode side, where the protons are consumed in the oxygen reduction reaction. The consumption of protons is reflected in the decreasing gradient of ϕ_p in the catalyst layer of the cathode side between $x = 4$ and $x = 5$. In the membrane, the proton current is constant and equal to the electron current that is measured in the external electric circuit.

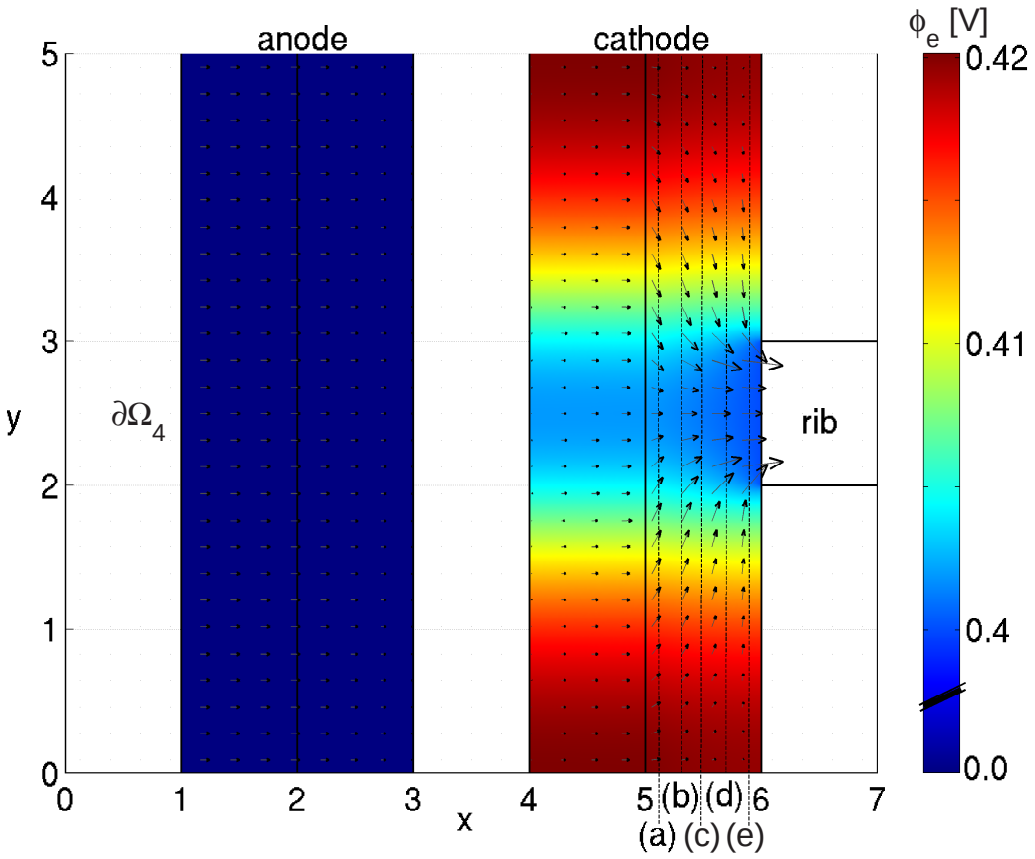

Figure 3.8: Flow of electron current in the carbon phase. The rib supplies electrons to an area which is five times larger than itself. This causes inhomogeneity of the current density. Conventional flow notation is used, i.e. the arrows indicate the flow direction of positive charges. The letters (a), (b), (c), (d) and (e) indicate the position of cross-sections that are shown in Fig. 3.9. The colors indicate the electronic potential ϕ_e. The gradient of ϕ_e along the *y*-direction causes a current that is perpendicular to the MEA. Normalized co-ordinates according to Fig. 3.1 are used.

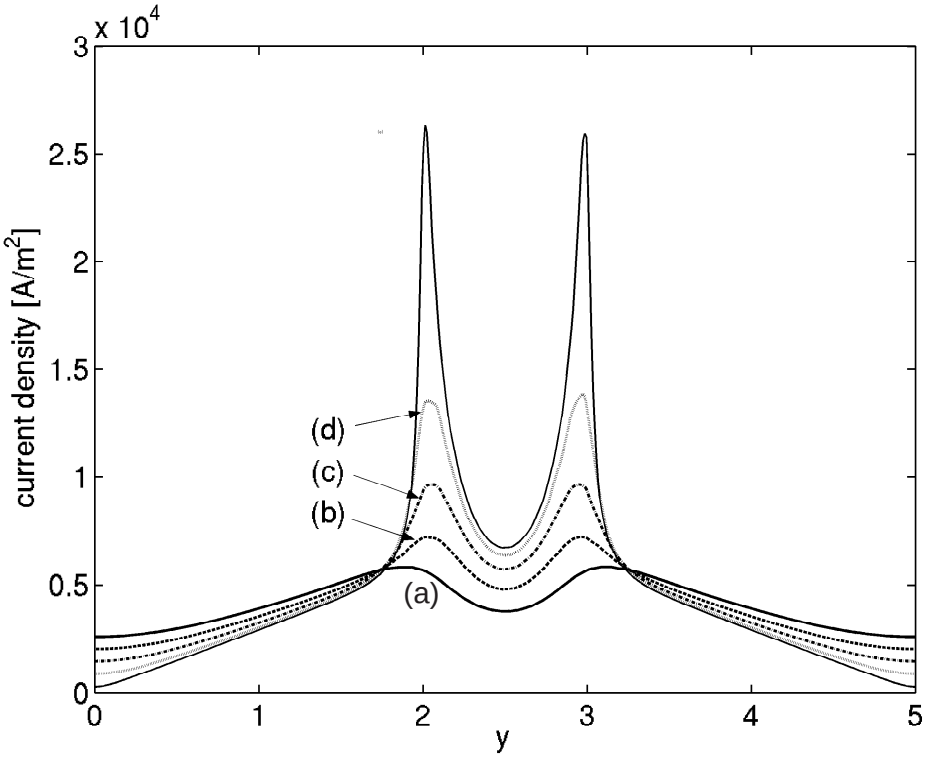

Figure 3.9: Absolute value of the current density at different positions in the gas diffusion layer of the cathode side. Normalized co-ordinates according to Fig. 3.1 are used for the abscissa. The cross-sections are determined at the following x-positions that are indicated in Fig. 3.8: (a) 5.1, (b) 5.3, (c) 5.5, (d) 5.7, (e) 5.9. This corresponds to the following distances in the x-direction from the cathode catalyst layer in the test cell: (a) 35 μm, (b) 105 μm, (c) 175 μm, (d) 245 μm, (e) 315 μm. The current density distribution is strongly non-uniform.

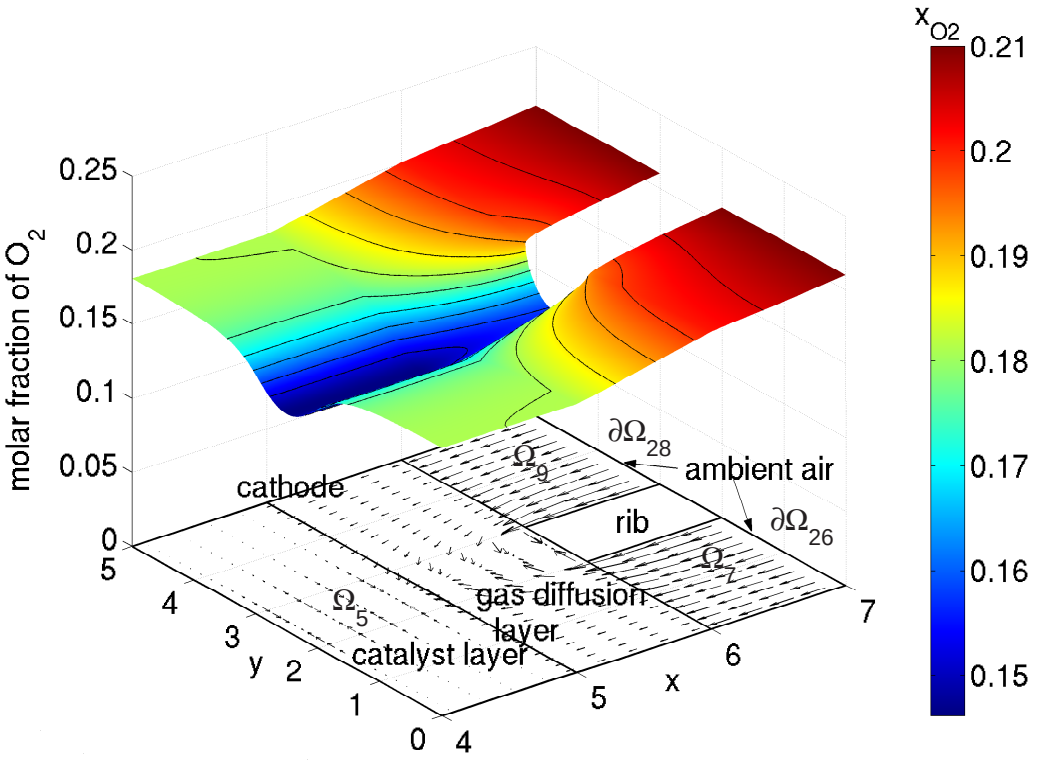

Figure 3.10: Spatial distribution of the molar fraction of oxygen. The rib represents a diffusion resistance to oxygen. This results in a substantial decrease in the oxygen molar fraction under the rib. The largest drop of the oxygen molar fraction occurs inside the gas diffusion layer due to its diffusional resistance. Nevertheless, the overall oxygen supply of the cathode is still sufficient at a cell voltage of 0.4 V. The molar flux of oxygen follows the gradient in the oxygen molar fraction. Hence the oxygen diffuses around the rib and the gas diffusion layer ensures the supply of the catalyst layer region that is covered by the rib. The catalyst layer is too thin to account for a significant drop of the oxygen molar fraction in the x-direction. It also cannot equilibrate the varying molar fraction along the y-direction. Normalized co-ordinates according to Fig. 3.1 are used.

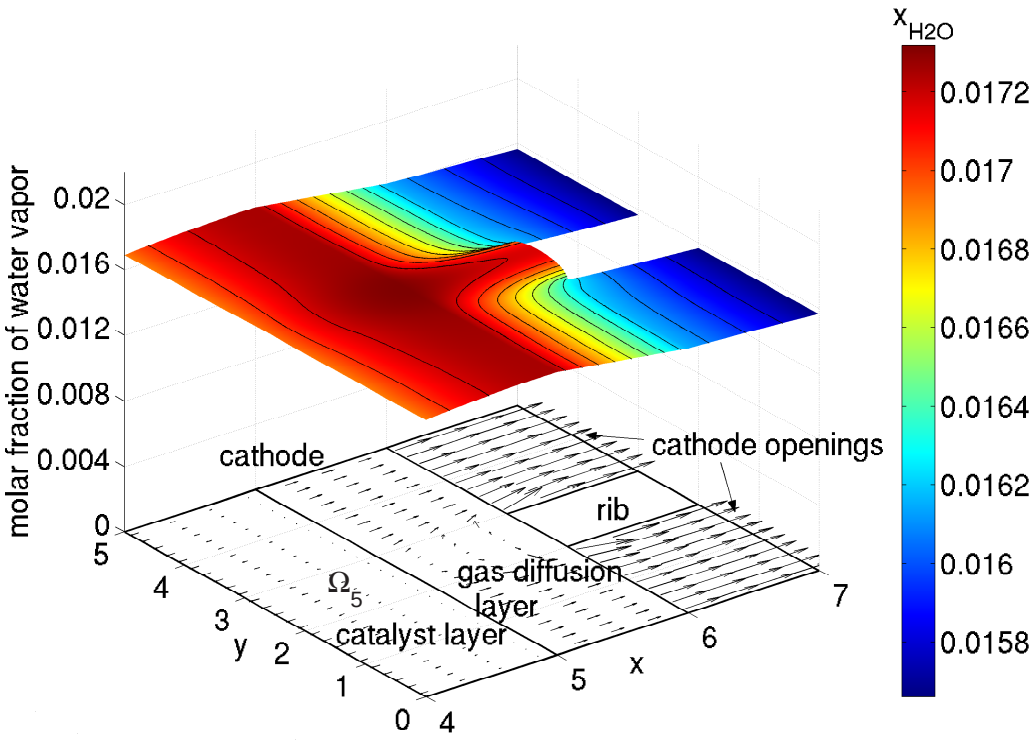

Figure 3.11: Spatial distribution of the molar fraction of gaseous water at the cathode. The rib prevents part of the water produced at the cathode from leaving the cell via the cathode openings. The maximum value of the molar fraction of gaseous water is located in the middle of the electrode under the rib. The average relative humidity in the cathode is 0.5. The arrows indicate that the water is forced to diffuse around the rib to leave the cell which increases diffusion length of the water vapor through the gas diffusion layer. Normalized co-ordinates according to Fig. 3.1 are used.

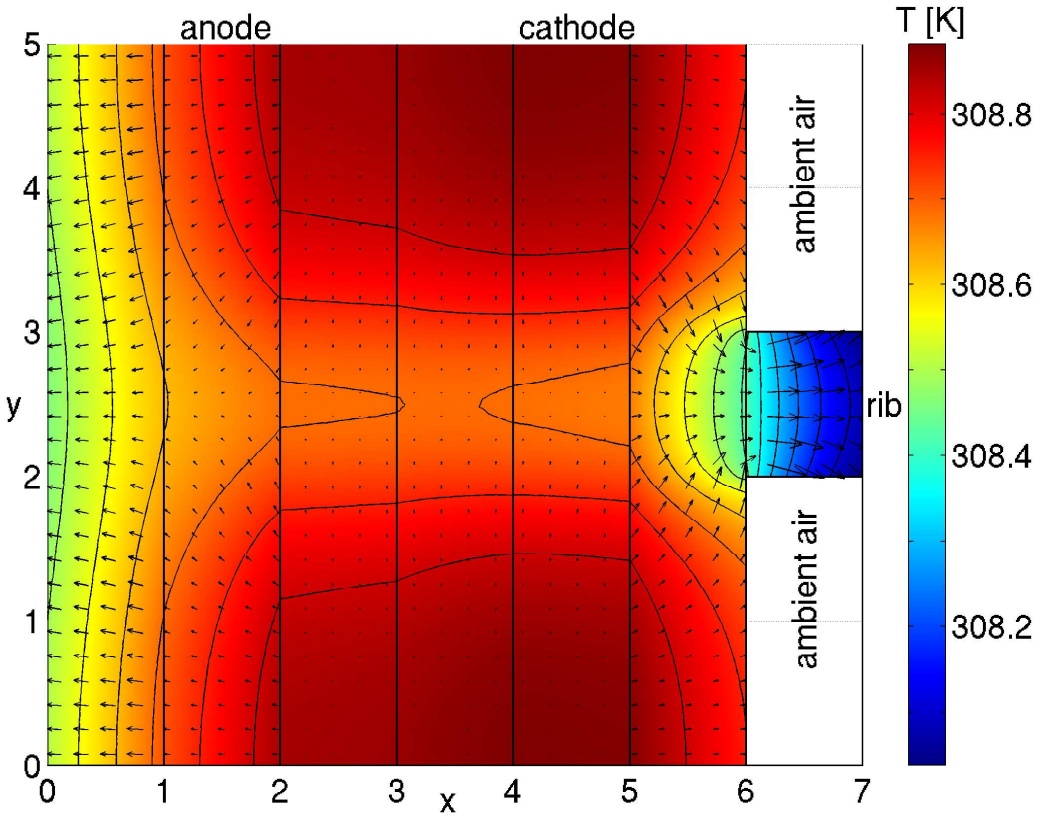

Figure 3.12: Temperature distribution in the planar cell. The overall temperature difference is only about 1 K at a cell voltage of 0.4 V and an average current density of 300 mA/cm^2. The shape of the temperature distribution is governed by the cooling influence of the rib. The arrows indicate the conductive heat flux.

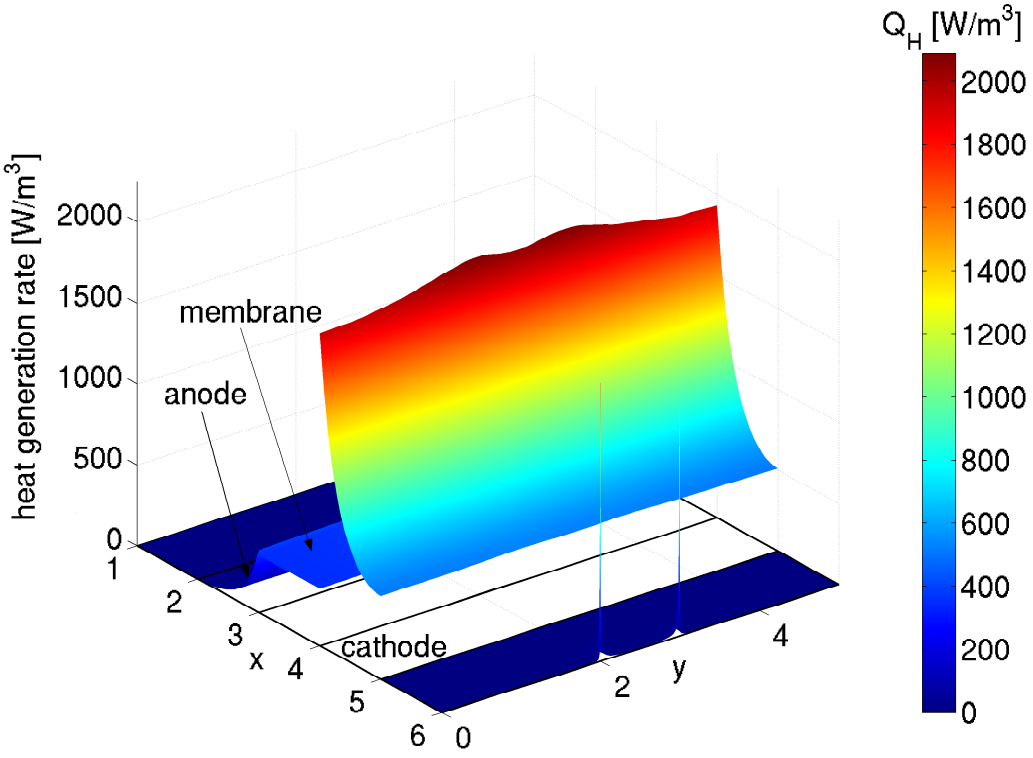

Figure 3.13: Heat generation in the fuel cell. The exothermic oxygen reduction at the cathode is the most important source of heat. Resistive heating is significant in the membrane and the catalyst layers. The non-uniform current density (Fig. 3.9) at the cathode causes increased resistive heating at the edges of the rib. Normalized co-ordinates according to Fig. 3.1 are used.

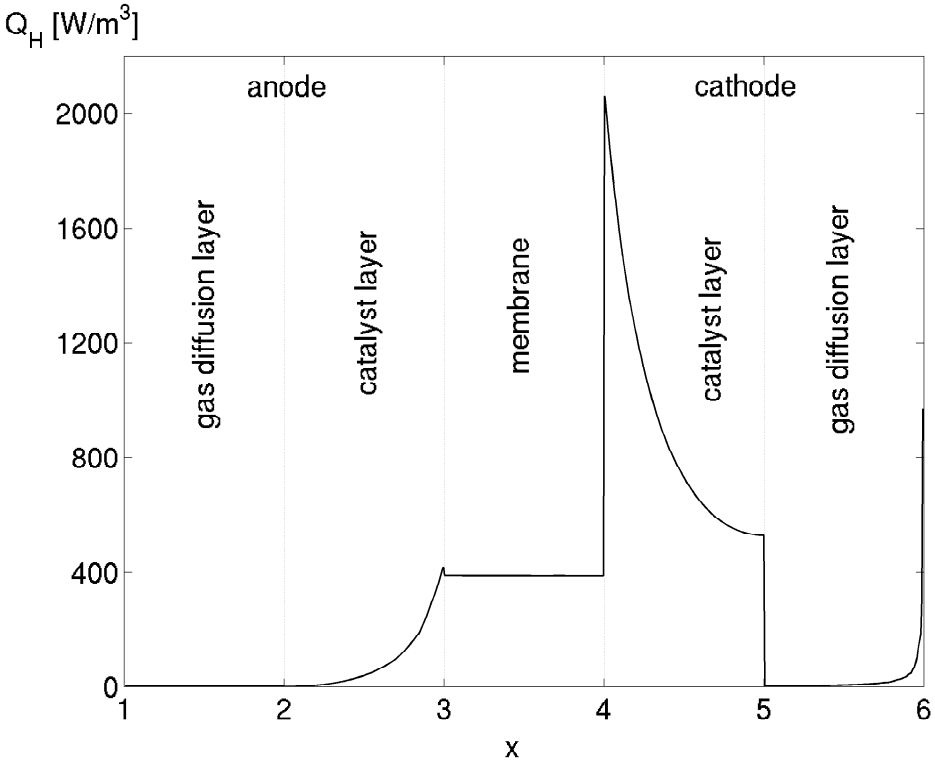

Figure 3.14: Cross-section along y=2 through Fig. 3.13. The graph highlights the importance of the heat of reaction on the cathode side. Compared to the waste heat of the oxygen reduction reaction, the resistive heating in the membrane and the catalyst layer of the anode side is small since the conductivity of the polymer is sufficient at a cell voltage of 0.4 V. However, due to the volume of the membrane being 2.5 times larger than the volume of the catalyst layer of each side, the contribution of the resistive heating in the membrane is important. The resistive heating in the gas diffusion layers is negligible unless the current density is very large compared to the average value. The increase of the heat generation at x=6 is due to the strongly increased current density at the edges of the ribs. However, the volume of this region is too small to have an impact on the temperature distribution of the cell.

the electrons are supplied not over the whole width of the electrode but via the rib only has a strong influence on the current flow. The supply of the regions between the ribs with electrons causes a current on the cathode side along the y-direction. This corresponds to the rise of the carbon-phase potential as shown in Fig. 3.5. The rib supplies an active area with electrons that is large in comparison to its own width. This leads to a locally increased current density. This effect increases with decreasing cell potential.

The absolute value of the current density at different positions in the gas diffusion layer of the cathode side is shown in Fig. 3.9. The cross-sections are taken along the y-direction of the cell as indicated in Fig. 3.8 by dashed lines in the gas diffusion layer. The closer to the rib the cross-section is taken, the more pronounced is the non-uniformity of the current density. The cross-section taken 35 μm under the rib (e) shows maxima which are about nine times as high as the mean current density of about 300 mA/cm^2 at $V_{cell} = 0.4$ V. The reason for this effect is the shape of the potential ϕ_e (see Fig. 3.5). A superposition of current flowing in the x-direction and the y-direction can be seen at the edges of the rib. With increasing distance from the rib, the non-uniformity becomes less pronounced, as curves (b), (c), and (d) show. Nevertheless, the cross-section determined at a distance of 35 μm from the catalyst layer of the cathode still shows two maxima. This indicates that the charge generation rate itself in the catalyst layer is non-uniform.

The rib in the cathode not only influences the potential and current distribution in the fuel cell but also shields part of the catalyst layer from the oxygen supply. Fig. 3.10 shows the spatial distribution of the molar fraction of oxygen in the cathode. The minimum value of the oxygen concentration is located under the middle of the rib. The oxygen supply is sufficient for all parts of the catalyst layer of the investigated cell. At a cell voltage of 0.4 V, the performance loss due the mass transfer resistance is small compared to the activation losses. The diffusive flux of oxygen is indicated by arrows in Fig. 3.10. On the cathode side the cell is open to ambient air at the boundaries $\partial\Omega_{26}$ and $\partial\Omega_{28}$. Oxygen diffuses into the voids Ω_7 and Ω_9 between the ribs. The gas diffusion layer distributes the oxygen to all parts of the active area Ω_5. The direction of the oxygen flux under the rib is almost perpendicular to the direction of the oxygen influx.

The spatial distribution of the molar fraction of gaseous water in the cathode is shown in Fig. 3.11. Water is produced only in the electrochemically active region of the cathode Ω_5. The product water is needed for the humidification of the membrane in order to maintain a high protonic conductivity. Here, the average relative humidity of the cathode is 0.5, which is sufficient to keep the membrane well humidified. Dry-out of the membrane becomes dominant if the relative humidity drops well below 0.4. However, if the gas mixture at the cathode side is saturated with water vapor, condensation forms liquid water. This causes a strong increase of the mass transfer resistance and flooding of the cell. The molar fraction of

gaseous water is highest under the rib. Liquid water is most likely to form there first at higher current densities. The diffusive flux of water is indicated by arrows in Fig. 3.11. The rib forces the diffusive outflux of water to bend around it. This results in an increased water concentration under the rib as shown in Fig. 3.11. At this operating point, some of the water diffuses through the membrane to the anode side of the cell.

The temperature distribution shown in Fig. 3.12 is dominated by the cooling effect of the rib. Due to the large surface-to-volume ratio, the overall temperature difference is only about 1 K at a cell voltage of 0.4 V and remains below 5 K for any current density. The average cell temperature is slightly above 308 K in this case but values above 335 K are reached at a high current density above 500 mA/cm^2. The arrows in Fig. 3.12 indicate the conductive heat flux through the cell. In planar self-breathing fuel cells, heat is generated mainly by the electrochemical reaction and resistive heating. The phase transition of water is of subordinate influence. The overall reaction in the PEMFC, that is $2\,H_2 + O_2 \rightleftharpoons 2\,H_2O$, is known to be exothermic. The analysis of Lampinem and Fomino [49] shows that there is a difference in the heat distribution among the electrodes. At the anode, the reaction is $H_2 \rightleftharpoons 2\,H^+ + 2e^-$ with a molar reaction entropy of $\triangle S_a = 0.104$ J/(K mol). The hydrogen electrode tends to cool since the reaction is endothermic. However, this effect is negligible compared to the situation at the cathode. The cathodic reaction is $O_2 + 4\,H^+ + 4\,e^- \rightleftharpoons 2\,H_2O$. The molar reaction entropy of the exothermic reaction is $\triangle S_c = -326.36$ J/(K mol). The heat generation rate in the different parts of the fuel cell is shown in Fig. 3.13. Since the charge generation rate in the cathode catalyst layer is highest close to the membrane, the maximum value of the heat generation rate occurs close to the interface between the cathode catalyst layer and the membrane. Resistive heating is important in the polymer phase of the membrane and the catalyst layers. At a relative humidity of 0.2, the conductivity of the membrane is one order of magnitude smaller than at a relative humidity of 0.5. Since the resistive heat generation depends quadratically on the gradient of ϕ_p, this effect dominates at high temperature and low relative humidity. The heat of the reaction depends only linearly on the temperature.

The volumetric source terms of the charge balance equations, i.e. the charge generation rates at the cathode (Eq. (3.9)) and the anode (Eq. (3.13)), are coupled with the potential distributions of ϕ_e and ϕ_p, the local concentrations of oxygen and hydrogen and the temperature distribution. Fig. 3.15 shows the charge generation rate in the catalyst layers of the fuel cell. The distribution of the charge generation is clearly governed by the potential distribution. The proton transport limitation confines the electrochemical reactions to the regions close to the membrane. The steep gradient on the anode side is due to the fast kinetics of the hydrogen oxidation reaction. The geometry of the cell is reflected in the two maxima at the cathode and the anode. If the fuel cell is operated at low cell voltage, the design

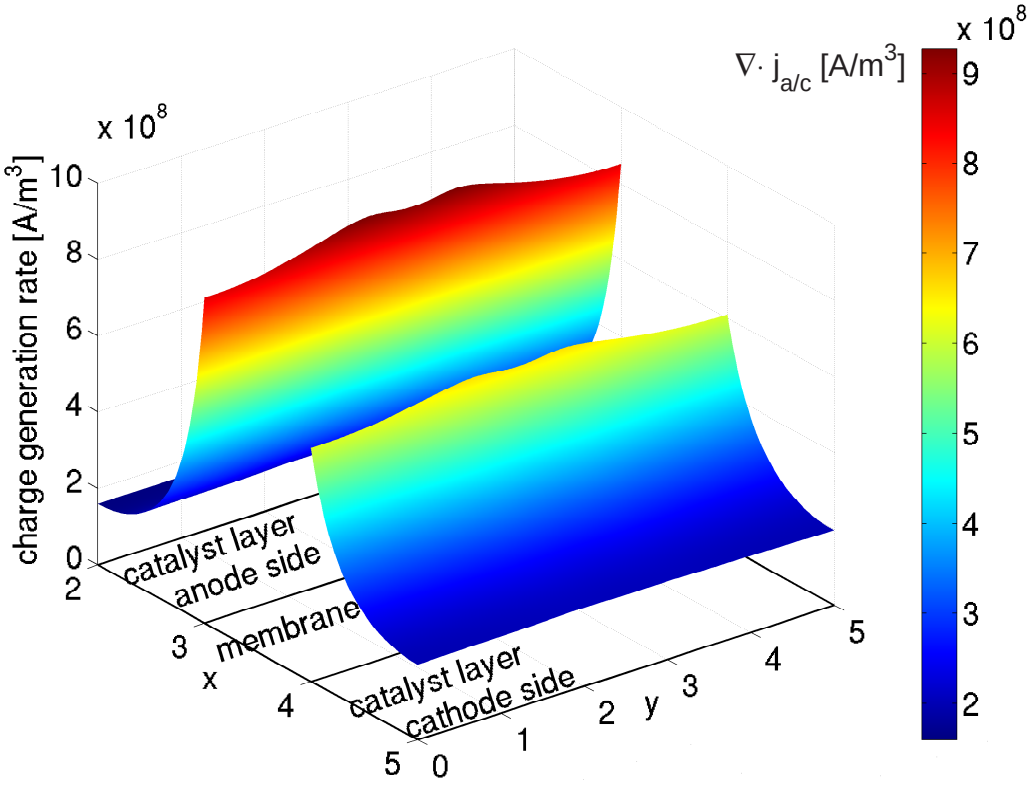

Figure 3.15: Charge generation rate in the catalyst layers of the fuel cell. The divergence of the ionic current density is highest close to the membrane. In the catalyst layer of the anode side, the reaction occurs in a thin layer that is adjacent to the membrane. The only limiting process is the proton transport, which is best close to the membrane. Depletion of hydrogen has no impact. On the cathode side, the shape of the charge generation distribution is the same as at the anode. However, the reaction rate of the oxygen reduction reaction is lower. Thus the reaction is distributed more homogeneously across the catalyst layer. The peaks reflect the influence of the rib on the activity of the catalyst layers. Normalized co-ordinates according to Fig. 3.1 are used.

of the open cathode influences the behavior of the cell more strongly. Fig. 3.16 shows the potential distribution of ϕ_e at a cell voltage of 0.1 V. The potential rises by 50% between the ribs. Thus the region below the rib should be most favored for a high activity of the catalyst layer. However, the rib also causes a drop in the oxygen concentration to 20% of the maximum value at the surface of the cathode. The distribution of the molar fraction of oxygen is shown in Fig. 3.17. Due to the slow kinetics of the oxygen reduction reaction, the behavior of the cathode is critical to the performance of the whole cell. Both the electrolyte and the solid phase potentials increase towards the membrane in the catalyst layer of the cathode. At each point, the driving force for the oxygen reduction reaction is the overpotential $\phi_e - \phi_p - \triangle\phi_{c,eq}$. Thus the lower the local potential $\phi_e - \phi_p$, the larger the charge generation rate. If the transport of protons and oxygen is fast, the cathode behaves like a flat electrode. If one transport mechanism is slow, either $\phi_e - \phi_p$ or x_{O2} becomes non-uniform in the catalyst layer. In Fig. 3.18, a cross-section along the x-direction at $y = 3$ is shown. The shape of the current generation rate shows that the performance of the porous electrode is limited by slow proton transport even at a very low cell voltage. The large opening ratio of the cell ensures sufficient oxygen supply in both cases.

The cross-section along the y-direction at the interface between the catalyst layer of the cathode and the membrane is shown in Fig. 3.19. This in-plane cross-section is interesting since it shows the impact of the cathode design. The graph shows the normalized charge generation rate in order to display clearly the deviation from the average value. The absolute value is mainly determined by the proton transport through the membrane. The shape of the curves shows the competing effects of lateral mass transfer limitation and lateral charge transfer limitation. The region between two ribs performs below average due to the rise of the potentials ϕ_e and ϕ_p. Below the rib, the performance is limited by the drop of the oxygen concentration. The oxygen transport limitation increases strongly with increasing current density. The easiest way to change the behavior of the fuel cell is to change the geometry of the open cathode. In Fig. 3.20, the base case with an opening ratio of 80% is compared to a cathode with an opening ratio of 50%. The results show that the wider rib removes the charge transfer limitation but increases the mass transfer limitation. The properties of the gas diffusion layer provide another possibility to optimize the performance of the fuel cell. An increase of the lateral conductivity, i.e. the conductivity of the gas diffusion layer in the y-direction, reduces the charge transfer limitation. The mass transfer limitation below the ribs can be reduced by a higher effective diffusivity along the y-direction.

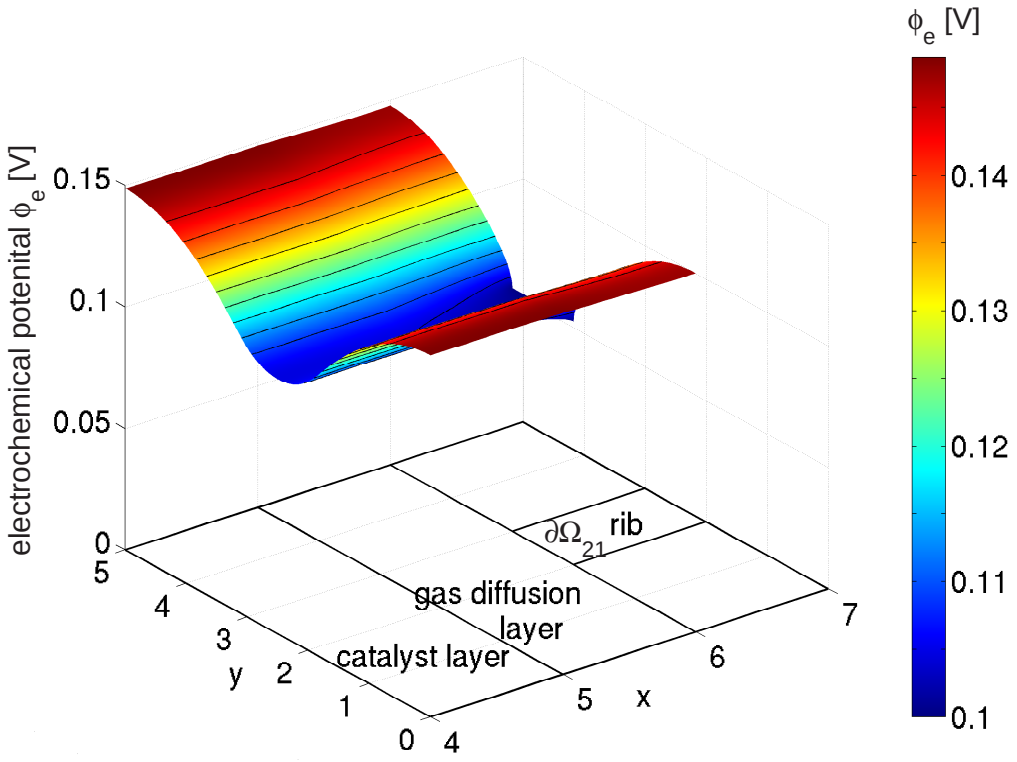

Figure 3.16: Distribution of the electrochemical potential in the carbon phase ϕ_e at a cell voltage of 0.1 V. The rise of ϕ_e between the ribs increases at low cell voltage. The lateral charge transfer limitation in the y-direction is not removed at low cell potential. Normalized co-ordinates according to Fig. 3.1 are used.

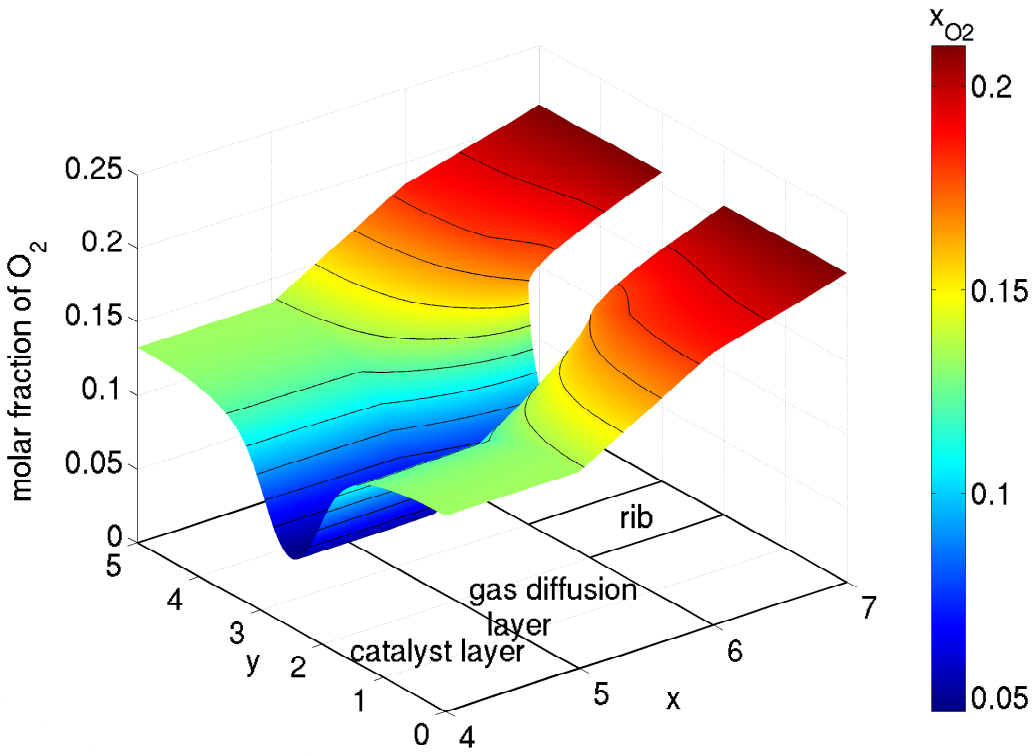

Figure 3.17: Spatial distribution of the molar fraction of oxygen in the porous cathode of the fuel cell at a cell voltage of 0.1 V. The effective mass transport resistance caused by the cathode design is large if the cell is operated at high current density. Normalized co-ordinates according to Fig. 3.1 are used.

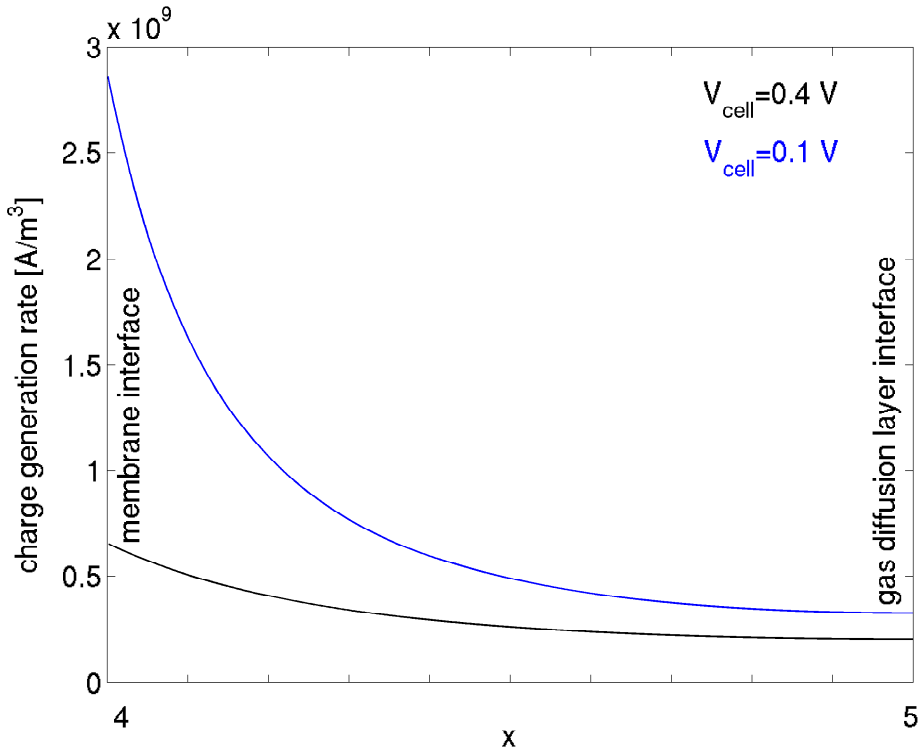

Figure 3.18: Cross-section through the catalyst layer of the cathode in the x-direction. The charge generation rate increases towards the membrane. This indicates the limitation of the oxygen reduction reaction by proton transport through the polymer phase. The divergence of the ionic current density does not increase towards the gas diffusion layer. Thus the through-plane oxygen transport along the x-direction is not performance-limiting compared to the proton transport. Normalized co-ordinates according to Fig. 3.1 are used.

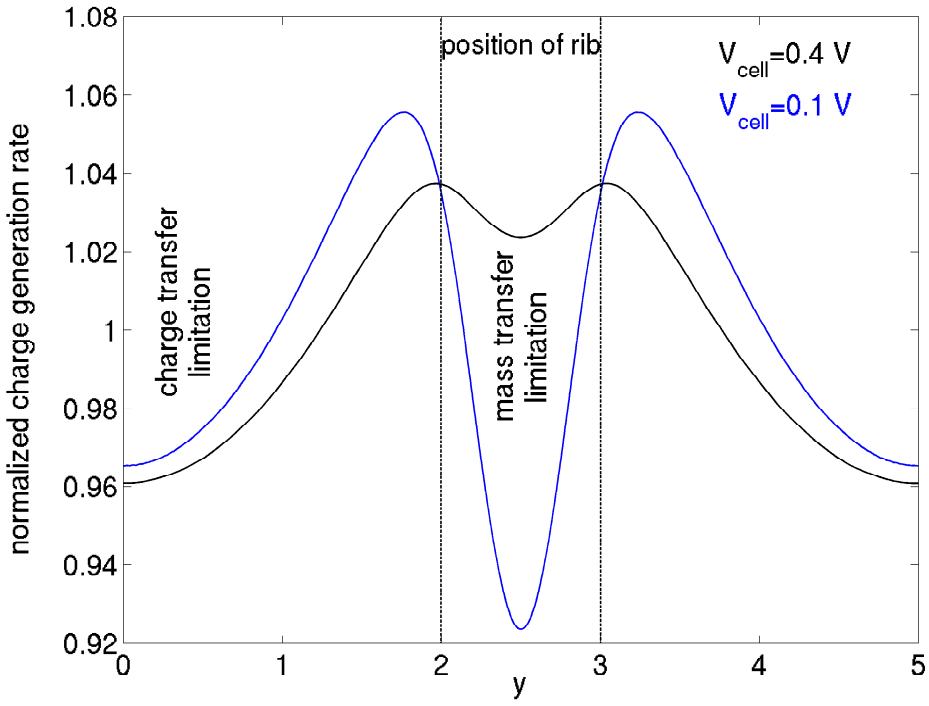

Figure 3.19: Cross-section along the interface between the catalyst layer of the cathode and the membrane. The normalized charge generation rate is shown. The shape of the curves indicates the competing effects of lateral mass transfer and charge transfer resistance in the y-direction that are influenced by the properties of the cathode. Normalized co-ordinates according to Fig. 3.1 are used.

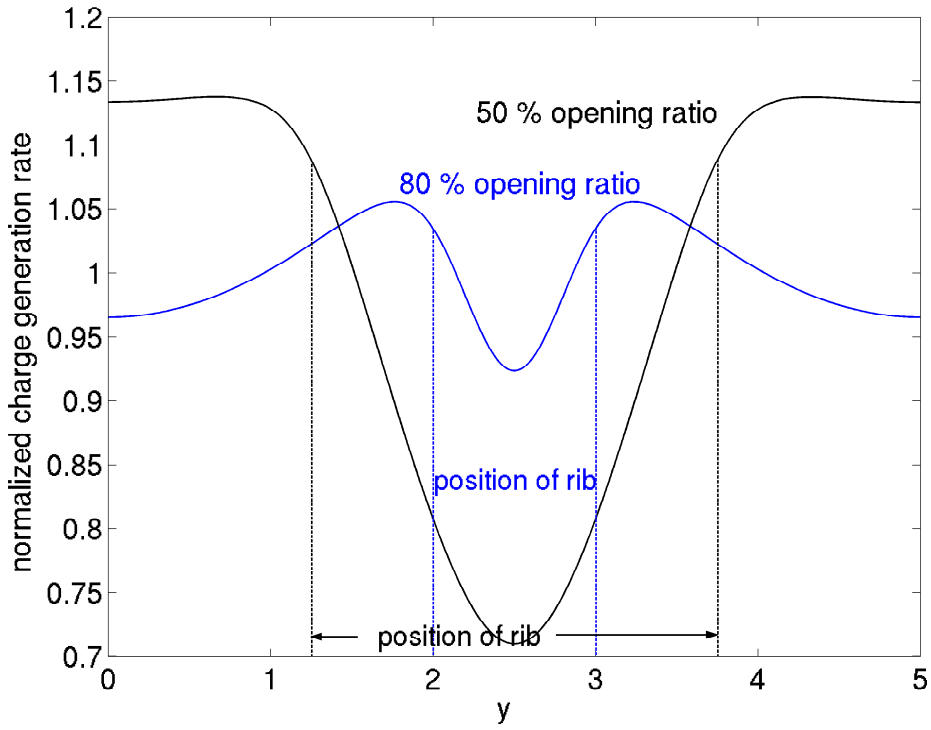

Figure 3.20: Cross-section along the interface between the catalyst layer of the cathode and the membrane at $x = 4$. The figure shows a comparison of two opening ratios at a cell voltage of 0.1 V. If the rib covers 20% of the cathode, the lateral mass transfer and charge transfer are limited in different regions. The wide rib removes the charge transfer limitation but increases the mass transfer resistance. Normalized co-ordinates according to Fig. 3.1 are used.

3.8 Summary of results

A novel non-isothermal two-dimensional model of a planar and self-breathing fuel cell has been presented in this chapter. Migration of electrons and protons, multicomponent diffusion of the gaseous species according to Maxwell-Stefan, and diffusion and electro-osmotic drag of water across the membrane is considered. The protonic conductivity of the membrane is included as a function of temperature and membrane water content. An agglomerate model is derived to take the microstructure of the electrodes into account. The heat transfer equation is solved including the effects of resistive heating, reaction entropy, and heat losses to the surroundings. The model is validated by comparison of simulation results with experimental values. The reference cell used for the validation is a planar self-breathing fuel cell in PCB technology. Excellent agreement between the model predictions and the measured current-voltage relation is achieved.

In general, the performance of the cell is determined by the competing effects of charge transfer and mass transfer. Most important is the conductivity of the membrane and the polymer phase of the cathode catalyst layer. In present fuel cells, this conductivity decreases rapidly if the relative humidity in the porous electrodes decreases. This effect limits the rate of the electrochemical reactions, particularly on the cathode side, and leads to non-uniform current production within the catalyst layer. A higher protonic conductivity already at moderate relative humidity would increase the performance substantially. To date, the protonic conductivity is highest when the polymer is in contact with liquid water. However, liquid water increases the mass transfer resistance and can lead to flooding and deactivation of the catalyst layer.

The design of the cathode influences the performance of the cell in several ways. The ribs in the cathode end-plate affect the potential distribution, resulting in a charge generation rate which is highest close to the ribs. The oxygen concentration is lowest under the middle of the ribs, reducing the charge generation rate in this region of the catalyst layer. Both, access to the oxygen supply and access to the electron supply is important for efficient use of the catalyst layers. The fuel cell design studied in the base case leads to a charge generation rate that is best close to the edges of the ribs in the cathode end-plate. The rib is an obstacle for the diffusive outflux of the product water. Liquid water is most likely to be formed first under the rib.

In the cathode, the supply of the active regions between the ribs with electrons causes a strong non-uniformity in the current density distribution. Close to the ribs in the gas diffusion layer, the current density is an order of magnitude higher than the average current density of the cell. This causes increased resistive heating in that part of the fuel cell. The temperature distribution of the planar self-breathing fuel cell is governed by two effects. The main source of heat is located

in the active area of the cathode, leading to an increased temperature in the center of the cell sandwich. The ribs in the cathode act like cooling fins that remove the heat from the center of the cell. This results in a temperature that is lower underneath the ribs than in the areas between the ribs. The overall temperature difference in this type of cell is small, only about 1 K at an average current density of about 300 mA/cm^2. This is a result of the high surface-to-volume ratio, which causes efficient heat removal mainly by convection from the fuel cell to the surroundings. However, a higher power density can be reached using the concept of planar fuel cells. With increasing power density, resistive heating and the heat generated by the electrochemical reaction will limit the cell performance. At low current density, the mass transfer limitation is small and the use of wide ribs and thin gas diffusion layers is preferable. In the high current density regime, the ribs should be thin to reduce the mass transfer limitation. The lateral mass transfer resistance can be reduced further by a high effective lateral diffusivity of the gas diffusion layer. However, the lateral conductivity of the gas diffusion layer should be excellent to avoid significant charge transfer limitations between the ribs.

Chapter 4

Two Phase Dynamic Modeling of the PEMFC

In sections 4.2 to 4.6 a mathematical model is developed that is based on a coupled system of partial differential equations. The model contains a dynamic, two-phase description of the proton exchange membrane fuel cell and a membrane model that accounts for Schroeder's paradox. The mass transport in the gas phase and in the liquid phase is considered as well as the phase transition between liquid water and water vapor. The transport of charges and the electrochemical reactions are part of the model.
In section 4.7 a potential sweep experiment is simulated using the mathematical model. The cell voltage is varied periodically between 0.9 V and 0.1 V The resulting cyclic voltammograms are suitable for exciting the liquid transport and accumulation in the PEMFC. The cyclic voltammograms are measured using a test fuel cell with a commercial MEA and an active area of 1 cm^2. The small active area ensures homogeneous operating conditions and reduces the lateral inhomogeneity that is not captured within the context of a one-dimensional model. In this way, the dynamic effect of liquid water formation and transport on the current-voltage characteristic of the fuel cell is investigated. A hysteresis effect is found in the measured time-dependent current-voltage relation. The limiting current density is time-dependent. Qualitative agreement of simulated and measured results is achieved. An analysis of the observed hysteresis of the current-voltage characteristics, based on the modeling results, is given in section 4.8.

4.1 Literature review of dynamic two-phase modeling

Excellent stability of fuel cell operation and minimization of the fuel cell system volume are usually required in portable applications. These constraints are accompanied by operating conditions that change over time. System start-up, system shut-down, and changes in the power demand of the electronic load during operation require an excellent understanding of the transient behavior of fuel cells. In particular, the dynamic accumulation and transport of liquid water in the PEMFC is important in this context. Two-phase, dynamic fuel cell models provide insight into the physical phenomena that govern the dynamic operating behavior of a PEMFC.

An extensive literature review of mathematical fuel cell models is given in section 3.1. However, most of the models published so far either disregard the formation of liquid water or treat the phase transition in a simplified way without solving a transport equation for liquid water.

Recently, a number of two-phase models for the PEMFC have been published. Wang [50] presented a two-phase flow mixture model of the cathode side of a PEMFC that is able to predict the liquid water saturation in the cathode. The membrane and the catalyst layer are included via boundary conditions in the model. A similar two-phase flow mixture model of the cathode of the PEMFC was presented by You and Liu [51]. Again, the catalyst layer and the membrane are included as boundary conditions. More recently Siegel and Ellis [52] presented a two-dimensional model accounting for the transport of liquid water in the porous electrodes. The membrane is described using a simple diffusive approach. The so-called Schroeder's paradox is neglected. Berning and Djilali [53] presented a three-dimensional, two-phase, multicomponent model of the cathode and anode of a PEMFC. Pasaogullari [54] investigated the effect of flooding on the cell performance. In particular, they studied the influence of the wettability of the gas diffusion layer on the liquid water transport. Finally, Weber and Newman [55] published a pseudo-two-dimensional fuel cell model including the transport of liquid water. Water transport across the polymer membrane is approached in a novel way that treats gradients in the liquid pressure and the chemical potential as separate driving forces.

However, all of the models mentioned in the preceding paragraph are steady-state models that ignore any transient effect in fuel cell operation. The dynamic fuel cell models published so far usually simplify the mathematical description significantly by making various assumptions. For example, Amphlett et al. [21] developed a transient model of a PEMFC stack. The model predicts the time dependence of the fuel cell performance and the heat losses. The liquid water

transport in the cells is not accounted for. A dynamic PEMFC model was presented by Woehr and Bolwin [46]. Energy and mass transfer is considered but the formation of liquid water is neglected. Water transport in the membrane is described using a simple diffusion approach. Another simplified dynamic model of a PEMFC is presented in [56]. A two-dimensional dynamic model of a PEMFC that accounts for liquid water transport was outlined in [57]. A comprehensive membrane model and a comparison of the simulation with experimental results is not given in that publication.
In contrast to the mathematical models that have been published so far, this chapter presents a PEMFC model that accounts for both the dynamic of the fuel cell and for the two-phase flow of water. Furthermore, a new time-dependent description of the membrane is proposed. An important feature is the coupling of the two-phase flow equations with the electrochemical potential and the liquid pressure of water in the membrane. The membrane model is an extension of the steady-state description given in [58]. The model accounts for the different transport processes of water across the membrane. The structural change in the membrane with changing membrane humidity is considered. A test cell is used to measure the time-dependent current voltage characteristics. Cyclic voltammograms using potential sweep rates of 10 mV/s and 5 mV/s and a cell voltage range of 0.1 V to 0.9 V are presented and discussed. This type of cyclic voltammogram is appropriate for exciting the liquid water formation and transport in the PEMFC.

4.2 Model concept

The PEMFC model presented here is a one-dimensional, two-phase, dynamic model of a cell sandwich including the gas diffusion layers, the catalyst layers, and the membrane. A detailed description of the following transport phenomena is provided:

- conduction of electrons through the carbon support of the catalyst layers and the gas diffusion layers
- migration of protons through the polymer phase of the catalyst layers and the membrane
- diffusion of oxygen and water vapor through the gas diffusion layer and the catalyst layer of the cathode
- diffusion of hydrogen and water vapor through the gas diffusion layer and the catalyst layer of the anode

- transport of water through the membrane driven by gradients in the relative humidity and liquid pressure
- electro-osmotic drag of water through the membrane
- transport of liquid water through the gas diffusion layers and the catalyst layers of anode and cathode.

The electrochemical reactions are described using the Butler-Volmer equation. Furthermore, the reduction of the effective active area in the catalyst layers due to flooding by liquid water is considered. The various couplings between the transport processes are part of the mathematical model. An effective medium approach is used for the gas diffusion layers, the catalyst layers, and the membrane. Since the model is one-dimensional, the influence of the gas channels is considered by means of boundary conditions.

Model assumptions

The most important model assumptions are as follows:

- The model is isothermal.
- The gas pressure in the gas diffusion layers is assumed to be constant.
- Multicomponent diffusion is not considered. A Fick diffusion approach is used.
- The product water is assumed to be generated in the gas phase.
- The influence of gravity on the transport of liquid water is neglected.
- Electrical contact losses at the interfaces between different components of the cell are not part of the model.

4.3 Experimental setup and model domain

The computational domain used for the simulations is shown in Fig. 4.1. The domain represents a cross-section through a PEMFC. The cross-section is perpendicular to the membrane. The computational domain is divided into different subdomains Ω_i that describe the gas diffusion layers $\Omega_{1/5}$, the catalyst layers $\Omega_{2/4}$, and the membrane Ω_3. The subdomains are coupled with each other via appropriate boundary conditions at the boundaries denoted by $\partial\Omega_i$. In order to improve

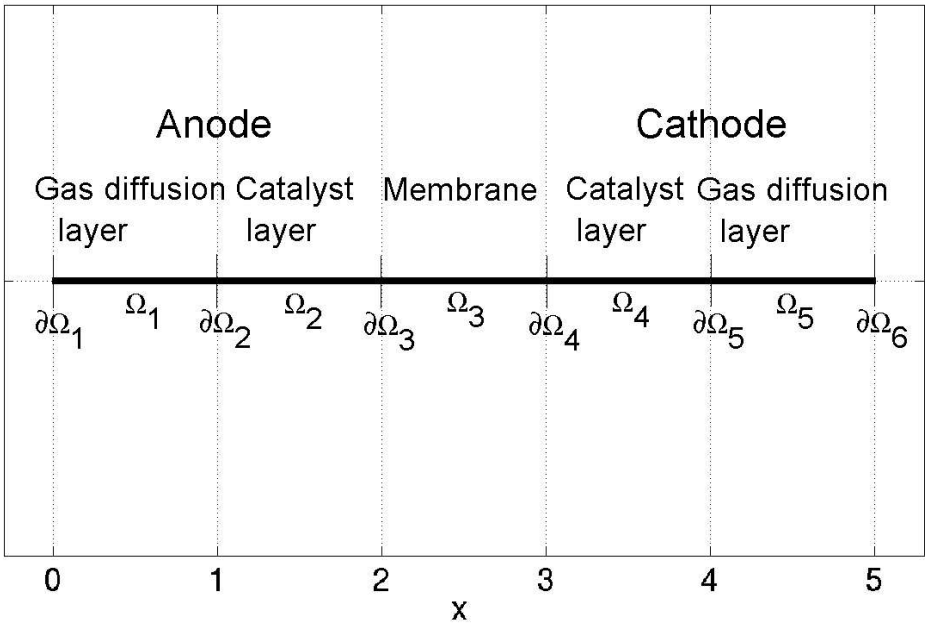

Figure 4.1: The geometry of the computational domain is shown using normalized coordinates. Subdomains are labelled as Ω_i and boundaries are labelled as $\partial\Omega_i$. The model equations are scaled. This results in subdomains of equal thickness. The computational domain that is perpendicular to the membrane corresponds to a physical domain that is 645 μm thick.

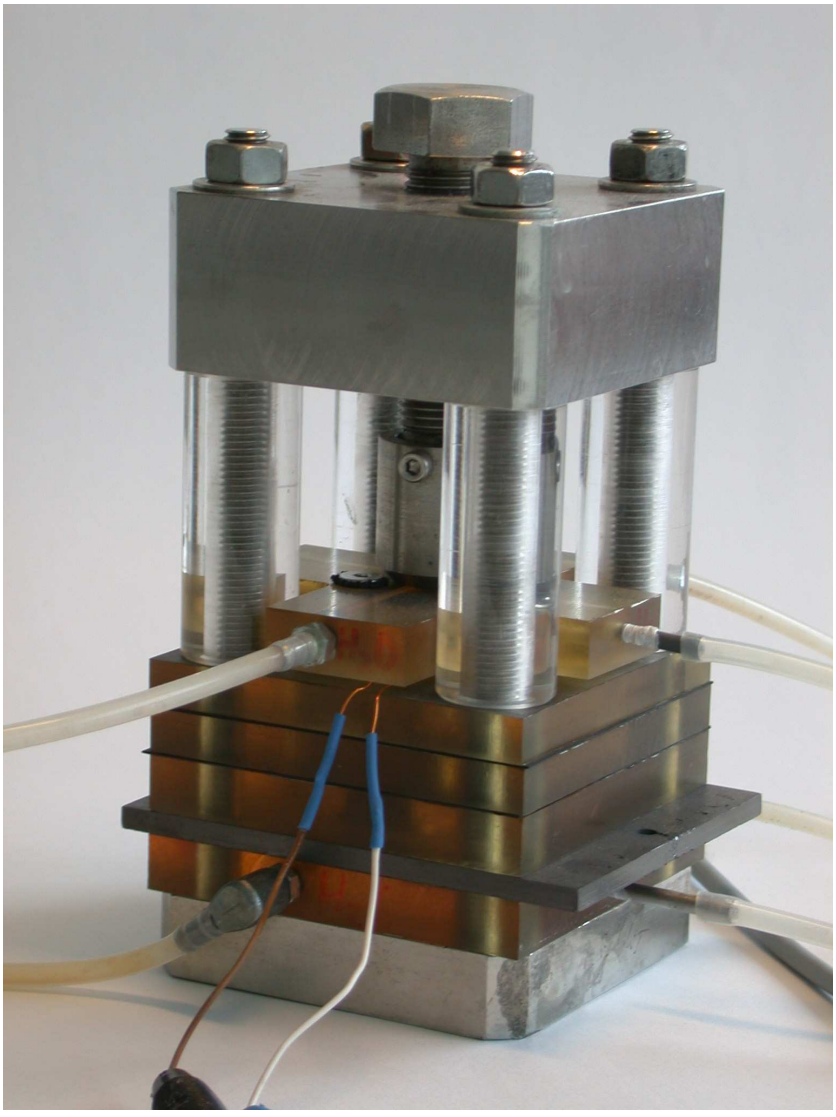

Figure 4.2: Small test fuel cell for validation measurements. The active area is only 1 cm^2 to reduce lateral gradients of the reactant distribution and the humidity. Moreover, the cell is water-cooled and maintains a well-defined contact pressure during the measurements. Courtesy of Dietmar Gerteisen, Fraunhofer Institute for Solar Energy Systems

the computational efficiency, the equations have been scaled. Equally thick subdomains resulting in a very simple geometry are obtained. The scaling improves the numerical stability of the model. The domain depicted in Fig. 4.1 corresponds to a physical domain that includes a cross-section through the gas diffusion layers of the cathode side and the anode side and the membrane electrode assembly. The thickness of the gas diffusion layers is 300 μm. The MEA has a polymer thickness of 25 μm. The catalyst layers are 10 μm in thickness each.
Measurement data are used for the validation of the mathematical model. The measurement data are taken using a small test fuel cell as shown in Fig. 4.2. Meander-shaped flow-fields, machined in graphite plates, are used on both the cathode side and the anode side of the fuel cell. Commercial TORAY^{TM} TGP-H-060 gas diffusion layers and a PRIMEA^{TM} 5510 MEA made by GORE^{TM} are used. The cell is connected to a Solartron^{TM} 1286 electrochemical interface and a 1255 HF frequency response analyzer in order to measure the cell voltage, the current, and the resistance of the cell. The gas flows are regulated using gas flow controllers. The gases that are fed into the fuel cell are passed through humidifiers made of stainless steel. The temperature inside the humidifiers is controlled by the test software. The fuel cell test software is programmed based on LabView^{TM}. All parameters that are important during the course of the measurement, i.e. cell voltage, current density, gas flows, and cell temperature are controlled by the software. The fuel cell is water cooled. Cooling channels are machined into the flow field plates of the cathode side. A Fisherbrand^{TM} FBC 720 thermostat is connected to the cooling channels. The test cell was held at a constant temperature during the measurements. The active area of the cell is only 1 cm^2. The small active area of the test cell enables a homogeneous gas supply and a uniform cell temperature.

4.4 Time-dependent model equations

4.4.1 Electrochemical reactions

The electrochemical reactions in the catalyst layers are modeled by the Butler-Volmer equation (Eq. (2.10)). In order to account for the porous structure of the electrodes, the active surface area per unit volume of catalyst a is introduced. The divergence of the ionic current density in the catalyst layers is given by

$$\nabla \cdot \vec{j}_c = s_g \; a \; i_c \left(\frac{x_{O_2}}{x_{O_2}^{ref}} \right) \left[exp\left(\frac{(1-\alpha_c) z_c F}{R\,T} \, \eta_c \right) - exp\left(-\frac{\alpha_c z_c F}{R\,T} \, \eta_c \right) \right] = Q_{c,C} \tag{4.1}$$

where i_c is the exchange current density of the oxygen reduction reaction, and α_c and z_c are the symmetry factor and the number of electrons transferred in the rate-determining step, respectively. The normalized oxygen concentration at reference conditions is denoted as $x_{O_2}^{ref}$. The overvoltage at the cathode is given by $\eta_c = (\phi_e - \phi_p - \Delta\phi_{c,eq})$, where $\Delta\phi_{c,eq}$ is the difference between electron and proton potential at reference equilibrium conditions. The factor s_g represents the gas saturation. Gas and liquid saturation are linked via $s_g = 1 - s_l$. A similar equation is used for the description of the anode

$$\nabla \cdot \vec{j}_a = s_g \, a \, i_a \left(\frac{x_{H_2}}{x_{H_2}^{ref}} \right) \left[exp\left(\frac{(1-\alpha_a) z_a F}{R\,T} \, \eta_a \right) - exp\left(-\frac{\alpha_a z_a F}{R\,T} \, \eta_a \right) \right] = Q_{a,C} \tag{4.2}$$

The overvoltage at the anode is given by $\eta_a = (\phi_e - \phi_p)$, where the equilibrium potential difference of the electron and the proton potential at the anode is assumed to be zero.

4.4.2 Charge transport

The electron and proton potentials are calculated using the Poisson equation (Eq. (2.39)). Accordingly, the following equation is defined in the gas diffusion layers and the catalyst layers

$$\nabla \cdot [-\sigma_{e,\kappa} \nabla \phi_e] = Q_{e,C} \; in \; \Omega_\kappa, \; \kappa = 1,2,4,5. \tag{4.3}$$

The potential of the carbon phase is ϕ_e. $\sigma_{e,\kappa}$ denotes the electronic conductivity of subdomain κ. The source term of the charge balance is defined as

$$Q_{e,C} = \begin{cases} -Q_{a,C} & in \; \Omega_2 \\ -Q_{c,C} & in \; \Omega_4 \\ 0 & elsewhere. \end{cases} \tag{4.4}$$

The stationary solution of the problem serves as an excellent initial estimate for the time-dependent problem. The steady-state solution is obtained using the following boundary conditions

$$\phi_e = \begin{cases} 0 & at \; \partial\Omega_1 \\ V_{cell} & at \; \partial\Omega_6 \end{cases} \tag{4.5}$$

and

$$[-\sigma_{e,\kappa} \nabla \phi_e] \cdot \vec{n} = 0 \tag{4.6}$$

at $\partial\Omega_3$ and $\partial\Omega_4$. $\vec{n}$ represents the outward-pointing normal vector for each boundary. At the cathode and anode sides, the continuity of the current and the electron potential holds at the interface between the gas diffusion layer and catalyst layer.

A time-dependent problem can be described by modification of Eq. (4.5) at boundary $\partial\Omega_6$. In this case, the constant cell voltage V_{cell} is replaced by a function that describes the time dependence of the cell voltage. A similar equation for the proton transport is used in the membrane and the catalyst layers

$$\nabla \cdot [-\sigma_{p,\kappa} \nabla \phi_p] = Q_{p,C} \; in \; \Omega_\kappa, \; \kappa = 2,3,4. \tag{4.7}$$

Again, ϕ_p and $\sigma_{p,\kappa}$ denote the potential and the conductivity of the proton-conducting phase in subdomain κ, respectively. The source terms are defined as

$$Q_{p,C} = \begin{cases} Q_{a,C} & in \; \Omega_2 \\ Q_{c,C} & in \; \Omega_4 \\ 0 & elsewhere. \end{cases} \tag{4.8}$$

In [58] the protonic conductivity of the acid form of Nafion is given as a function of the water content. Hence, the protonic conductivity of the membrane Ω_3 is expressed as

$$\sigma_{3,p} = \begin{cases} 50 \; (f - 0.06)^{1.5} \; exp\left[\frac{15000}{R}\left(\frac{1}{T_{ref}} - \frac{1}{T}\right)\right] & f \leq 0.45 \\ 50 \; (0.39)^{1.5} \; exp\left[\frac{15000}{R}\left(\frac{1}{T_{ref}} - \frac{1}{T}\right)\right] & f > 0.45. \end{cases} \tag{4.9}$$

f denotes the volume fraction of water in the membrane and is given by

$$f = \frac{\lambda \, V_{H_2O}}{V_m + \lambda \, V_{H_2O}} \, . \tag{4.10}$$

λ is the number of water molecules per sulfonic acid group in the membrane. V_{H_2O} is the molar volume of water that is given by

$$V_{H_2O} = \frac{M_{H_2O}}{\rho_l} \, , \tag{4.11}$$

where ρ_l is the density of water at operating temperature. M_{H_2O} denotes the molar mass of water. V_m is the partial molar volume of the dry membrane given by the quotient of the equivalent weight and the dry density of the membrane

$$V_m = \frac{EW}{\rho_m} \, . \tag{4.12}$$

In contrast to the membrane, the catalyst layer is not made of pure ionomer. Hence, the protonic conductivity inside the catalyst layer is expected to be lower than inside the membrane. The protonic conductivity of the catalyst layer is

expressed as the product of the protonic conductivity of Nafion and the Nafion content of the catalyst layers $\sigma_{p,2/4} = \nu \cdot \sigma_{p,3}$. ν denotes the volume fraction of ionomer in the catalyst layers. The boundary conditions for the ionic current balance are

$$[-\sigma_{p,\kappa} \nabla \phi_p] \cdot \vec{n} = 0 \tag{4.13}$$

at the boundaries $\partial\Omega_2$ and $\partial\Omega_5$. The continuity of the protonic current and potential holds at the interfaces between the membrane and the catalyst layers.

4.4.3 Two-phase mass transport

Two-phase flow formulation

From the balance between the volume saturation of liquid water s_l and gas s_g, the following equations are obtained to describe the two-phase flow in the porous media (see Eq. (2.41) in section 2.5)

$$\partial_t [\pi_\kappa \rho_k s_k] + \nabla \cdot [\rho_k \vec{v_k}] = Q_{k,M}, \;\; k = l, g \; . \tag{4.14}$$

π_κ denotes the in-situ porosity of subdomain κ, where $\kappa = 1,2,4,5$. s_k is the saturation of phase k, where $k = l, g$ describes the liquid and gas phases, respectively. ρ_k denotes the density of phase k. The divergence of the mass flux is described using Darcy's law

$$\vec{v_k} = -K_\kappa \frac{k_k}{\mu_k} \nabla p_k, \;\; k = l, g \; , \; \kappa = 1,2,4,5 \; . \tag{4.15}$$

The permeability of the different subdomains is denoted as K_κ and the relative permeability of phase k is denoted as k_k. μ_k denotes the viscosity of phase k. Combining Eq. (4.14) and Eq. (4.15) yields the multiphase flow differential equations (Eq. (2.45)) that are derived in section 2.5. The relative permeabilities of the liquid and gas phases are represented by [59]

$$k_l = (s_l)^m \tag{4.16}$$

$$k_g = (1 - s_l)^m, \tag{4.17}$$

where $m = 3$ is used. The difference between the pressure of the gas phase and the liquid phase is the capillary pressure

$$p_c = p_g - p_l. \tag{4.18}$$

In a hydrophobic medium, the liquid pressure p_l is higher than the gas pressure p_g. Hence the capillary pressure defined by Eq. (4.18) is negative. In a hydrophilic

medium, $p_l < p_g$ holds, resulting in a positive capillary pressure. An analytical determination of the relation between capillary pressure and saturation for porous media does not exist because of the irregular pore geometry. Numerous scientists have derived a functional relationship between the capillary pressure and the saturation. However, so far the relationship between the capillary pressure and the water saturation has not been determined to describe the porous media that are commonly used in PEMFC's. Most often the models of Leverett [60], Brooks and Corey [61], and Van Genuchten [62] are used for air-water systems. The capillary pressure is expressed as proposed in [54]

$$p_c = \sigma_{H_2O} \cos\theta_\kappa \sqrt{\left(\frac{\pi_\kappa}{K_\kappa}\right)}\, J(s_l)\ , \tag{4.19}$$

where $J(s_l)$ is the Leverett function

$$J(s_l) = \begin{cases} 1.417(1-s_l) - 2.120(1-s_l)^2 + 1.263(1-s_l)^3 & if\ \theta < \frac{\pi}{2} \\ 1.417\ s_l - 2.120\ s_l^2 + 1.263\ s_l^3 & if\ \theta > \frac{\pi}{2}\,. \end{cases} \tag{4.20}$$

Note that the Leverett function is expressed in terms of the phase saturation of the non-wetting phase in each case. The contact angle of subdomain κ is denoted as θ_κ. The surface tension of water is described by the following interpolation equation [63]

$$\sigma_{H_2O} = B\,\tau^\nu\,(1 + b\,\tau)\ , \tag{4.21}$$

where $\tau = 1 - T/T_c$, $T_c = 647.096$ K, $B = 235.8$ mN/m, $b = -0.625$, and $\nu = 1.256$. This equation is valid between the triple point and the reference temperature T_c. Using the constraint $s_l + s_g = 1$, only one equation of the form of Eq. (4.14) remains. Hence, we solve for the liquid water saturation. The source term of the liquid phase is described according to [64]

$$\begin{aligned} Q_{l,M} = {} & k_c\,\pi_\kappa\,s_g\,\frac{M_{H2O}}{RT}\,(p_{H_2O} - P_{sat})\,H\,[p_{H_2O} - P_{sat}] \\ & + k_v\,\pi_\kappa\,s_l\,\rho_l\,(p_{H_2O} - P_{sat})\,H\,[P_{sat} - p_{H_2O}] \end{aligned} \tag{4.22}$$

in $\Omega_1, \Omega_2, \Omega_4, \Omega_5$. k_v and k_c denote the evaporation and condensation rate constants, respectively. p_{H_2O} denotes the partial pressure of water vapor and H is the Heaviside step function. The saturation pressure of water P_{sat} is given by $\log P_{sat} = 8.07 - 1656.39/(226.86 + [T - 273.15]) + 2$. At the interfaces between the gas diffusion layers and the gas channels $\partial\Omega_1$ and $\partial\Omega_6$, the average saturation of the GDL is used as a boundary condition

$$s_l = s_l^{avg}. \tag{4.23}$$

In general, the saturation at the interfaces depends on the two-phase flow characteristics of the gas diffusion layer and the gas channel. As the lower bound of s_l^{avg} the immobile saturation, i.e. the smallest saturation necessary for continuous liquid saturation, is used. The immobile saturation in the case of spherical packings is experimentally investigated in [65]. The results show little influence of the physical properties of the matrix on the immobile saturation. Spatial heterogeneity leads to a significant increase in the immobile saturation. The gas diffusion layers commonly used in fuel cells are very homogeneous. Considering this, we assume an immobile saturation of the diffusion medium of $s_l^{im} = 0.1$ [66]. At the interfaces between the catalyst layers and the membrane, $\partial\Omega_3$ and $\partial\Omega_4$, the continuity of the liquid pressure and the liquid water flux holds. Continuity of the liquid pressure and the liquid water flux holds also at the interfaces between the catalyst layers and the gas diffusion layers, $\partial\Omega_2$ and $\partial\Omega_5$.

Gas transport at the cathode

The cathode side of the fuel cell model consists of the subdomains Ω_4 and Ω_5. The mass balance of the gaseous species on the cathode side is described by a time-dependent continuity equation for each species. The diffusive mass flux of species i, where $i = O_2, H_2O, N_2$, is described using the Fick diffusion equation (Eq. (2.28)) and the continuity equation (Eq. (2.14))

$$\partial_t \left[\pi_\kappa \rho_c s_g \omega_i\right] - \nabla \cdot \left[\pi_\kappa \left(\frac{\pi_\kappa - 0.11}{1 - 0.11}\right)^{0.785} \rho_c s_g^2 \, D_i \nabla \omega_i\right] = Q_{i,M}. \tag{4.24}$$

π_κ denotes the porosity of subdomain κ, where $\kappa = 4, 5$. ω_i is the mass fraction of species i. s_g is the gas saturation and D_i the Fick diffusivity of species i. ρ_c is the density of the gas on the cathode side given by $\rho_c = M_c P / RT$, where $M_c = \sum_i x_i M_i$, $i = O_2, H_2O, N_2$. M_i denotes the molar mass of species i. For the mass fraction of the species, $\sum_i \omega_i = 1$ holds. The proton conductivity of the membrane, the level of the catalyst flooding, and the effective diffusivity all strongly depend on the water saturation of the GDL. Nam and Kaviany [66] used numerical upscaling to determine the effective diffusivity of the GDL as a function of the saturation and the porosity, i.e. $D_{i,\kappa}^{eff} = D_i f(\pi_\kappa) g(s_g)$. The GDL is modeled as a stack of overlapping fiber screens with square pore spaces. The species conservation equation $\nabla^2 c_i = 0$ is solved for that geometry using the Gauss-Seidel iteration method. This procedure is repeated for different network geometries, porosities, and values of the saturation. Based on the average of the numerical results, the following relations are obtained

$$f(\pi_\kappa) = \pi_\kappa \left(\frac{\pi_\kappa - 0.11}{1 - 0.11}\right)^{0.785} \tag{4.25}$$

$$g(s_g) = s_g^2 \,. \tag{4.26}$$

Oxygen is consumed by the oxygen reduction reaction at the cathode side. The source terms of the oxygen balance are given by

$$Q_{O_2,M} = \begin{cases} \frac{M_{O_2}}{4F} \cdot Q_{c,C} & in\ \Omega_4 \\ 0 & elsewhere. \end{cases} \tag{4.27}$$

The product water of the electrochemical reaction at the cathode is assumed to be generated in the gas phase. Liquid water is formed by condensation on pre-existing liquid surfaces or condensation sites, for example hydrophobic coating defects. The source terms of the water vapor balance account for the phase transition between water vapor and liquid water

$$Q_{H_2O,M} = \begin{cases} -\frac{M_{H_2O}}{2F} \cdot Q_{c,C} - Q_{l,M} & in\ \Omega_4 \\ -Q_{l,M} & in\ \Omega_5 \,. \end{cases} \tag{4.28}$$

At boundary $\partial\Omega_6$ the molar fraction of oxygen and water vapor is given by $x_{O_2} = x_{O_2}^{in}$ and $x_{H_2O} = x_{H_2O}^{in}$, respectively. At the interface between the gas diffusion layer and the catalyst layer $\partial\Omega_5$ the continuity of the concentrations and the diffusive fluxes of oxygen and water vapor holds. The membrane is assumed to be impervious to oxygen. Hence, at interface $\partial\Omega_4$ the following equation applies

$$-\left[\pi_4 \left(\frac{\pi_4 - 0.11}{1 - 0.11}\right)^{0.785} \rho_c s_g^2 D_{O_2} \nabla \omega_{O_2}\right] \cdot \vec{n} = 0 \,. \tag{4.29}$$

Gas transport at the anode

The anode side consists of the subdomains Ω_1 and Ω_2. The gaseous species that are present at the anode are H_2 and H_2O. In analogy to the description of the cathode, a mass balance is set up using the Fick diffusion approach. The time-dependent mass balance on the anode side is given by

$$\partial_t \left[\pi_\kappa \rho_a s_g \omega_i\right] - \nabla \cdot \left[\pi_\kappa \left(\frac{\pi_\kappa - 0.11}{1 - 0.11}\right)^{0.785} \rho_a s_g^2 \, D_i \nabla \omega_i\right] = Q_{i,M}. \tag{4.30}$$

The density of the gas mixture at the anode side is given by $\rho_a = M_a P / RT$, where $M_a = \sum_i x_i M_i \ , \ i = H_2, H_2O$. Hydrogen is consumed by the hydrogen oxidation reaction on the anode side. The only source of water vapor on the anode side is the phase transition of water between the liquid and gas phases. Consequently, the source terms of the hydrogen and water vapor balances are

$$Q_{H_2,M} = \begin{cases} -\frac{M_{H_2}}{2F} \cdot Q_{a,C} & in\ \Omega_2 \\ 0 & in\ \Omega_1. \end{cases} \tag{4.31}$$

and

$$Q_{H_2O,M} = -Q_{l,M} \; in \; \Omega_1, \Omega_2 \, , \tag{4.32}$$

respectively. At boundary $\partial\Omega_1$, the molar fraction of hydrogen and water vapor is given by $x_{H_2} = x_{H_2}^{in}$ and $x_{H_2O} = x_{H_2O}^{in}$, respectively. At the interface between the gas diffusion layer and the catalyst layer $\partial\Omega_2$, the continuity of the concentrations and the diffusive fluxes of hydrogen and water vapor holds. The membrane is assumed to be impervious to hydrogen. Hence at interface $\partial\Omega_3$

$$-\left[\pi_2 \left(\frac{\pi_2 - 0.11}{1 - 0.11}\right)^{0.785} \rho_a s_g^2 D_{H_2} \nabla \omega_{H_2}\right] \cdot \vec{n} = 0 \tag{4.33}$$

holds. Here $\vec{n}$ is the outward-pointing normal vector of this boundary. The boundary condition for the concentration of water in the gas phase at the interface between the catalyst layer and the membrane is explained in the following paragraph.

4.4.4 Dynamic two-phase membrane model

Ignoring the effects of thermal diffusion, the transport of water through the membrane is driven by gradients in water concentration, pressure, and potential. There is no broad consensus in the literature regarding how water is transported through the membrane. The literature is divided among those who claim that the water flux is pressure driven [67] and those who claim it is concentration driven. A minority claims it is both. Recently this argument was resolved by Weber and Newman [68]. They provide a detailed structural model of water transport inside a perfluorinated sulfonic acid ionomer. The model for the first time gives a physical description of the so-called Schroeder's paradox. According to the model, there are two different transport mechanisms. The first mechanism for vapor-equilibrated membranes is proportional to the gradient in the chemical potential. The second mechanism for liquid-equilibrated membranes is proportional to the gradient in hydraulic pressure. Moreover, as the water content of the membrane changes, the membrane itself undergoes a structural change. This change of the membrane structure is schematically shown in Fig. 4.3. Initially, the water is absorbed in the membrane and forms inverted micelles with the hydrophilic acid groups. As the water content increases, the micelles become interconnected by a network of collapsed slightly hydrophobic channels. Additional water causes these channels to expand and fill with liquid water. A continuous transition is assumed between the two transport modes. When the membrane is neither fully liquid nor vapor-equilibrated, the transport mode is assumed to be a superposition of the two. The overall flux of water is distributed between the two modes based on the fraction of expanded channels. According to [58], the overall flux of water N_{H_2O} can be

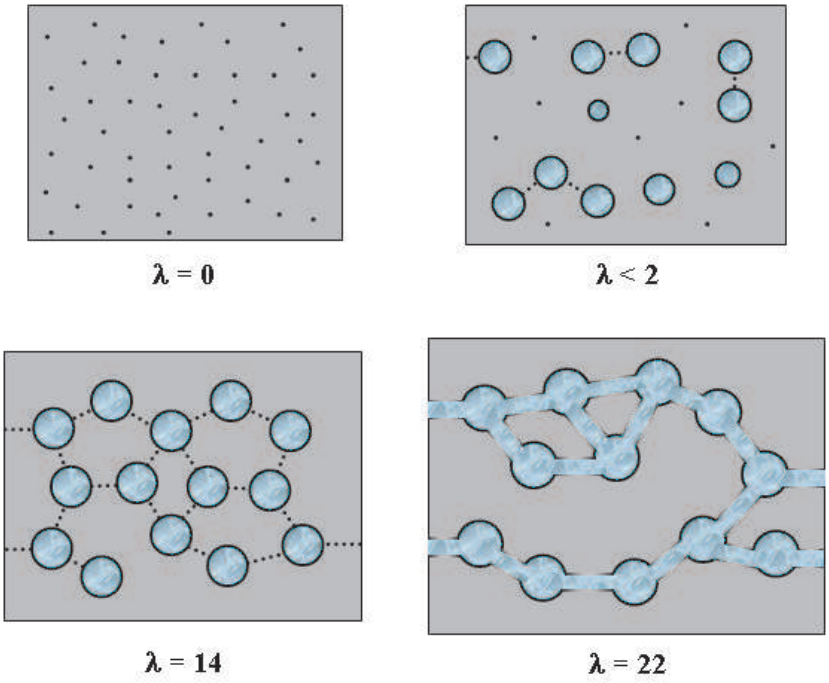

Figure 4.3: Evolution of the membrane structure as a function of water content, λ (moles of water per mole of sulfonic acid sites). The pictures are cross-sectional representations of the membrane, where the gray area is the fluorocarbon matrix, the black is the polymer side chain, the blue is the liquid water, and the dotted line is a collapsed channel. Courtesy of Adam Z. Weber, Lawrence Berkeley National Laboratory

expressed as

$$N_{H_2O} = S\left[-\left(\alpha_l + \frac{\sigma_3^p\,\xi_l^2}{F^2}\right) V_{H_2O}\nabla p_l - \frac{\sigma_3^p\,\xi_l}{F}\nabla\phi_p\right] + (1-S)\left[-\left(\alpha_g + \frac{\sigma_3^p\,\xi_g^2}{F^2}\right)\nabla\mu_{H_2O} - \frac{\sigma_3^p\,\xi_g}{F}\nabla\phi_p\right], \tag{4.34}$$

where S is the fraction of expanded channels, which is used as a weighting function for the two transport modes. This is not a rigorous treatment, but it has a physical basis.
The stationary membrane model developed by Weber and Newman [58] is extended to the non-equilibrium case. The following time-dependent balance equation is obtained

$$\frac{\rho_m}{EW}\partial_t\lambda + \nabla\cdot N_{H_2O} = 0\,. \tag{4.35}$$

α is the transport coefficient, and is basically a modified diffusion coefficient or permeability. It relates the water flux in the absence of protonic current to its chemical potential gradient. In the case of a vapor-equilibrated membrane, the transport coefficient is given by

$$\alpha_g = \frac{c_{H_2O}\,D^m_{H_2O}}{R\,T\,(1-x_{H_2O})}\,. \tag{4.36}$$

To use this equation, three functions are needed. The membrane water concentration is given by

$$c_{H_2O} = \frac{\rho_m}{EW}\lambda\,. \tag{4.37}$$

The water mole fraction is given by $x_{H_2O} = \lambda/(\lambda+1)$. Finally, for the diffusion coefficient $D^m_{H_2O} = 1.8\cdot 10^{-5} f$ is used. The transport coefficient for the liquid-equilibrated case can be expressed as

$$\alpha_l = \frac{K_{sat}}{\mu_l\,V^2_{H_2O}}\left(\frac{f}{f_l}\right)^2\,. \tag{4.38}$$

K_{sat} denotes the absolute permeability, that is, the permeability of a completely liquid-filled membrane. f_l is the maximum value of the water volume fraction that is obtained in the liquid-equilibrated case. The liquid pressure is linked to the channel radius and the contact angle using the Laplace equation

$$p_l = -\frac{2\,\sigma_{H_2O}\,cos\,\theta_3}{r_c}\,, \tag{4.39}$$

where σ_{H_2O} is the surface tension of water. The expanded channel-cluster network is treated as a bundle of capillaries. Liquid pressure, surface tension, and contact angle are used to calculate the critical radius r_c. If $r > r_c$, the channels are expanded. If $r < r_c$, the channels are collapsed since the membrane is slightly hydrophobic. The channel-size distribution based on a fit to pore-size distribution measurements is given in [58]. Integration of the normalized differential volume of channels of radius r from the critical radius to infinity results in the fraction of expanded channels

$$\int_{r_c}^{\infty} V(r) = S = \frac{1}{2}\left[1 - erf\left(\frac{ln\, r_c - ln\, 1.25}{0.3\,\sqrt{2}}\right)\right] . \tag{4.40}$$

The electro-osmotic coefficient in the liquid-equilibrated mode is given by

$$\xi_l = 2.55\, exp\left(\frac{4000}{R}\left(\frac{1}{T_{ref}} - \frac{1}{T}\right)\right) . \tag{4.41}$$

In the vapor-equilibrated mode, $\xi_g = \lambda$ holds if $\lambda < 1$ and $\xi_g = 1$ if $\lambda \geq 1$.
In addition, an equation is required that correlates the humidity of the membrane to the relative humidity in the electrodes. Detailed models have been proposed for this purpose. Futerko and Hsing [69] used a modified version of the Flory-Huggins model. A similar treatment using the same type of chemical equilibrium but a different thermodynamic approach was proposed by Weber and Newman [58]. In contrast, Springer [25] simply used a third-order polynomial to fit the water content of the membrane vs. the water vapor activity. Thampan [70] showed that the water-sorption characteristics of Nafion can be modeled by an Brunauer-Emmett-Teller (BET) equation. The BET approach assumes multiple layers of water on the pores inside the membrane. This approach is used here since it provides a single equation linking the membrane humidity with the relative humidity. The parameters used are based on a physical model.

$$\frac{\lambda_v}{\lambda_m} = \frac{[C\, RH/(1-RH)][1-(n+1)RH^n + n\, RH^{n+1}]}{1+(C-1)\, RH - C\, RH^{n+1}} \tag{4.42}$$

λ_m is the water loading at monolayer coverage. RH denotes the relative humidity at the interface between the membrane and the catalyst layer. Finally, n is the total number of water layers in the pores at saturation. If there is any liquid water in contact with the membrane, the gases are saturated corresponding to $RH = 1$. In this case, the humidity of the membrane is given by

$$\lambda = \lambda_v + S(\lambda_l^{max} - \lambda_v^{max}) . \tag{4.43}$$

λ_v^{max} and λ_l^{max} are the maximum membrane humidity values of a membrane that is in contact with saturated vapor and liquid water at the operating conditions,

respectively. The electrochemical potential of water in the membrane in terms of the water vapor activity is given by $\mu_{H_2O} = RT\ ln(a_{H_2O})$. The water vapor activity can be expressed by $\theta_a c_{H_2O}$, where θ_a is the activity coefficient. The water concentration in turn is a function of the membrane humidity that is given by Eq. (4.37). Additionally, if there is liquid water present, the continuity of the capillary pressure is assumed.

4.5 Numerical solution of the time dependent PDEs

The mathematical model is a system of time-dependent partial differential equations (PDE). The software package FEMLAB^{TM} [47] is used to solve the system of equations. In order to provide a good initial estimate for the time-dependent problem, the corresponding stationary problem is solved first. The equations are converted to a weak form that is connected to a variational principle. The problem is discretized using the Galerkin finite-element method. An affine invariant of the damped Newton method is used to solve the resulting system of nonlinear equations. The time-dependent equations are discretized only in space using the Galerkin method. The result is a system of ordinary differential equations in time. This procedure is known as the method of lines. The different transport processes and the electrochemical reactions occur on very different time-scales. For an explicit solution scheme, only the shortest time-scale matters. This imposes a severe restriction on the size of the time-steps, making the explicit scheme very inefficient in this case. Hence, the implicit solver ode15s provided by MATLAB^{TM} is used for the time discretization. The ode15s is a variable-order multistep solver based on the numerical differentiation formulas. The time-steps and the formulas are changed dynamically.

4.6 Discussion of important model parameters

In the following section, an overview of the most important model parameters is given. The significance of the different parameters is discussed and the method of obtaining the parameter values is outlined.
A Tafel slope of 60 mV/dec is generally obtained from measurements at a low current density that corresponds to a low cathode overpotential, lower than about 400 mV. The corresponding values of the oxygen reduction reaction are $z_c = 2$ and $\alpha_c = 0.5$. For high cathode overpotential, a Tafel slope of 120 mV/dec is generally observed [71]. Assuming that the first electron transfer is the rate-determining step, $z_c = 1$, the transfer coefficient is computed as $\alpha_c = 0.5$. The exchange current density of the O_2 reduction reaction at the Pt-Nafion interface correspond-

ing to each Tafel slope is reported in [72]. For the 120 mV region, a value of $1 \cdot 10^{-3}$ A/m^2 is reported. For low cathode overpotential, the corresponding value is $2 \cdot 10^{-5}$ A/m^2. The values are calculated using the geometric surface area. The Tafel slope and the corresponding exchange current density were measured at a temperature of $T_{ref} = 298$ K using O_2 at a pressure of one atmosphere. This results in $x_{O_2}^{ref} = 1$. Under these conditions, the reversible potential for the oxygen reduction at Pt-Nafion is $\Delta\phi_{eq} = 1229$ mV [73]. The occurrence of mixed potentials is neglected. Based on transmission electron microscope (TEM) images, the average Pt particle size in the catalyst layer is estimated to be between 1 nm and 3 nm. The thickness of the catalyst layer is 10 μm. Using a Pt loading of 0.4 mg/cm^2, the active surface area per volume is estimated to be of the order of $a = 10^7$ m^2/m^3. As an example, a TEM image of a catalyst layer is shown in Fig. 4.4.

Commonly the gas diffusion layers used in fuel cells are teflonized to provide a hydrophobic surface. The contact angle of water for the hydrophobic coating (PTFE) is about 108° when measured for water droplets on flat and smooth surfaces [66]. Rough hydrophobic surfaces exhibit a higher contact angle, which is influenced by the actual contact area between the solid and the liquid droplet. Taking this into account, the contact angle of water in the diffusion medium is assumed to be 115°. Prior to assembly, the carbon paper has a porosity of 0.7 to 0.8. The gas diffusion layers are compressed in the assembled fuel cell. Hence, a porosity of the diffusion media of $\pi_{1,5} = 0.4$ is assumed. The Kozeny-Carman relation gives an empirical estimate of the absolute permeability of the gas diffusion layer. Using a fiber diameter of $d_f = 7\mu$m, and a Kozeny constant of $k_K = 6$ it follows for the absolute permeability

$$K_{1,5} = \frac{\pi_{1,5}^2 \, d_f^2}{16 \, k_K \, (1-\pi_{1,5})^2} = 2.3 \cdot 10^{-13} \, m^2. \tag{4.44}$$

Ihonen et al. [74] measured the through-plane permeability of non-compressed gas diffusion media. They obtained values ranging from $1.8 \cdot 10^{-11}$ m^2 to $3.3 \cdot 10^{-13}$ m^2 for commercial GDLs without a microporous layer. Compression decreases the permeability, and hence the use of $K_{1,5} = 1 \cdot 10^{-14}$ m^2 is consistent with the experimental values. This value is also used in previous publications on liquid water transport in fuel cells; see e.g. Berning et al. [53].

The porosity of the catalyst layer is investigated in [75] using the results of gas porosimetry and mercury porosimetry measurements. For a Nafion content between 0.30 and 0.50, the porosity varies from 0.5 to 0.15. Based on that investigation, the porosity of the catalyst layer is assumed to be $\pi_{2,4} = 0.4$. The catalyst layer consists of Nafion, carbon, and Pt particles. While the Pt particles can be expected to have little effect on the liquid water transport, the main components,

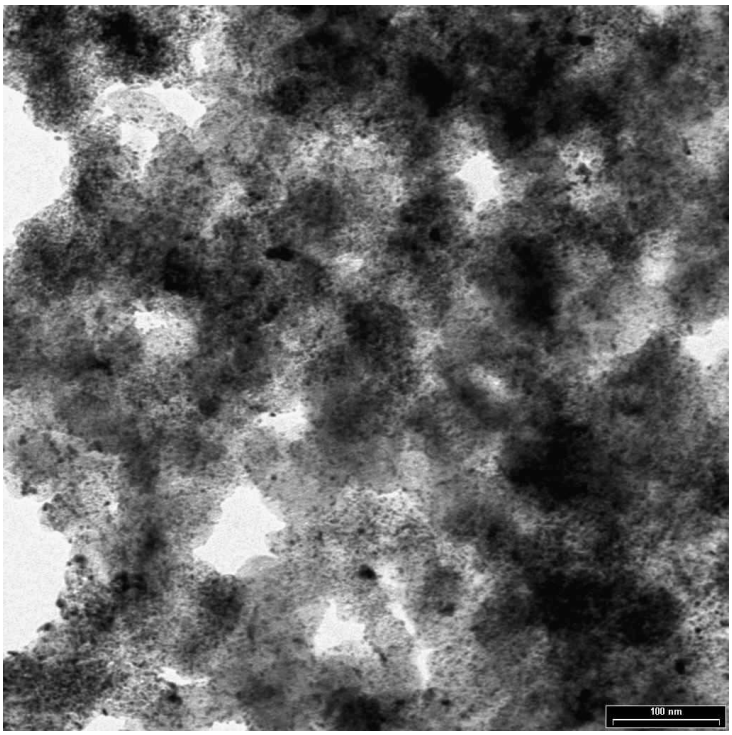

Figure 4.4: TEM image of the catalyst layer of a GORE^{TM} PRIMEA^{TM} 5510 MEA. Cross-sections of an epoxy embedded MEA were prepared using the ultramicrotomy technique. The slice shown is about 100 nm thick. In the TEM picture, the small black dots are single catalyst particles. The larger circular features are the carbon black support. The ionomer appears light gray. The white areas in the TEM image are macropores in the catalyst layer.

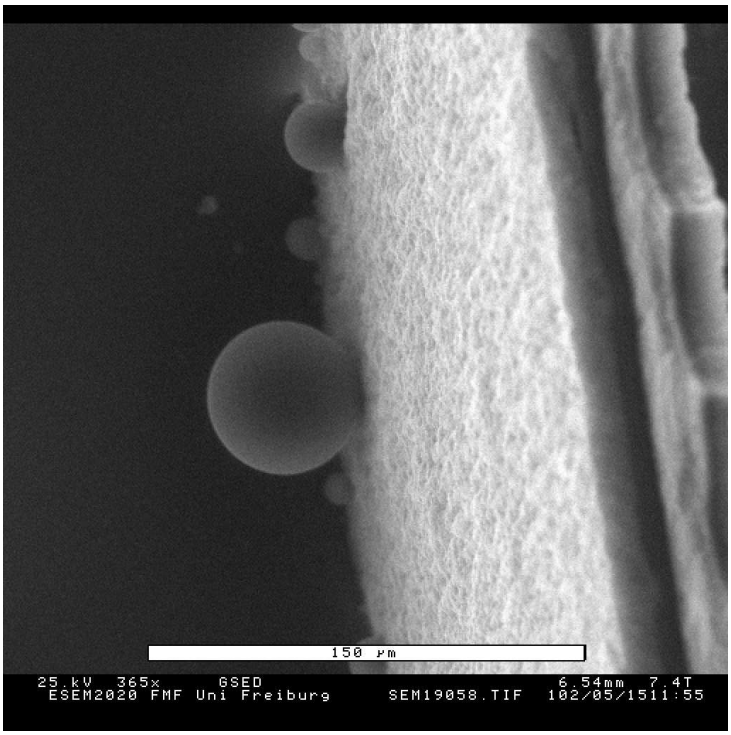

Figure 4.5: Example of an ESEM picture of a GORE^{TM} PRIMEA^{TM} 5510 MEA. In the central part of the picture some water droplets with a radius below 100 μm are shown. The water droplets are on top of the rough surface of the catalyst layer, which is in contact with the GDL in the assembled fuel cell. The image indicates the hydrophobic character of the catalyst layer.

Nafion and carbon, determine the liquid water transport characteristics. Depending on the Nafion content and the humidification state, the catalyst layer can show either hydrophobic or hydrophilic behavior. In this work, the catalyst layer is treated as an effective medium, hence requiring an effective contact angle. Due to the lack of comprehensive experimental data, measurements using the environmental scanning electron microscope (ESEM) were made. In Fig. 4.5 an ESEM picture of the catalyst layer surface is shown as an example. Rough hydrophobic surfaces exhibit an apparent contact angle θ_a larger than the intrinsic contact angle. Due to the roughness of the surface, the measured contact angle is increased compared to the contact angle of a perfectly smooth surface. According to [76], the apparent contact angle and the intrinsic contact angle are linked by

$$\theta_{2,4} = arccos\left(\frac{1+cos\,\theta_a}{\phi_s - 1}\right). \tag{4.45}$$

Based on Fig. 4.5 and similar ESEM pictures, the apparent contact angle is determined to be $\theta_a = 135^\circ$. ϕ_s is the ratio of the actual solid-liquid contact area under the droplet to the nominal base area. Assuming $\phi_s = 0.5$, we obtain an intrinsic contact angle of $\theta_{2,4} = 115^\circ$. The absolute permeability of the catalyst layer is assumed to be $K_{2,4} = 1 \cdot 10^{-14}$ m^2.
For the permeability of a completely liquid-filled membrane, the value quoted in [58] is adopted, $K_{sat} = 1.8 \cdot 10^{-18}$ m^2. It should be noted, however, that this value varies widely in the literature. The contact angle of Nafion has been measured. For example, slightly hydrophilic angles for contact with liquid water have been reported. The hydrophobicity of Teflon is approached as the membrane dries out. Based on freezing-point depression experiments of the liquid-phase water in Nafion, Weber and Newman estimated the contact angle of the membrane to be $\theta_3 = 90.02^\circ$ [58]. A precise value of the contact angle of the membrane is important since the liquid pressure p_l in the membrane is proportional to $cos\,\theta_3$.
The determination of the condensation rate constant is mainly based on the derivation given in [66]. The condensation rate constant k_c depends on the specific interfacial area between the liquid and the gas phase A_{lg}/V. It is assumed that A_{lg}/V is 30% of the specific interfacial area between the solid and the fluid A_{sf}, which is empirically determined by

$$\frac{A_{sf}}{V} = \frac{4\,(1-\pi_{1,5})}{d_f} = 3.4 \cdot 10^5\,\frac{m^2}{m^3}\,, \tag{4.46}$$

where $\pi_{1,5} = 0.4$ and $d_f = 7\ \mu$m. Furthermore, the condensation rate constant depends on the mean molecular speed. From the Maxwell distribution of speeds it follows that

$$v_m = \sqrt{\frac{8\,R\,T}{\pi\,M_{H_2O}}} = 592\,\frac{m}{s} \tag{4.47}$$

at 298 K for water vapor. Finally, a mass accommodation coefficient δ influences the condensation, which is assumed to be $7 \cdot 10^{-4}$. Putting all this together, the condensation rate constant is obtained from kinetic theory, as $k_c = v_m \, \delta \, A_{lg}/(4\,V) = 1 \cdot 10^4 \; s^{-1}$.

4.7 Investigation of cyclic voltammograms

In this section, modeling results are compared with experimental results. This comparison shows the validity of the modeling approach by comparing the cell behavior as predicted by the model with the experimentally measured behavior.
A potential sweep experiment was used to validate the model. The sweep experiment allows one to study the important problem of liquid water transport in PEMFCs. The cell voltage was varied periodically between 0.9 V and 0.1 V using a constant potential sweep rate of 10 mV/s. The sweep rate of 10 mV/s was chosen since it is appropriate to excite the liquid water accumulation and transport. The result of this measurement is a cyclo-voltammogram. During the experiment, isothermal conditions were maintained at a temperature of 300 K. Dry gases were used. Constant gas flow rates of 50 ml/min and 25 ml/min were applied at the cathode side and the anode side, respectively. A cell voltage of 0.9 V was used as the starting point of the experiment. Prior to the experiment, the cell was operated at a cell voltage of 0.5 V in order to protect the cell from damage if the membrane electrode assembly dried out.
First, the modeling result of the potential sweep experiment is considered. The IV-curve predicted by the model is shown in Fig. 4.6. The first forward sweep between a cell voltage of 0.9 V and 0.1 V is indicated by red squares. The maximum value of the current density is reached at a cell voltage of 0.4 V. A decrease in the current density is predicted in the range between 0.4 V and 0.1 V. During the course of the first backward sweep, indicated by red rhombi, the current density decreases further compared to the forward sweep. Generally, a lower current density is predicted if the cell voltage is increased from 0.1 V to 0.9 V. This results in a strong hysteresis effect between the forward and the backward sweep. The second forward sweep is indicated by blue downward-pointing triangles. In the range between a cell voltage of 0.9 V and 0.5 V, the first and the second forward sweep are similar. At lower cell voltage, a significantly lower current density is predicted for the second forward sweep. There is also a hysteresis effect during the second cycle. Subsequent cycles show identical behavior to the second cycle. They are not shown in Fig. 4.6.
The experimentally measured current-voltage characteristic is shown in Fig. 4.7. The first forward sweep from 0.9 V to 0.1 V is indicated by red squares. In the experiment, the maximum of the current density is reached at a cell voltage of 0.3 V.

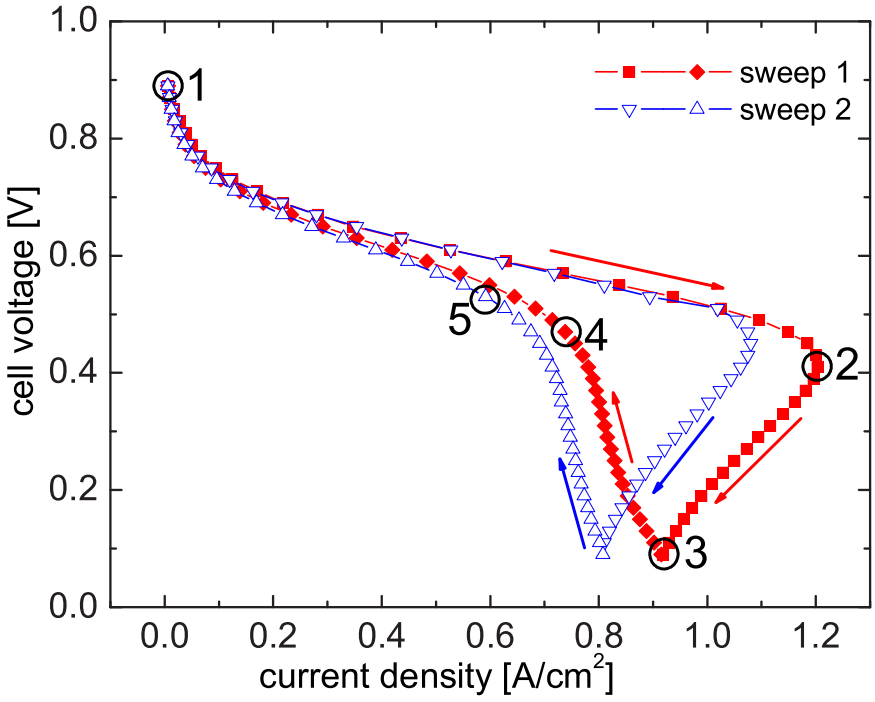

Figure 4.6: Simulation of the potential sweep experiment. The cell voltage is cycled between 0.9 V and 0.1 V. The duration of one cycle is 160 s. The first two cycles are shown. A hysteresis effect of the current-voltage relation is found for both cycles. Subsequent cycles are identical with the second cycle. They are omitted in the interest of clarity. The numbers mark specific points in the current-voltage characteristics and refer to Fig. 4.13 and Fig. 4.14.

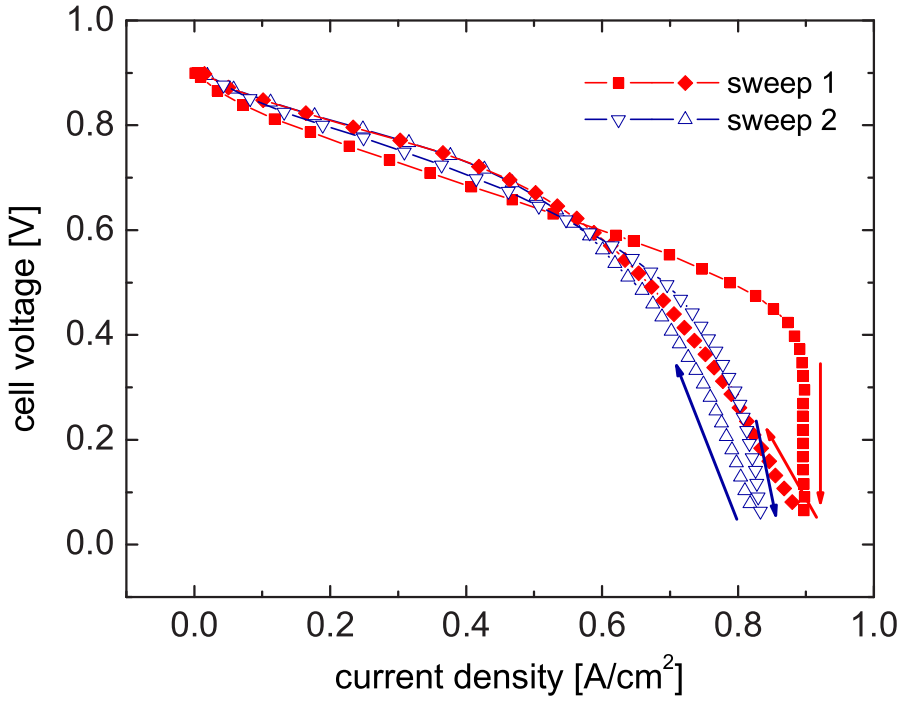

Figure 4.7: Measurement results of the potential sweep experiment are shown. The first cycle is indicated by red symbols. The constant potential sweep rate during the experiment was 10 mV/s, i.e. the duration of one cycle is 160 s. A pronounced hysteresis effect is found in the current density. Subsequent cycles were almost identical with the second cycle. They are omitted in the interest of clarity.

Between 0.3 V and 0.1 V cell voltage there is only a slight decrease in the current density. During the first backward sweep, which is indicated by red rhombi, the current density is generally lower than during the first forward sweep. The first cycle shows a strong hysteresis of the current density, as predicted by the model. The second cycle, indicated by downward and upward-pointing triangles, shows a weaker, but still significant, hysteresis effect. The limiting current density is lower than in the case of the first cycle. This behavior is also predicted by the model.
Fig. 4.8 shows the simulated cell resistance. The red squares indicate the resistance values that correspond to the first forward sweep in Fig. 4.6. With increasing current density, more product water is generated, which humidifies the membrane. Between a current density of 1.2 A/cm^2 and 0.8 A/cm^2 the membrane resistance decreases, even though the current density is decreasing. Hence, the humidification of the membrane is delayed with respect to the generation of product water at the cathode. Subsequently, the resistance remains at a low level compared to the beginning of the simulation. At the end of the first backward sweep and the beginning of the second cycle, i.e. in the high cell voltage region, the resistance increases. The resistance level during the second forward sweep, indicated by blue downward-pointing triangles, is lower than during the first forward sweep. In the high current density region, the resistance decreases again. The first and the second backward sweeps, indicated by red rhombi and blue upward-pointing triangles, respectively, show very similar behavior. The following cycles are identical with the second cycle. For reasons of clarity they are not shown here.
During the potential sweep experiment, the resistance of the cell was recorded. The result is shown in Fig. 4.9. At the beginning of the experiment, a strong increase of the cell resistance is observed. This is caused by the pre-conditioning of the cell. The strong increase of the cell resistance is followed by a decrease until the end of the first forward sweep. During the first backward sweep, indicated by red rhombi, the cell resistance remains at a low level, which increases slightly during the second forward sweep. The second backward sweep, indicated by blue downward-pointing triangles, shows a similar behavior to the first backward sweep. The comparison of the modeling results in Fig. 4.8 and the experiment (Fig. 4.9) shows that the model approach is valid for the prediction of the dynamic evolution of the cell resistance. The dynamic membrane model describes the time-dependent water transport through the membrane coupled with the time-dependent two-phase flow in the catalyst layer and the GDL. For the first time, this approach is validated experimentally.
Fig. 4.10 shows a comparison of measured and simulated IV-curves. In terms of trends the predictions of the model agree well with the measured results. Moreover, the current density that is reached at the lowest cell potential is predicted correctly. However, the differences between the simulated and the observed cyclic voltammograms are up to 30%. A one-dimensional model approach does not in-

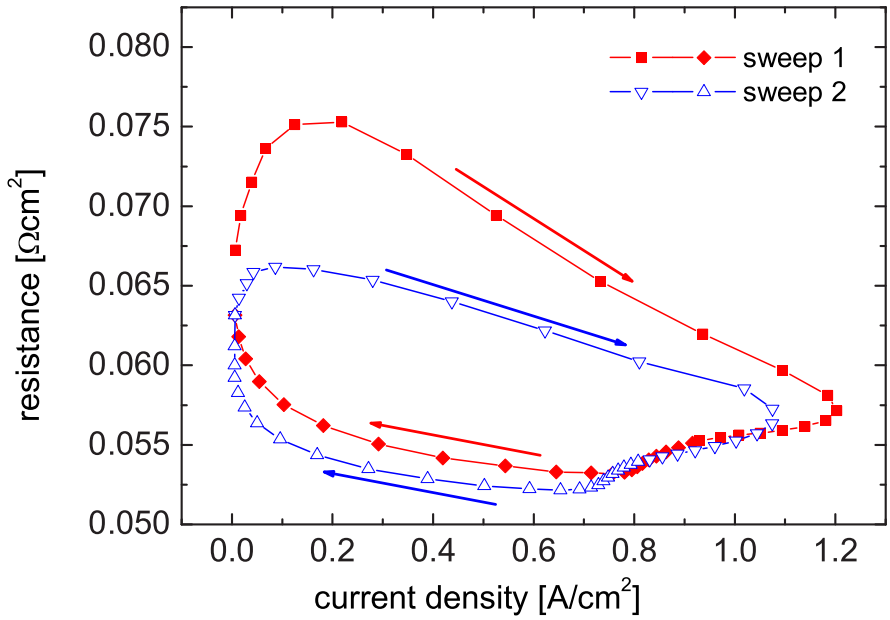

Figure 4.8: Simulated evolution of the cell resistance. During the first cycle, indicated by red squares and rhombi, a strong decrease of the resistance in the high current density region is predicted. The protonic resistance during the first and second backward sweeps shows very similar behavior. During the forward sweep of the second cycle, indicated by blue downward-pointing triangles, the resistance increases but remains at a lower level compared to the first forward cycle.

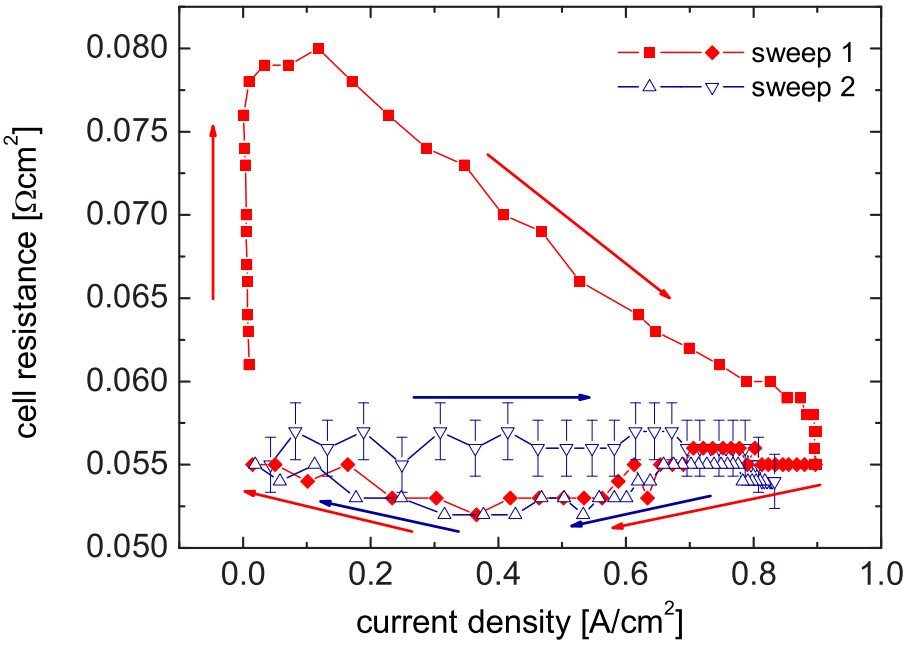

Figure 4.9: Experimentally measured cell resistance. To prevent dry-out, the cell was run at a cell voltage of 0.5 V before the start of the experiment. This causes the cell resistance to rise, which is followed by a linear decrease during the first forward sweep. The first and second backward sweeps, which are indicated by red rhombi and blue upward-pointing triangles, respectively, show very similar behavior. During the second forward cycle, the resistance increases only slightly compared with the backward cycles.

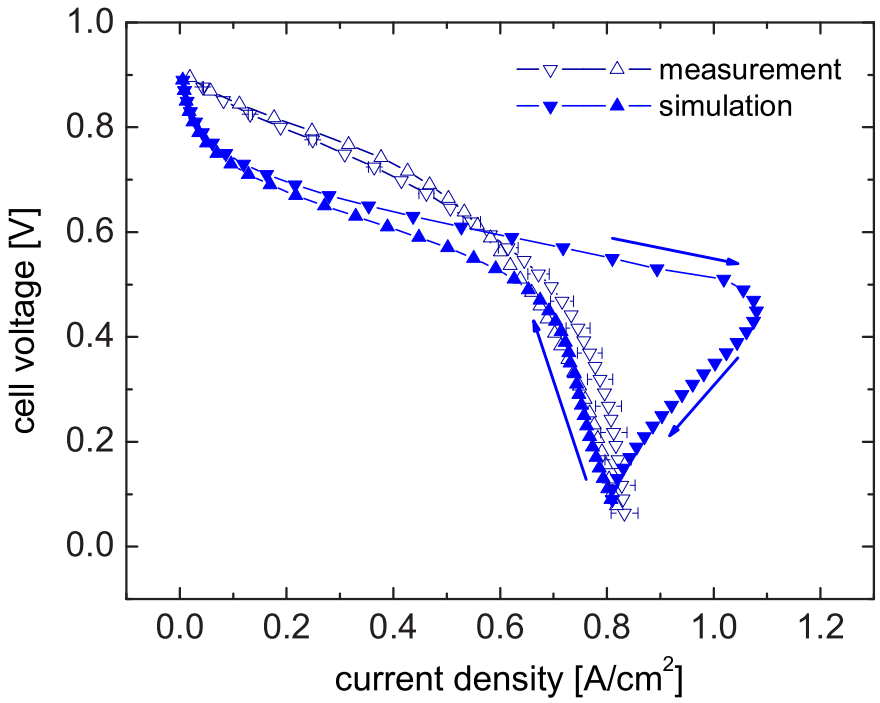

Figure 4.10: This figure shows a comparison of the measurement results and the simulation results of the potential sweep experiment. A sweep rate of 10 mV/s is used in both cases. The measured and the simulated IV-curves agree well in terms of trends. However, the simulation underpredicts the current density at high cell potentials but overestimates the current at medium to low cell potentials.

clude spatial variations of the gas distribution, the temperature, and the material properties. Spatial heterogeneity was reduced as far as possible by using a water-cooled cell and by supplying sufficient oxygen and hydrogen over the small active area. However, some position-dependent effects still present in the test fuel cell are not captured by the one-dimensional model. The cell is cooled with a high coolant flux from a thermostat. The temperature in the end plates was monitored and found to change less than 1 K during the operation. The temperature in the MEA can change more than 1 K due to the thermal resistance caused by the interfaces between the different layers. In [74] the thermal resistance of the interface between the GDL and the end plate is determined to be around 5 $\mathrm{Kcm^2W^{-1}}$. With a rib to channel ratio of 1 : 1, the average heat flux is estimated to be 0.6 $\mathrm{W/cm^2}$ rib area. The corresponding temperature drop between the end plate and the GDL is 3 K. In addition, the interface between the catalyst layer and the GDL must be taken into consideration which would increase the temperature gradient further. However, the heat is removed from the cell on both the cathode and the anode side. The fuel gases serve as an additional coolant. In summary, the temperature does not account for a large part of the difference between measurement and simulation.

More critical is the influence of the gas flow rates included in the boundary conditions of the model. The mass transport limitation, the removal of water, and the rates of condensation and evaporation are influenced by the gas fluxes. Moreover, the gas flow drags liquid water droplets along the channels. Up to now, no rigorous treatment of this effect has been published. To provide a quantitative measure of the impact of the flow rates on the cyclic voltammograms Fig. 4.11 compares three different measurements. In the base case, which is also shown in Fig. 4.10, 50 ml/min air and 25 ml/min hydrogen were used. The use of higher flow rates of 100 ml/min air and 50 ml/min hydrogen or 400 ml/min air and 200 ml/min hydrogen increases the limiting current density significantly. Hysteresis of the IV-curve is observed in all cases.

Furthermore, the double layer capacitance, which is not included in this model, is expected to have an impact on the cyclic voltammograms. The constant change of the cell potential causes a continuous discharging of the double layer. The in-situ properties of the fuel cell components are a further source of error. The porosity of the GDL changes with the contact pressure. Normally, the porosity is lower below the ribs of the flow plates. Moreover, the permeability is influenced by the contact pressure and is expected to be non-uniform across the GDL. Furthermore, the capillary pressure-saturation relations that are commonly used in fuel cell modeling are not specifically adjusted for the description of the fuel cell components. This point requires experimental investigation in future research. The situation for the contact angle is similar. The surface contact angle of the catalyst layer was measured by ESEM. Similar data for the GDL can be found in the literature. However,

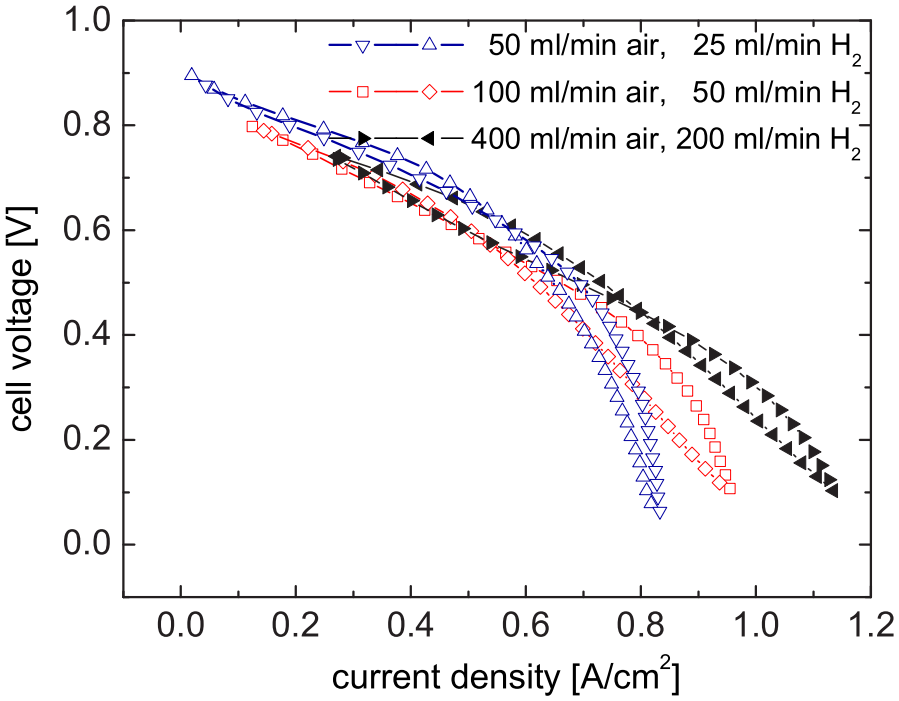

Figure 4.11: This figure shows the influence of different flow rates on the measurement results. In the base case (Fig. 4.6) flow rates of 50 ml/s dry air at the cathode side and 25 ml/s dry hydrogen at the anode side are used. Increasing the flow rates leads to a significant shift of the cyclic voltammograms.

there is a gap between the surface properties and the bulk properties which has to be closed by a rigorous treatment that also considers the issue of mixed wettability. The hydraulic characteristic of porous media with mixed wettability was investigated e.g. by Ustohal, Stauffer and Dracos [77].
In the model the product water is assumed to be generated as water vapor in the base case (Fig. 4.6). Liquid water is formed by condensation, accumulates and leads to the hysteresis. One could also assume that the water is generated in the liquid phase. Fig. 4.12 shows a comparison of the two possible water generation assumptions. If the water is assumed to be generated in the liquid phase (case B), the mass transfer losses are overestimated compared to the base case. If the product water is liquid no condensation is necessary for the accumulation effect. Hence, the flooding of the cathode is faster and stronger than in the base case.

4.8 Analysis of the cyclic voltammograms

A pronounced hysteresis effect of the current-voltage characteristic is predicted by the modeling results and observed in the potential sweep experiment. In the following section, an analysis of this hysteresis effect is given, based on the dynamic fuel cell model. Fig. 4.13 shows the fuel cell sandwich, which consists of the gas diffusion layers, the catalyst layers, and the membrane. In the gas diffusion layers and the catalyst layers, the volume saturation of liquid water s_l is indicated by solid lines. In the membrane, the mean value of the fraction of expanded channels S_{mean} is indicated. The numbers refer to Fig. 4.6, where specific points in the current voltage characteristic are marked.
At the beginning of the sweep experiment (1), the distribution of the liquid water is almost uniform across the cell. In the membrane, the fraction of expanded channels is small at the beginning of the first cycle (1). The highest current density is reached at a cell voltage of 0.4 V (2). According to the results of the model, the liquid water saturation is still low at this point. While an increase in the liquid water saturation is observed at the cathode, the anode side shows a small decrease of s_l. This is due to the influence of the electro-osmotic drag, which is high in the high current density regime. The fraction of expanded channels in the membrane is still small at point (2). In contrast to the electro-osmotic drag, the accumulation of liquid water shows a delay with respect to the time evolution of the current density. This is indicated by the relatively strong increase in the liquid saturation between the highest current density (2) and the end of the first forward sweep (3). The saturation of liquid water shows a further increase during the first backward sweep, where the relative maximum is reached between 0.4 V and 0.5 V cell voltage (4). This leads to the observed hysteresis behavior. The absolute maximum liquid water saturation is seen during the backward sweep of the second cycle (5).

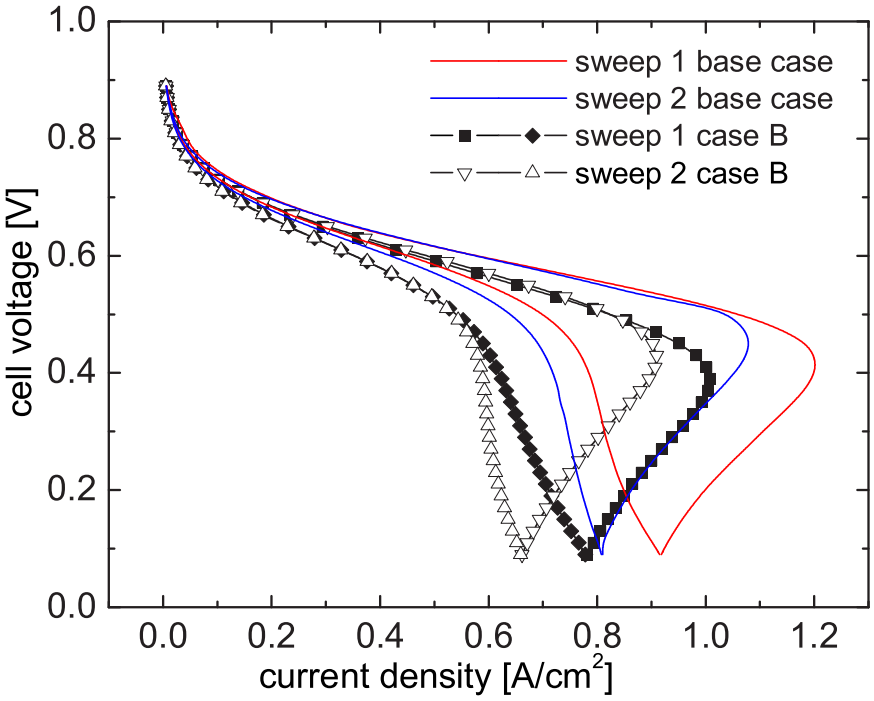

Figure 4.12: Comparison of two different assumptions regarding the generation of the product water at the cathode. In the base case the water is assumed to be generated as water vapor. case B shows the simulated IV-curves if the water is assumed to be generated in the liquid phase. case B shows an increased mass transfer resistance compared to the base case.

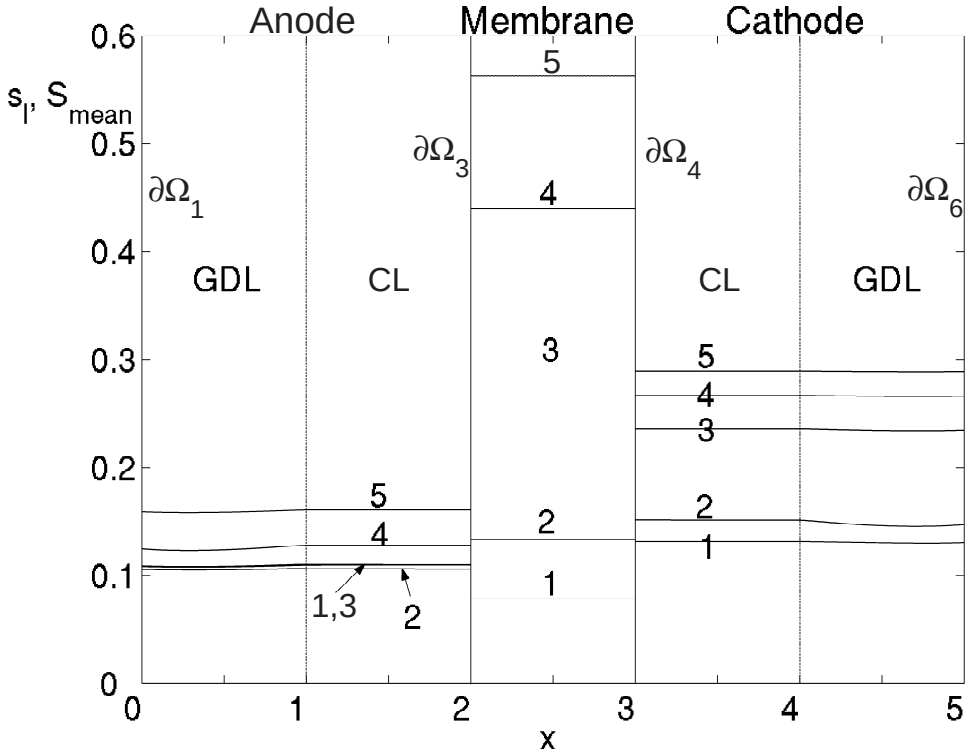

Figure 4.13: This graph shows the volume saturation of liquid water s_l in the gas diffusion layers (GDL), and the catalyst layers (CL). In the membrane, the average fraction of expanded channels S_{mean} is shown. During the experiment, the liquid water saturation and the fraction of expanded channels in the membrane increase. On the anode side, the saturation of liquid water remains low due to the influence of the electro-osmotic drag of water from the anode to the cathode. The numbers refer to Fig. 4.6 and have the following meaning: (1) start of first cycle, (2) maximum current density, (3) minimum cell voltage, (4) maximum liquid water saturation during first cycle, (5) maximum of liquid water saturation during second and subsequent cycles. Normalized coordinates corresponding to Fig. 4.1 are used.

The time-span between the highest current density and the maximum value of the liquid water saturation in the cathode is between 70 s and 80 s. The liquid water accumulation on the anode side is generally weaker than on the cathode side due to the electro-osmotic drag. The fraction of expanded channels S in the membrane influences the water transport through the membrane in accordance with Eq. (4.34). The liquid water saturation at the interfaces between the catalyst layers and the membrane, $\partial\Omega_3$ and $\partial\Omega_4$, and the fraction of expanded channels S are coupled. The higher the liquid water saturation, the smaller is the critical radius in Eq. (4.40). This is the smallest possible radius of pores that are expanded. Correspondingly, the fraction of expanded channels, and, hence, the amount of water that is driven through the membrane by a pressure gradient, increases during the experiment. This is shown in Fig. 4.13 in the membrane subdomain at the points (3),(4), and (5).

In Fig. 4.14, the normalized charge generation rate $Q^C_{norm} = \left| Q_{c/a,C} / Q^{mean}_{c/a} \right|$ is shown. This allows one to identify those regions of the catalyst layers that are most active during the course of the experiment. The influence of the liquid water accumulation on the electrochemical reactions can be seen. Fig. 4.14 shows the catalyst layers of the anode side and the cathode side that are separated by the membrane. The numbers refer to different points of the current-voltage characteristic that is shown in Fig. 4.6. On the anode side, the distribution of the charge generation rate is close to stationary during the sweep experiment. The catalyst layer of the anode side is most active close to the membrane, where the difference between the the electronic potential ϕ_e and the protonic potential ϕ_p is highest. There is no mass transfer limitation for hydrogen. On the cathode side, the behavior is different. At the beginning of the experiment (1) and during the first forward sweep (2), the charge generation is distributed more uniformly over the catalyst layer than on the anode side. This is due to the slower reaction kinetics of the oxygen reduction reaction compared to the hydrogen oxidation reaction. When liquid water accumulates on the cathode side, the distribution of the charge generation changes dramatically. During the first backward sweep between 0.1 V and 0.9 V (3,4) and during the second cycle (5), the catalyst layer is only active close to the gas diffusion layer of the cathode side. The reason is the strong mass transport limitation for oxygen on the cathode side due to the accumulation of liquid water. A comparison with the behavior of a self-breathing fuel cell highlights the importance of efficient water-management. Fig. 3.18 shows that the catalyst layer is most active close to the membrane in case of a partially hydrated ionomer. The utilization of the platinum catalyst particles is most efficient if the ionomer is fully hydrated. However, flooding of the catalyst layer must be avoided.

Fig. 4.15 compares measured cyclic voltammograms with different sweep rates. The base case with a sweep rate of 10 mV/s used in Fig. 4.10 is compared to a

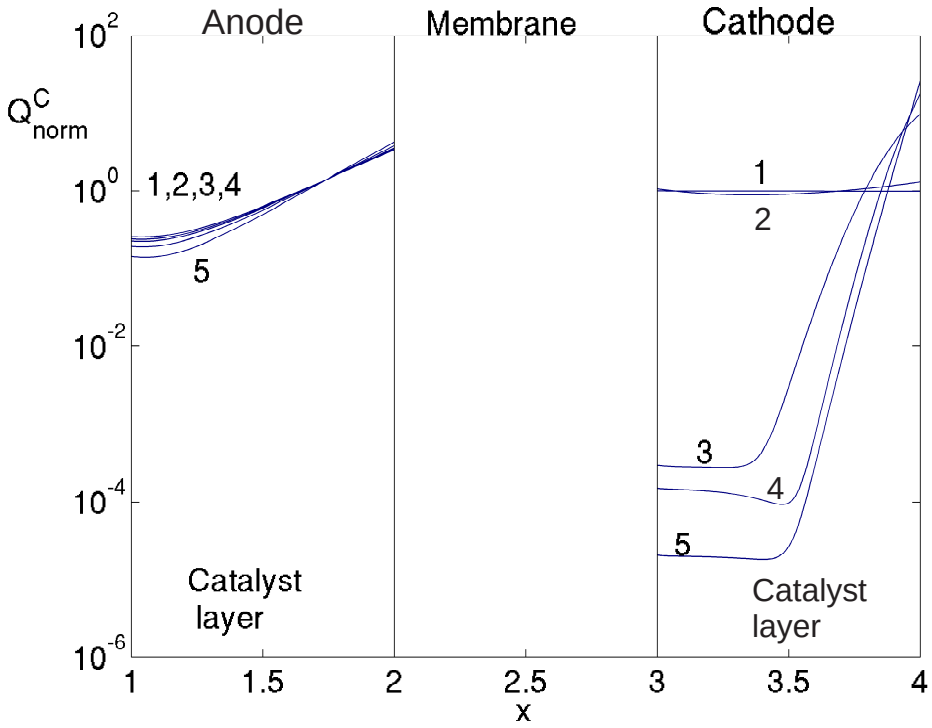

Figure 4.14: The normalized charge generation rate Q^C_{norm} is shown on a logarithmic scale. Q^C_{norm} is defined by $\left|Q_{c/a,C}/Q^{mean}_{c/a}\right|$, where $Q^{mean}_{c/a}$ is the average charge generation rate in the catalyst layer of the cathode and the anode, respectively. The results show the influence of the liquid water saturation on the activity of the cathode. Normalized coordinates corresponding to Fig. 4.1 are used.

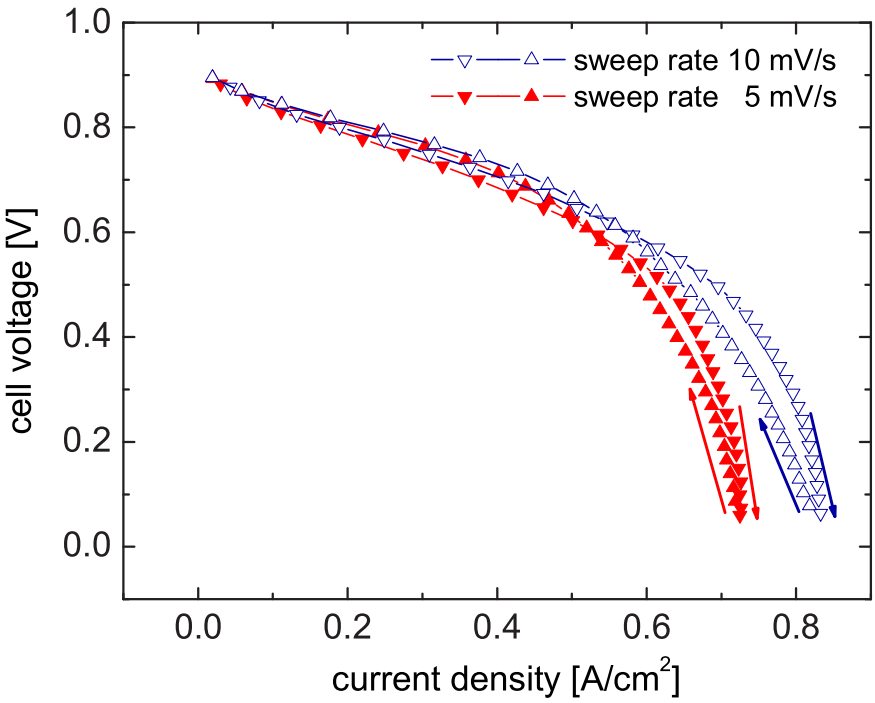

Figure 4.15: Cyclic voltammograms with different sweep rates are compared. The hysteresis effect is found in both cases. The limiting current density is smaller in case of the smaller sweep rate.

measurement with a sweep rate of 5 mV/s. While hysteresis is observed in both cases, the mass transport resistance in the high current density region is larger in case of the lower sweep rate. This is consistent with the explanation of the hysteresis due to the accumulation of liquid water at the cathode. The modeling results show the same trend. Fig. 4.16 compares simulation and measurement for two different sweep rates.

4.9 Characteristic frequencies of water transport

The most important feature of the mathematical model developed in section 4.4 is the coupled time-dependent description of the two-phase flow and the water transport across the membrane. Thus, the model facilitates the investigation of the liquid water transport through the GDL and the water transport across the membrane in the liquid-equilibrated case. The characteristic frequencies and time constants associated with these transport phenomena are derived in the following. First, the transport equation that describes the water flux across the membrane is rewritten. Combining Eq. (4.34), Eq. (4.35) and Eq. (4.43) yields

$$\begin{aligned} 0 = &\frac{\rho_{dry}}{EW}\partial_t\left[\lambda_v + S(\lambda_l^{max} - \lambda_v^{max})\right] \\ &+\nabla\cdot\left(S\left[K_l\nabla p_l + D_l\nabla\phi_p\right] + (1-S)\left[K_g\nabla\mu_{H_2O} + D_g\nabla\phi_p\right]\right) . \end{aligned} \tag{4.48}$$

where $K_l = -\left(\alpha_l + \frac{\sigma_3^p\,\xi_l^2}{F^2}\right)V_{H_2O}$, $D_l = -\frac{\sigma_3^p\,\xi_l}{F}$, $K_g = -\left(\alpha_g + \frac{\sigma_3^p\,\xi_g^2}{F^2}\right)$, and $D_g = -\frac{\sigma_3^p\,\xi_g}{F}$. Applying the principle of superposition, thereby assuming that the water transport mechanisms in the vapor-equilibrated and liquid-equilibrated case are independent, this equation can be written as the sum of two differential equations. The first equation describes the vapor-equilibrated case. The driving force of the diffusive water flux is the gradient of the electrochemical potential across the membrane:

$$\frac{\rho_{dry}}{EW}\partial_t\lambda_v + \nabla\cdot(1-S)(K_g\nabla\mu_{H_2O} + D_g\nabla\phi_p) = 0 \tag{4.49}$$

The second equation describes the liquid-equilibrated case. In that case the driving force is the gradient of the liquid pressure across the membrane:

$$\frac{\rho_{dry}}{EW}(\lambda_l^{max} - \lambda_v^{max})\partial_t S + \nabla\cdot S(K_l\nabla p_l + D_l\nabla\phi_p) = 0 . \tag{4.50}$$

In this equation the term $D_l\nabla\phi_p$ describes the electro-osmotic flux of water. In other words, this is the coupling of the proton current and the water flux through

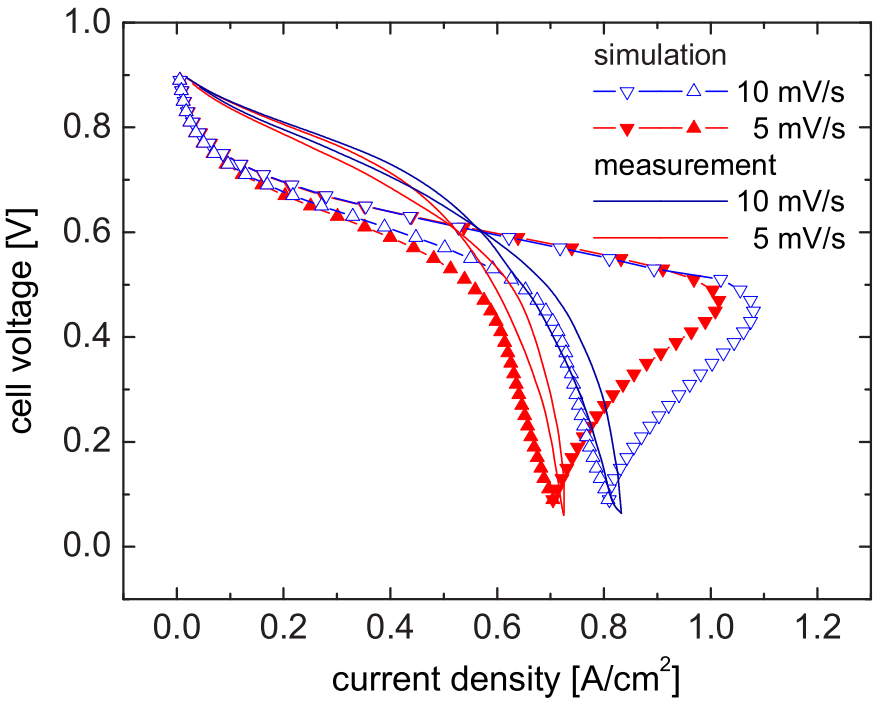

Figure 4.16: The simulated cyclic voltammograms show the same trend as the measured cyclic voltammograms. If the sweep rate is decreased the saturation of the cathode is higher, leading to an increase of the mass transfer resistance.

the membrane. In order to derive the characteristic frequency of the pressure-driven water flux the proton current and the water flux, are assumed to be decoupled, i.e. $D_l = 0$. The transport coefficient K_l relates the water flux in the liquid-equilibrated case to the gradient of the liquid pressure across the membrane. The liquid pressure p_l is a function of the liquid water saturation s_l (Eq. (4.18) and Eq. (4.19)). Hence, the gradient of the liquid pressure can be replaced by a gradient of the saturation s_l. The fraction of expanded channels S can be expressed in terms of the critical pore radius r_c by Eq. (4.40). r_c in turn is a function of the liquid pressure (Eq. (4.39)) and, hence, a function of the saturation s_l. Thus, Eq. (4.50) is rewritten in terms of the saturation as

$$\frac{\rho_{dry}}{EW}(\lambda_l^{max} - \lambda_v^{max})\frac{\partial S}{\partial r_c}\frac{\partial r_c}{\partial s_l}\partial_t s_l + \nabla \cdot S(K_l \frac{\partial p_l}{\partial s_l}\nabla s_l) = 0 \; . \tag{4.51}$$

Rearranging this equation yields

$$\partial_t s_l = \nabla \cdot (D_{m,l}\nabla s_l) \; , \tag{4.52}$$

where the diffusion coefficient $D_{m,l}$ is given by

$$D_{m,l} = -\frac{EW \cdot S \cdot K_l}{\rho_{dry}(\lambda_l^{max} - \lambda_v^{max})}\frac{\partial r_c}{\partial S}\frac{\partial s_l}{\partial r_c}\frac{\partial p_l}{\partial s_l} \; . \tag{4.53}$$

From the simulation results at a cell voltage of 0.5 V a value of $D_{m,l} = 7.5 \cdot 10^{-11}$ m^2/s is extracted. In a fuel cell with a polymer thickness of $d_m = 25$ μm the typical time constant is

$$\tau_{m,l} = \frac{d_m^2}{D_{m,l}} = 8.3 \; s \; , \tag{4.54}$$

corresponding to a characteristic frequency of $\omega_{m,l} = 0.12$ Hz. $\tau_{m,l}$ is the typical time that is needed for the equilibration of a liquid pressure gradient across the membrane.
If the condensation and evaporation of water is neglected the liquid water transport through the GDL is described by

$$\partial_t \left[\pi_\kappa \rho_l s_l\right] + \nabla \cdot \left[\rho_l \vec{v}_l\right] = 0 \; . \tag{4.55}$$

Combining this equation with Eq. (4.15), Eq. (4.19) and Eq. (4.20) yields the Richards equation

$$\partial_t s_l = \nabla \cdot (D_{GDL,l}\nabla s_l) \; . \tag{4.56}$$

The diffusion coefficient is given by

$$D_{l,GDL} = -\sqrt{\frac{K_{GDL}}{\pi_{GDL}}}\frac{\sigma_{H_2O}}{\mu_l}cos(\theta_{GDL})s_l^3 \; (1.417 - 4.24 s_l + 3.789 s_l^2) \; . \tag{4.57}$$

An average saturation of 0.25 in the GDL corresponds to $D_{l,GDL} = 1.2 \cdot 10^{-7}$ m^2/s. A typical thickness of a GDL is 300 μm. In this case, a saturation gradient across the gas diffusion layer is equilibrated within $\tau_{l,GDL} = 0.75\ s$. This corresponds to the characteristic frequency of $\omega_{l,GDL} = 1.3\ Hz$. In contrast to the liquid water transport, the characteristic frequency of the oxygen diffusion through the gas diffusion layer is much larger. Based on Eq. (4.24), the characteristic frequency is estimated to be 18 Hz.

4.10 Simulation of low frequency impedance

AC impedance measurements are a powerful tool to probe fuel cells. Accordingly, there are many publications addressing the use of impedance spectroscopy for fuel cell development. See for example [72] and [78]. State-of-the-art impedance models describe the catalyst layer and the gas diffusion layer of the cathode in detail. Thus, impedance data have been used to understand and improve the electrode performance and the porous gas diffusion backing layer. Electrical impedance spectra are usually measured using frequencies between 10 kHz and 0.1 Hz. An impedance spectrum that is typical for a PEMFC shows two arcs that originate from the influence of the catalyst layer and the gas diffusion layer, respectively. The higher frequency arc reflects the combination of an effective charge transfer resistance and the double-layer capacitance within the catalyst layer. The lower frequency arc reflects the mass-transport limitations in the gas phase within the gas diffusion layer. Model based evaluation of AC impedance spectra provides understanding and optimization guidelines for fuel cell electrodes and gas diffusion backings and can be used for the extraction of parameters and characterization of fuel cell components. Not only the electrochemical reaction, the proton transport, and the transport of the gaseous species, but also the generation and transport of liquid water have been investigated using AC impedance spectroscopy. Song et al. [79] measured impedance spectra of a PEMFC in a frequency range between 10 kHz and 1 mHz. An additional arc in the frequency range below 1 Hz was found. The low frequency arc was supposed to reflect the transport limitation caused by the accumulation of liquid water. Similar measurement results were published in [80]. The mathematical impedance models currently available neglect the two-phase transport of liquid water and the gaseous species. Accordingly, there are no modeling results explaining the observed low frequency arc in the literature. The mathematical model introduced in section 4.4 facilitates the simulation of the low frequency part of the impedance spectrum. The model accounts for the two-phase transport, which is the leading order effect at low frequencies.

Based on the estimation given in the preceding section, an impedance spectrum in

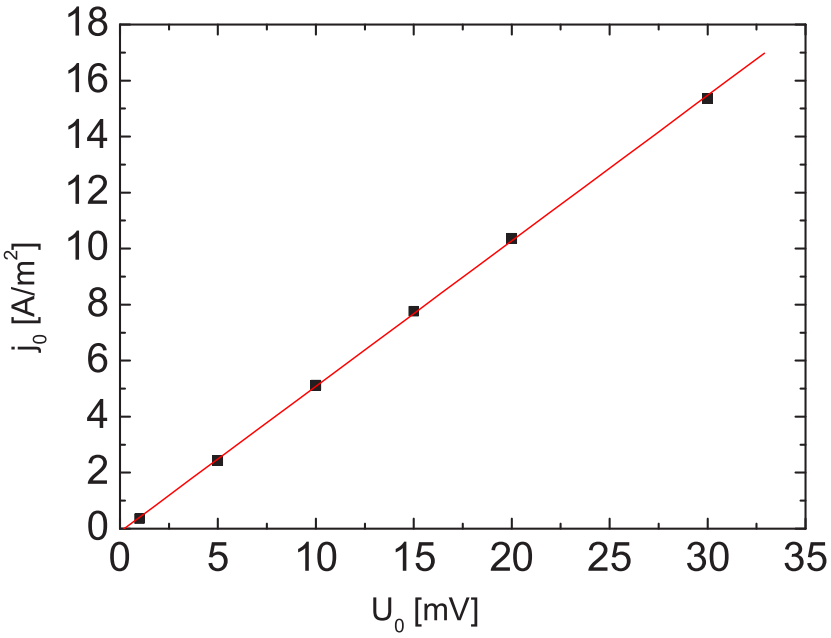

Figure 4.17: This graph shows the magnitude of the simulated output at different oscillation amplitudes. Linearity is observed in a wide range of amplitudes. For the simulation of the impedance spectrum an amplitude of 10 mV was used.

a frequency range between 1 Hz and 1 mHz is simulated. A boundary condition of the form $\phi_e = V_{cell} + U_0\ sin(\omega t)$ was applied at boundary $\partial\Omega_6$. This boundary condition describes the periodic perturbation of frequency ω of the cell voltage applied by a frequency response analyzer during an impedance measurement. For the cell voltage, $V_{cell} = 0.25$ V was used. The fundamental assumption, implicit in the theory of electrochemical impedance spectroscopy, is that the perturbing signal is of low amplitude. In order to excite the liquid water generation and transport significantly, the amplitude of the perturbation cannot be chosen arbitrarily small. In order to ensure that the bounds of linearity were maintained a plot of the amplitude of the output versus the amplitude of the perturbation is shown in Fig. 4.17. For the simulation of the impedance spectrum, an amplitude of $U_0 = 10$ mV was chosen. The resulting Nyquist plot is shown in Fig. 4.18. One single arc in the low frequency region is found. According to the estimation that is given in the preceding section, this spectrum can be explained with the equilibration of a saturation gradient across the membrane. The humidification of the membrane is

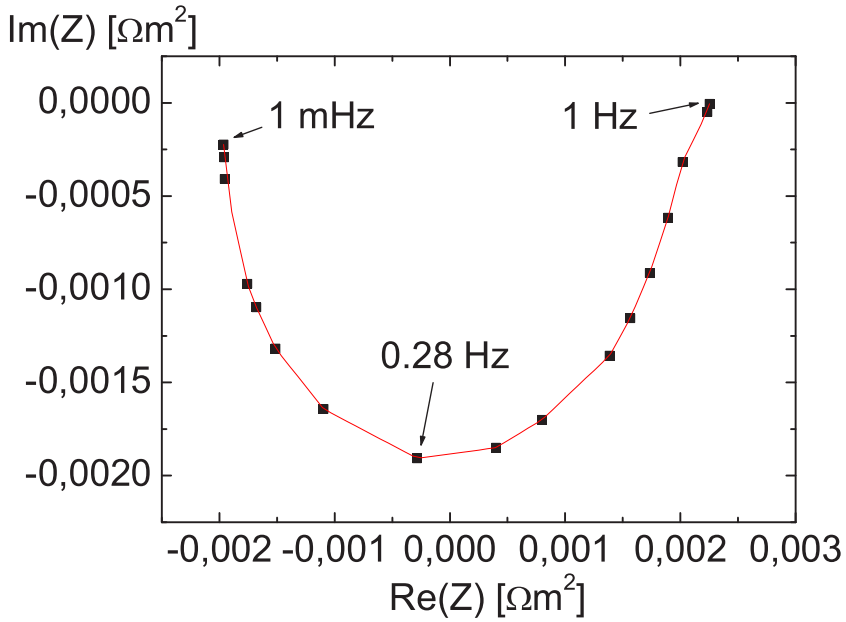

Figure 4.18: The simulated impedance spectrum in a frequency range between 1 mHz and 1 Hz is shown. Based on the estimation given in the preceding section, the impedance arc can be explained with the equilibration of a saturation gradient between cathode and anode across the membrane.

delayed with respect to the water generation in the catalyst layer of the cathode. The estimated characteristic frequency of this process is 0.12 Hz. This is in good agreement with the results shown in Fig. 4.18.

4.11 Conclusion

In this chapter a dynamic model of a proton exchange membrane fuel cell has been developed. The model contains a description of the gas diffusion layers, the catalyst layers, and the membrane. The phase transition between water vapor and liquid water is considered. The model accounts for the transport of the gaseous species and the transport of liquid water. Furthermore, the charge transport and the electrochemical reactions are considered. The couplings between the different processes are included in the model. The model is one-dimensional and isothermal.

During the operation of the fuel cell, the product water accumulates in the gas diffusion layers and the porous electrodes. This process influences the transport of the fuel gases. The result is a current-voltage characteristic that is not stationary, but time-dependent. Most PEMFC models found in the literature are based on a stationary description. However, a stationary model does not explain the experimentally observed behavior, which is time-dependent in the two-phase regime. The liquid water transport occurs on a time-scale of minutes. Flooding effects that are caused by liquid water accumulation are described by this model. The gas saturation is decreased by the presence of liquid water. An important feature of the model is that it describes the reduction of the ionic current density due to the presence of liquid water and the liquid water content in the electrodes couples to a dynamic transport process of liquid water in the porous layers.
The validity of the model approach is shown by a comparison with experimental results. For the first time, the results of a dynamic and two-phase model on a time-scale of minutes are shown and compared with measurement data. Cyclic voltammograms are simulated and measured. The influence of different flow rates and sweep rates on the results is investigated. The test cell has a small active area and is actively water-cooled. The current-voltage characteristic and the evolution of the cell resistance are predicted correctly by the model. A pronounced hysteresis effect is observed in the cyclic voltammograms. The modeling results show that this hysteresis is caused by an increase in the mass transport limitation on the cathode side. This is due to the time-dependent accumulation of water on the cathode side. An important part of the mathematical model is the description of the polymer membrane. The model contains a time-dependent description of the concentration and pressure-driven water transport through the membrane. The membrane model is coupled with the two-phase flow equations in the electrodes. The validity of this novel model approach is shown by the comparison of the measured and the simulated cell resistance.
The mathematical model that is presented here is suitable for explaining the experimentally observed hysteresis behavior of cyclic voltammograms. Hence, it is concluded that the effective medium approach is suitable to describe the water transport in the porous regions. However, the description of the liquid water transport is taken from the field of ground water transport. The porous media that are investigated in this field are considerably larger than the gas diffusion layers and the electrodes of a PEMFC. Moreover, many of the model parameters in the two-phase flow equations are based on literature sources and estimations. In some cases, there is a lack of comprehensive data. Also, the capillary pressure-saturation relation does not capture the difference between imbibition and drainage of the porous layers. Fundamental investigations of the two-phase flow properties of fuel cell components are required in order to improve the data basis. This will improve the accuracy and the predictive power of mathematical

fuel cell models.
The model that is presented here can predict the impact of dynamic changes of the operating conditions on the fuel cell. For example, rapid load changes can be simulated. This topic is important during start-up and operation of a fuel cell system that is subjected to a dynamic load. The model is applied to simulate the low frequency impedance spectrum of a PEMFC. The occurrence of an arc in the sub-Hertz region of a Nyquist plot can be explained by the excitation of the liquid water transport across the membrane.

Chapter 5

Dynamic PEMFC Stack Model

In this chapter a dynamic PEM fuel cell stack model for system simulation is presented. The chapter is organized as follows. Section 5.1 reviews the most recent publications on the topic of PEM fuel cell stack simulation. The focus of this literature review is on the dynamic description of fuel cell stacks. A dynamic, mathematical model of a PEMFC stack is developed in section 5.2 to section 5.5. The model is time-dependent and non-isothermal. It is based on energy and mass balance equations. Heat and mass transfer by convection and conduction within the stack and changes due to the electrochemical reactions and the phase transition of water are taken into account. The mass and heat transport equations are coupled with an electrical model that is based on the Tafel equation and a membrane model that accounts for the net-transfer of water through the membrane.
The most important input parameters of the model are the mass and heat fluxes at the inlet of the stack, the overall current, and the ambient temperature. The solution variables are the heat and mass fluxes at the stack outlet, the temperature of the stack, and the stack voltage. The measurement setup that is used for the validation measurements controls all of the input parameters and records the solution variables of the model. The mathematical formulation of the model is a coupled differential algebraic equation (DAE) system that contains ordinary differential equations in time describing the heat and mass transfer and an algebraic equation for the electrochemical reaction. The DAE is solved using the ode15s solver of MATLAB^{TM}. In section 5.6, simulation results and a comparison of simulation results and measurement results are presented. The simulation results describe the dynamic response of a fuel cell stack on load changes, thereby indicating that the model approach is appropriate.

5.1 Introduction

The transient response of a PEMFC stack to a load change of the power consumer is a complex phenomenon. A transient model has to account for the electrochemical reactions, the transport of water, and the gas components. Moreover, heat transport and charge transport are important processes in a fuel cell stack. The performance of a PEMFC stack depends on various operating conditions, such as the ambient temperature and the relative humidity of the gases, for example. Material parameters like the porosity and permeability of the GDL or the permeability of the membrane also influence the operating behavior of a PEMFC stack. Mathematical modeling and simulation is used to understand and handle this complexity.

As discussed in section 3.1 steady-state mathematical models of PEM fuel cells have been presented by several authors. However, steady-state models are not suitable for describing the dynamic behavior of a fuel cell stack. When operating, the stack is subject to load changes caused by the electric consumer. The development of optimized model-based control strategies requires a dynamic model that captures all important dynamic processes. In section 4.1, recent dynamic PEMFC models are discussed. Dynamic models that consider all important physical phenomena and couplings in a fuel cell are computationally expensive. Control applications usually require models that are fast to solve and numerically stable in a wide range of operating conditions. Up to now, these demands have not been met by models that contain a physically complete description of the phenomena in a PEMFC. Most control-oriented models are based on simplified versions of comprehensive fuel cell models. Often the dynamic couplings of the transport processes and the electrochemical reaction are partially neglected. Compared to the amount of work that has been published on the steady-state modeling of the PEMFC, few publications address the dynamic description of a PEMFC stack.

A control-oriented dynamic model of a fuel cell system for application in vehicles has been presented by Pukrushpan [81]. The voltage of the fuel cell stack is modeled on the basis of the load current and operating conditions, including cell temperature, air pressure, and oxygen partial pressure. To reduce the complexity of the model, the mass and energy balance and the electrochemical reactions are included in a lumped model of the fuel cell cathode only. For simplicity, the authors assume a fully humidified membrane. Golbert and Lewin [82] developed a transient along-the-channel model for control purposes. In their model only the energy balance of the solid is described dynamically, whereas all other equations are assumed to be at steady state for a given solid temperature. Amphlett et al. [83] used a similar approach that treats several transport phenomena in a quasi-stationary way. Natarajan et al. [84] developed a dynamic model of the cathode. A stack manifold model that accounts for the gas transport within the gas channels

and distributors was developed by Thirumalai and White [85]. Their model contains a description of the momentum and mass balance of a fuel cell stack. Other phenomena like the phase transition between water vapor and liquid water and a description of the membrane are neglected. The stack model presented in Ref. [86] applies an object-oriented approach. The gas flow, the produced heat, and the electrochemical performance are described in separate modules. The exchange of information between the modules is managed by a master program. However, the simulation results cover a time-span of only 10 minutes. In particular the heating and cooling of a fuel cell stack can require significantly more time and should be included in a stack model.
In this chapter, a dynamic fuel cell stack model is presented that contains several novel aspects. The model is based on the stationary single cell model of Yi [34]. In contrast to that work the stack model presented here includes the time-dependence of the mass and heat transfer and accounts for the whole stack. The mathematical description is formulated as a coupled DAE system. The dry-out of the membrane is an important phenomenon if a fuel cell stack is operated at high temperature or if dry gases are applied at the inlet. Accordingly, the stack model accounts for the coupling between the relative humidity of the cathode and anode side and the water content of the membranes. The water transport across the membrane in each cell is considered. The model simulates the behavior of a fuel cell stack for a duration of more than one hour under varying load. Validation measurements using a PEMFC stack are carried out and compared to the results of the stack model.

5.2 Model description

The PEM fuel cell stack model is dynamic and non-isothermal. Balance laws are used to describe the transport phenomena between the inlet and the outlet of the stack. Convective mass transfer and heat transfer by convection and conduction within the stack is accounted for. A mass balance of water in the liquid and vapor phase is included, accounting for the water transport through the membrane, condensation and evaporation in the channels, and water generation at the cathode. In addition, the dependencies of proton and water transport through the membrane on its water content is described by a membrane model according to Ref. [25]. An electrical model is included that allows for the calculation of the stack voltage for different current densities. It accounts for the influence of temperature changes and the voltage drop due to activation and ohmic losses. In section 5.3, the equations are set up for a single cell. The whole stack is described by several coupled cell modules. This approach allows the calculation of solution variables for each individual cell, thus offering the possibility of deriving stack temperature profiles and considering unequal fuel distribution in the cells.

The model geometry is illustrated in Fig. 5.1, which shows a part of a single-cell sandwich, including the bipolar plates. The gas channels usually have a meander shape. Since the model does not resolve the geometry of the gas channels, an effective channel length L_{eff} is introduced as indicated in Fig. 5.2. L_{eff} is a lumped parameter that describes the effective average length of the gas path, containing information about the geometry of the gas channels and the cross-diffusion of gas between adjacent channels.
The most important model assumptions are listed in the following:

- Gas in the channels can be described according to the ideal gas law.
- The gas channels are treated as plug-flow reactors. The total pressure along the channel is constant.
- The gas flow into the stack is homogeneously distributed among the cells and within each cell.
- The concentrations of the gases, the temperatures, and the solid temperature are assumed to change along the channel only. Variations in through-plane direction are neglected.
- The water transport in the gas channels is in form of water vapor only.
- Liquid water is assumed to exist as small droplets on the surface of the gas channels. As heat exchange with the solid material is much faster than with the gas, liquid water is assumed to have stack temperature. The volume of the liquid water is negligible.
- The membrane model neglects the pressure-driven transport of water.
- The diffusive mass transfer resistance of the gas diffusion layer and the catalyst layer is neglected.
- The current density is assumed to be constant throughout the stack. The inhomogeneity of the electric potential is neglected.

5.3 Model equations

The model equations are described in four subsections: energy and mass balance equations, an electrical model, and a membrane model.
The equations for energy and mass balance are formulated as classical balance laws based on the equation of continuity, i.e. Eq. (2.15) derived in Chapter 2. The

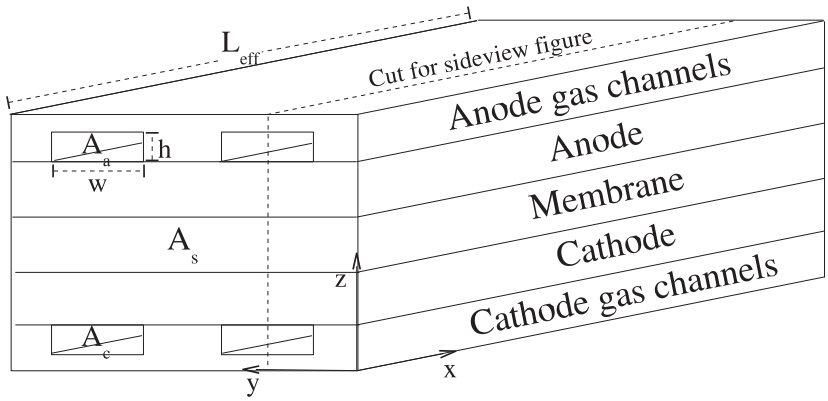

Figure 5.1: 3D view of the cell model, indicating the cross-sectional cell area A_s, the cross-sectional area of the gas channels of the anode A_a and of the cathode A_c, the effective channel length L_{eff}, and the cut for Fig. 5.2.

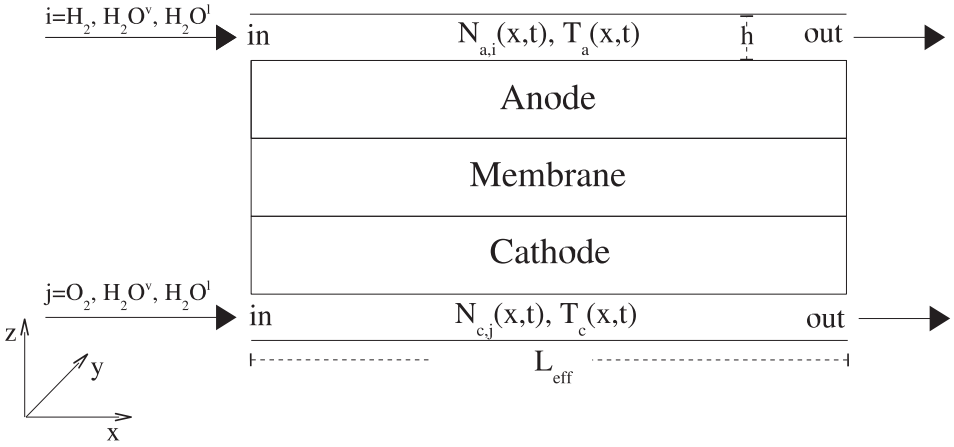

Figure 5.2: Sideview of the cell model along the cut indicated in Fig. 5.1, illustrating the direction of the molar flow $N_{a,i}$ of species i in the anode gas channel and the molar flow $N_{c,j}$ of species j in the cathode gas channel from the channel inlets to the channel outlets.

mass balance is set up for $H_2, O_2, N_2, H_2O^v, H_2O^l$. Energy balance equations are formulated for the gas channels of anode and cathode and for the solid material. Their basic form is given by Eq. (2.50) in Chapter 2. The different balance equations are described below in detail.

5.3.1 Energy balance

First, the energy balance of the gases is described. The considered species are $i = H_2, H_2O^v$ on the anode side and $i = O_2, N_2, H_2O^v$ on the cathode side. Liquid water is assumed to exist in form of small droplets at the surface of the channels. It is further assumed that the liquid water has stack temperature. The energy balance of the gas reads

$$\begin{aligned}\sum_i \partial_t \left[c_{q,i}(x,t) C_i T_q(x,t) A_q\right] = &-\sum_i \partial_x \left[N_{q,i}(x,t) C_i T_q(x,t)\right] \\ &+ A_{sg} U_{sg} \left[T_s(x,t) - T_q(x,t)\right] + \Delta H_{vap} \partial_x N_{q,H_2O^l}(x,t)\end{aligned} \tag{5.1}$$

where $c_{q,i}$ is the concentration of species i and $q = a, c$ denotes the anode side and the cathode side, respectively. $N_{q,i}$ is the molar flux of species i along the channel of electrode k. C_i denotes the heat capacity and T_q is the gas temperature. A_q is the cross-sectional area of the channel as indicated in Fig. 5.1, and A_{sg} is the heat-exchange area between channel and solid material. Furthermore, U_{sg} describes the heat transfer between the gas and the solid material. T_{sol} is the stack temperature and ΔH_{vap} is the enthalpy of evaporation of water. The term on the left-hand side of the equation describes the change of internal energy in a volume element. The terms on the right-hand side describe from left to right: the transfer of internal energy by convection, the heat transfer between the gas and the components of the stack, and the heat consumption or production due to evaporation and condensation of water.
The energy balance equation of the solid material links the processes in the gas channels of the anode side and the cathode side. It is given by

$$\begin{aligned}\rho_s C_s A_s \partial_t T_{sol}(x,t) = &\, A_s k_s \partial_x^2 T_{sol}(x,t) \\ &- n_{chan} \partial_x \left(\left[N_{a,H_2O^l}(x,t) + N_{c,H_2O^l}(x,t)\right] C_{H_2O^l} T_{sol}(x,t) \right) \\ &+ n_{chan} A_{sg} U_{sg} \left[T_a(x,t) + T_c(x,t) - 2T_{sol}(x,t)\right] + A_{ss} U_{ss} \left[T_{sur}(x) - T_{sol}(x,t)\right] \\ &- n_{chan} \Delta H_{vap} \left[\partial_x N_{a,H_2O^l}(x,t) + \partial_x N_{c,H_2O^l}(x,t)\right] \\ &- n_{chan} d_y w \left[\left(\frac{\Delta S_a}{2F} + \frac{\Delta S_c}{4F} \right) \left(T_{sol}(x,t) + 273\right) - \eta_c(x,t) \right] I(x,t) \,,\end{aligned} \tag{5.2}$$

where ρ_s is the density of the solid material, C_s is its heat capacity, and A_s is the cross-sectional area of a single cell in the stack (see Fig. 5.1). k_s denotes the

heat conduction coefficient, n_{chan} is the number of channels in one cell, and A_{ss} is the heat exchange area between the stack and its surroundings. Furthermore, U_{ss} is the heat transfer coefficient and T_{sur} denotes the ambient temperature. d_y is a scaling coefficient, which takes into account the enlargement of the contact area between the gas and the porous catalyst layer due to the cross-diffusion under the flow-field bridges. The width of a gas channel is denoted as w and ΔS_q is the entropy of reaction in electrode q. Finally, F is the Faraday constant, η_c is the activation overpotential of the oxygen reduction reaction, and I denotes the current density. The change of internal energy in a volume element of the solid stack material, which is described by the term on the left-hand side, is given by the following source and sink terms on the right-hand side of the equation: (a) Heat conduction driven by a temperature gradient within the stack; (b) heat transferred by convection of liquid water; (c) heat transfer between bulk material and gases of anode and cathode sides; (d) heat transfer between bulk material and surroundings; (e) heat generation and consumption due to condensation or evaporation of water in anode or cathode; (f) heat generation due to the reaction entropy and dissipation. As a cell contains several channels, the terms b, c, e, and f are multiplied by the number of channels n_{chan}.

5.3.2 Mass balance

For the mass balances the convective transport along the channel, the fuel consumption of H_2 and O_2, the production of H_2O^v at the cathode, the phase transition of water, and the transport of water vapor through the membrane are taken into account. Below, the mass balance equations for the species on the cathode side are given. The corresponding equations for the anode side are analogous.
The mass balance equation of oxygen in the cathode is

$$\partial_t \left[c_{c,O_2}(x,t)A_q\right] = -\partial_x \left[N_{c,O_2}(x,t)\right] - \frac{d_y w I(x,t)}{4F} \,. \tag{5.3}$$

The concentration of oxygen changes due to the convective transport along the channel and the consumption of oxygen at the cathode.
The mass balance equation for water vapor in the cathode is given by

$$\begin{aligned}\partial_t \left[c_{c,H_2O^v}(x,t)A_q\right] &= -\partial_x \left[N_{c,H_2O^v}(x,t)\right] \\ -\partial_x \left[N_{c,H_2O^l}(x,t)\right] &+ \frac{d_y w I(x,t)}{2F} + \frac{d_y w \alpha_{net} I(x,t)}{F} \,.\end{aligned} \tag{5.4}$$

The change in the concentration of water vapor is balanced by the convective transport of water vapor and convection of liquid water. Moreover, the production of water in the electrochemical reaction and the net-transport of water through

the membrane are taken into account. The net-migration coefficient α_{net} is the number of water molecules per proton that is transported through the membrane. It can be positive or negative, depending on the direction of the net-water flux. The mass balance equation for liquid water in the cathode is

$$\begin{aligned}\partial_t \left[c_{c,H_2O^l}(x,t)A_q\right] &= -\partial_x \left[N_{c,H_2O^l}(x,t)\right] \\ &+ \frac{k_c wh}{RT_c(x,t)} \left(p_{H_2O^v}(x,t) - P_{sat}(\overline{T_c})\right) \ , \end{aligned} \tag{5.5}$$

where k_c is the condensation rate constant and h is the channel height. R denotes the ideal gas constant, $p_{H_2O^v}$ is the partial pressure of water vapor in the cathode gas channel, and P_{sat} is the saturation pressure. The concentration of liquid water changes due to convective transport of liquid water along the channel and the phase transition of water.

5.3.3 Electrical model

The electrical model is similar to the model developed by Golbert et al. [82]. The cell potential is calculated from the following equation

$$V_{cell} = V_{oc} - \frac{RT_{sol}}{0.5F} ln\left(\frac{I(t)}{i_{0,c}\ a_{O_2}}\right) - \frac{I(t)t_m}{\sigma_m(x,T,\lambda_m(z,t))} \ , \tag{5.6}$$

where V_{oc} is the open circuit voltage and a_{O_2} denotes the activity of oxygen in the cathode. The exchange current density is denoted as $i_{0,c}$. The membrane is described by its thickness t_m and its conductivity σ_m. The cell potential V_{cell} is given by the open circuit voltage, which is reduced by the considered losses. The second term on the right-hand side of Eq. (5.6) describes the activation overpotential of the oxygen reduction reaction. The third term describes the ohmic losses due to the limited membrane conductivity.

5.3.4 Membrane model

The transport of water through the membrane is assumed to be a superposition of the electro-osmotic drag and the diffusion due to a concentration gradient across the membrane. The net-migration coefficient of water through the membrane α is modeled as described in Ref. [82]:

$$\begin{aligned}\alpha_{net} = n_{drag} &- \frac{F}{I} D_{m,H_2O} \frac{c_{c,H_2O^v} - c_{a,H_2O^v}}{t_m} \\ &- \frac{c_{c,H_2O^v} + c_{a,H_2O^v}}{2} \frac{k_{m,p}F}{\mu_l I} \frac{p_{c,H_2O^v} - p_{a,H_2O^v}}{t_m}, \end{aligned} \tag{5.7}$$

where n_{drag} is the electro-osmotic drag coefficient describing the number of water molecules carried through the membrane for each proton. D_{m,H_2O} is the diffusion coefficient of water in the membrane, $k_{m,p}$ the water permeability, and μ_l the viscosity of water. Three transport mechanisms are considered in the equation above. The first term on the right-hand side describes the transport of water by electro-osmotic drag. The second and third terms describe the diffusion due to a concentration and a pressure gradient in the gas phase. The dependency of the membrane water content λ_m on the water vapor activity a_q at the membrane interface is modeled by the following equations [25]

$$\lambda_m = \begin{cases} \left(0.043 + 17.8a_q - 39.85a_q^2 + 36a_q^3\right) & for \quad a_q \leq 1 \\ \left(14 + 1.4\left(a_q - 1\right)\right) & for \quad a_q > 1 \end{cases} . \tag{5.8}$$

The membrane conductivity σ_m depends on the membrane water content λ_m. To account for this dependency, the membrane water content is calculated in each time-step according to

$$\sigma_m = (0.00514\lambda_m - 0.00326) exp\left(1268\left(\frac{1}{T_{ref}} - \frac{1}{T_{sol}}\right)\right) . \tag{5.9}$$

The supporting equations that are needed to complete the DAE system are given in the appendix of the thesis.

5.4 Discretization and solution method

For the model validation the solution variables should be experimentally accessible. Accordingly, two reference points are defined. These are the inlet and the outlet of the fuel cell stack. At both points the gas temperatures and the molar flows of the different species are considered. The parameters at the channel inlets serve as boundary conditions for the model. Furthermore, the current density is a time-dependent input parameter. Hence, based on the operating conditions, the model calculates the molar fluxes and temperatures at the channel outlets, the average temperature of the solid material, and the stack voltage. Only one cell module is calculated numerically. The results are extrapolated to take several cells in the stack into account. Accordingly, it is assumed that each cell in the stack works identically. Fig. 5.4 provides an overview of the input and output variables of the model and illustrates how the variables are adapted from the stack to the cell model. To derive appropriate and rapidly computable equations, the DAE system described above is integrated along the channel length. Using the divergence theorem and the mean value theorem, ODEs in time are derived from the PDEs which are discretized to the two points under consideration, the inlet and outlet of

the channels. The model is implemented in MATLAB^{TM} using the provided ODE solver environment. The implicit solver ode15s is used for the time discretization. The ode15s is a variable-order multistep solver based on the numerical differentiation formulas. The time-steps and the formulas change dynamically. During tests with different current density profiles the model showed stable convergence behavior, thus indicating that the model is applicable to a wide range of different operating conditions and load profiles.

5.5 Parameter identification

The mathematical model contains several constants and parameters, which can be broken down into stack-dependent geometrical, electrochemical, and physical parameters as well as stack-independent physical constants. The majority of the parameters was determined by literature research. A thorough literature study was performed to determine reasonable ranges for all parameters. The geometrical stack dimensions and the operating and boundary conditions are measurement values. The list of parameters and references is given in Tables Ia to Id.

5.6 Results and discussion

Fig. 5.5 to Fig. 5.10 show simulation results for a current step profile. The stack current is increased in steps of 50 mA/cm^2 up to 300 mA/cm^2 and subsequently reduced analogously. This procedure elucidates the behavior of the fuel cell stack upon a step change in the load, as frequently encountered in practical applications. The computing time is 0.8 seconds on a workstation with an AMD Athlon 1533 MHz processor for a simulated time-span of 75 minutes. Thus, the model is computationally efficient and suitable for control applications.
The results of Fig. 5.5 show the typical behavior of a stack subjected to a current step profile. With increasing current density the stack voltage decreases and vice versa. According to Faradays law, higher current density is linked to higher fuel consumption. Thus, the molar flows of hydrogen and oxygen out of the stack decrease with increasing current density. This effect is illustrated in Fig. 5.6. On the other hand, the production rate of water increases with the current density, as can be seen in Fig. 5.7. The molar flux of water vapor at the outlet of the cathode side increases and decreases with the current density. Due to the diffusion of water through the membrane, the amount of water at the anode side also increases.
However, at higher current density the electro-osmotic drag of water from the anode side to the cathode side becomes important. This phenomenon is the main reason for the difference between the flow rates of water vapor at the anode and

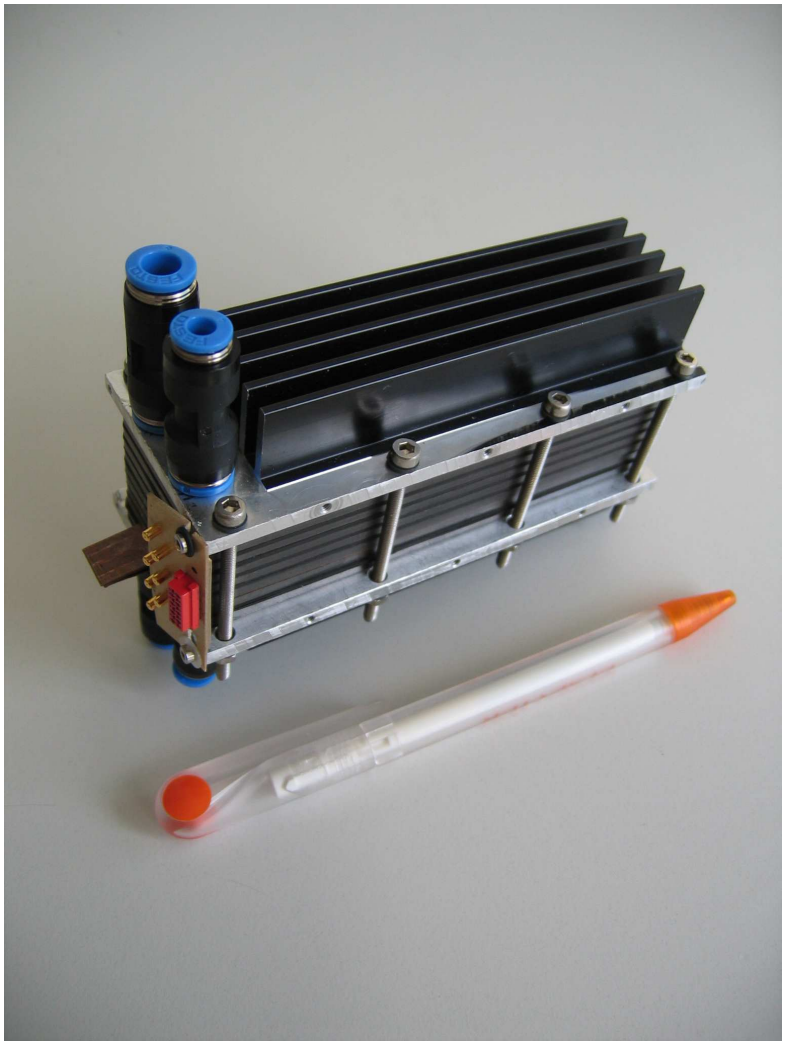

Figure 5.3: The picture shows the PEMFC stack that was used for the validation measurements. The nominal power output of the stack is 30 W. The peak power is as much as 70 W, depending on the operation conditions. The blue features are the gas inlet and outlet, respectively. The gray layers between the stainless steel plates are the bipolar plates and the sealings of the cells. The stack temperature is reduced by cooling ribs on the surface of the stainless steel endplates. The screws apply the pressure to seal the stack and reduce the contact resistance between adjacent layers.

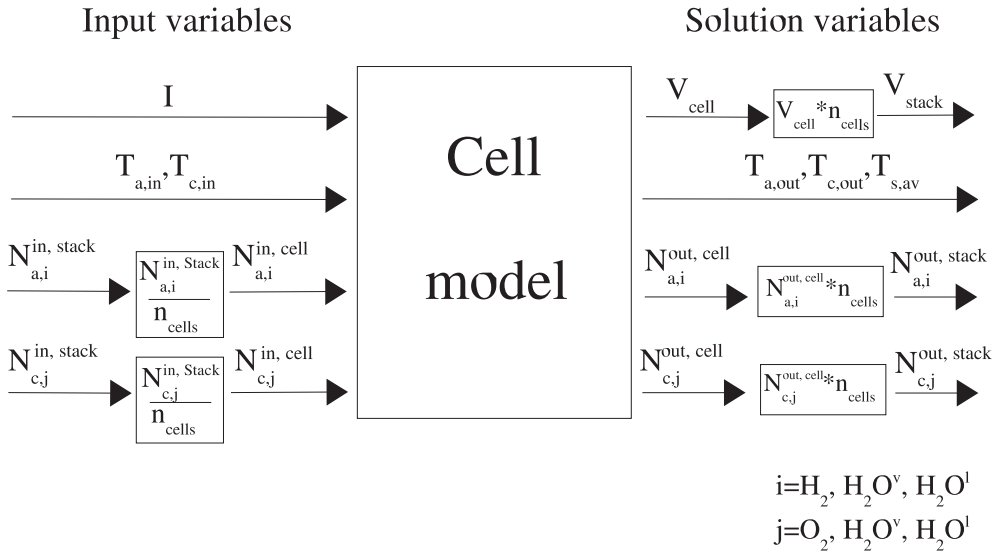

Figure 5.4: An overview of the input and solution variables is shown. The stack model is obtained from the cell model by division or multiplication, respectively by the number of cells n_{cells}.

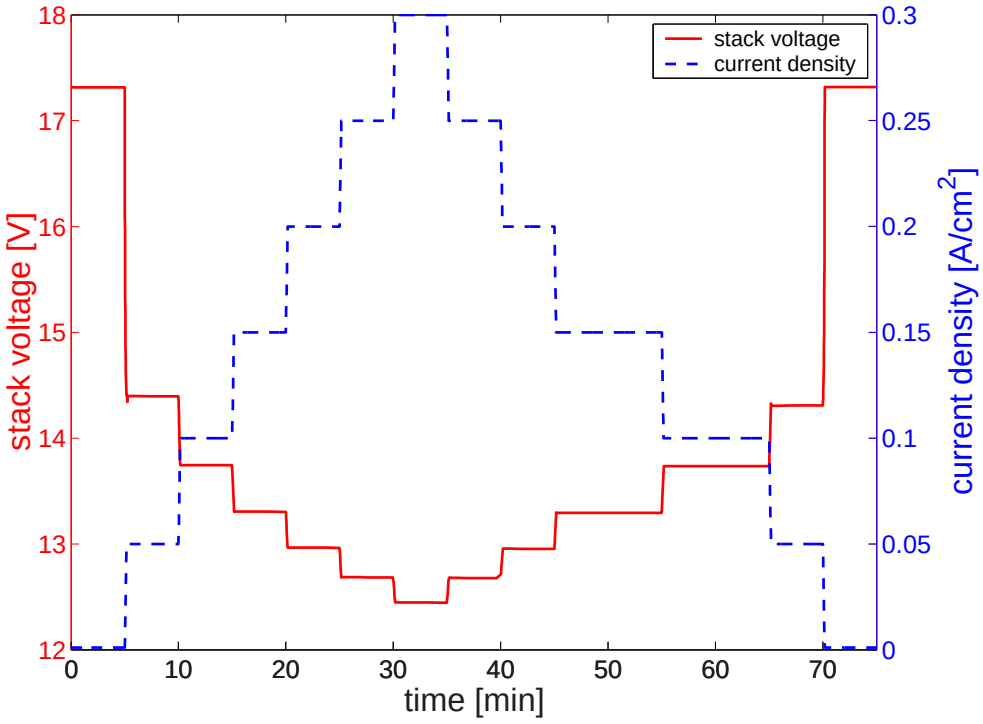

Figure 5.5: The stack model is applied to simulate the application of a current step profile indicated by blue. The resulting stack voltage is calculated and indicated by red. Upon an increases of the current density the voltage of the fuel cell stack decreases. The magnitude of the voltage steps is governed by the Tafel equation. Hence, a small change in the current density at low stack voltage leads to a large change in the stack voltage. At higher current density the change of the stack voltage is less pronounced.

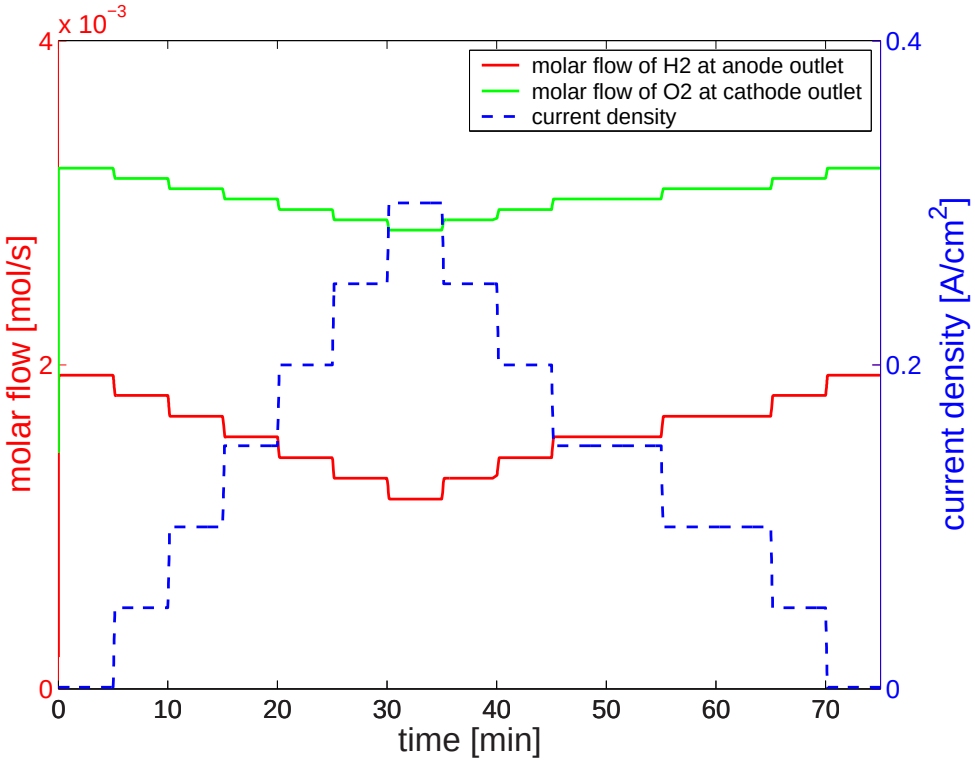

Figure 5.6: This graph shows the simulated evolution of the oxygen and hydrogen flux at the stack outlet. The concentration of the fuel gases at the outlet decreases with increasing current density. The species are consumed in the fuel cell stack in accordance with Faraday's law.

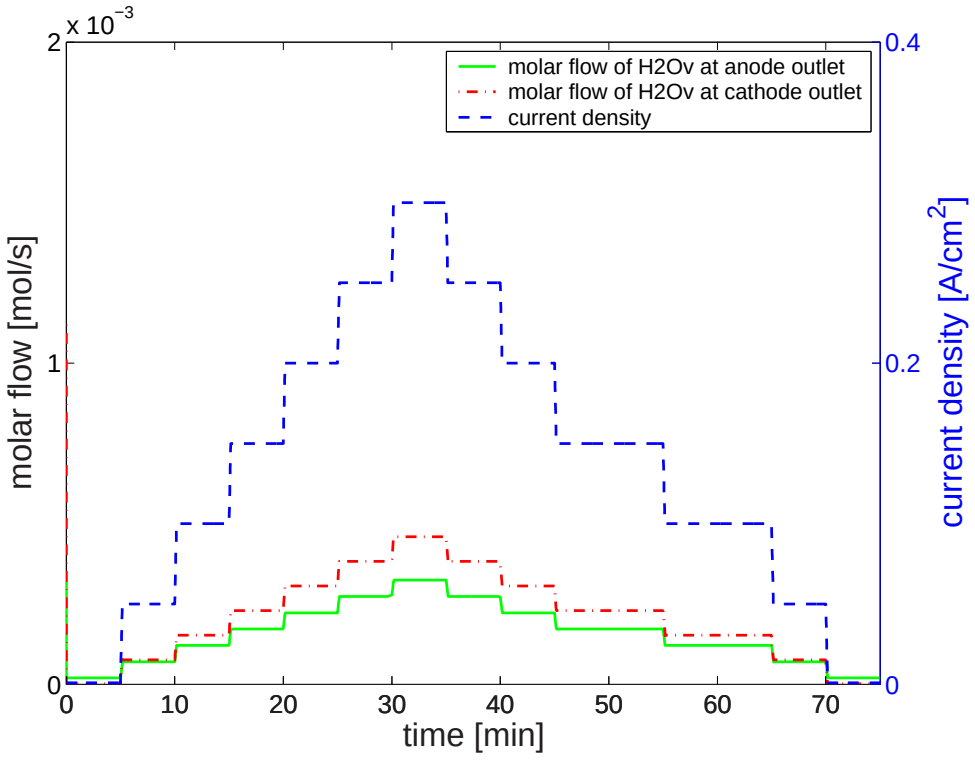

Figure 5.7: The molar flux of water vapor at the cathode outlet is indicated by red. Part of the water generated at the cathode diffuses through the membrane to the anode side. Accordingly, at the outlet of the anode side the molar flux of water vapor increases with increasing current density, too. However, at high current density more water is removed via the cathode due to the electro-osmotic drag from anode side to cathode side.

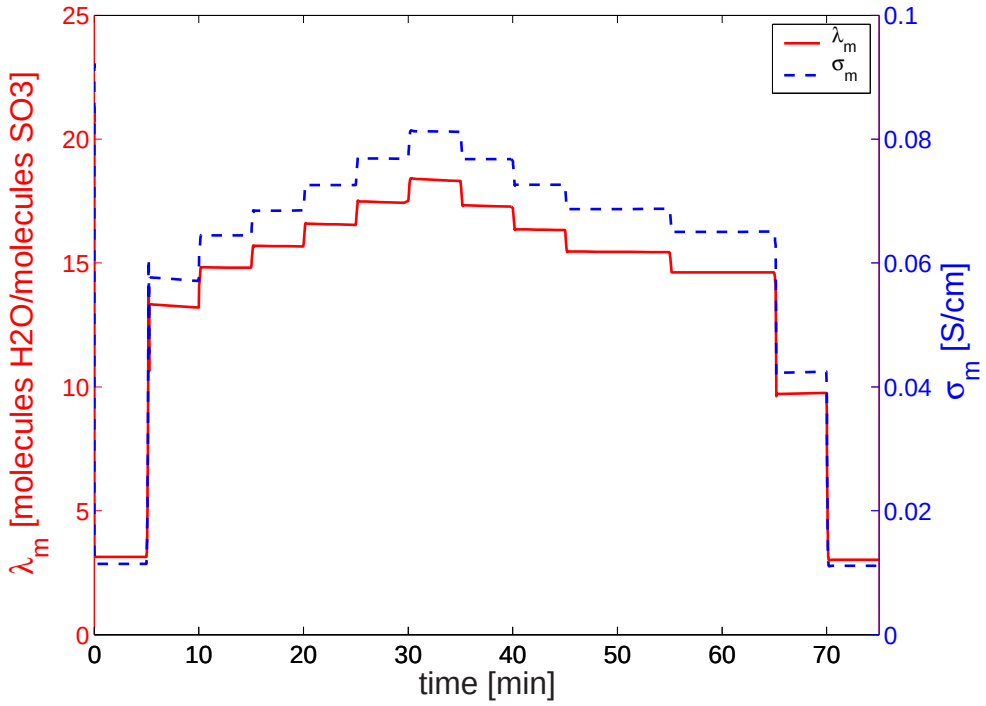

Figure 5.8: This graph shows the water content λ_m and the conductivity σ_m of the polymer membrane of a single cell within the stack. The water content is determined by the activity of water vapor in the gas channels of the electrodes. According to Fig. 5.7, the molar flux of water vapor at the stack outlets increases with increasing current density. Hence, the relative humidity increases, which leads to a higher membrane water content λ_m and a higher protonic conductivity σ_m.

cathode outlets at the highest current density in Fig. 5.7. The water content of the membrane λ_m is determined by the relative humidity of the gases in the electrode compartments. Fig. 5.8 shows the water content, i.e. the number of water molecules per sulfonic acid group of the membrane. Fig. 5.7 indicated that the humidity in the gas channels of cathode and anode side increases with increasing current density. Accordingly, in Fig. 5.8 an increase of the membrane water content λ_m with increasing current density can be seen. Since the protonic conductivity σ_m improves as the membrane becomes more humid, σ_m shows the same trend as λ_m.

The most important heat source at small and medium current density with sufficient membrane conductivity is the waste heat production of the oxygen reduction reaction. The heat generation due to the electrochemical reaction is proportional to the current density. The temperature of the stack is indicated by gray in Fig. 5.9.

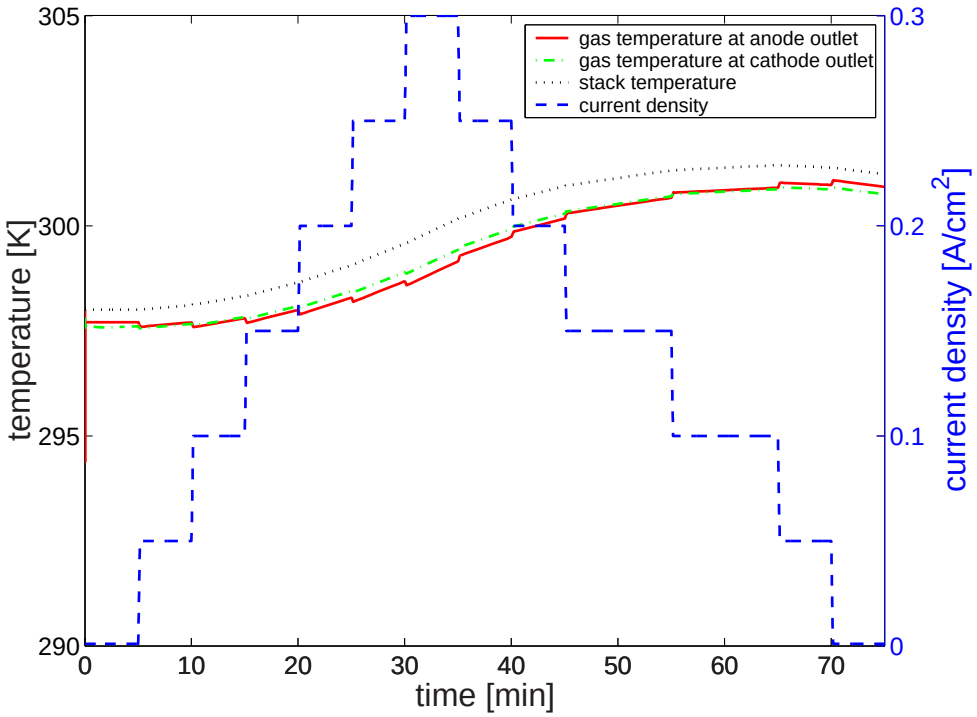

Figure 5.9: The stack temperature is indicated by gray. It is delayed with respect to the heat production within the stack which is mainly determined by the current density. The delay is due to the comparatively large mass and heat capacity of the solid stack components. The temperature of the gases at the outlet of cathode and anode is governed by the evolution of the stack temperature. The gases heat up during their transition through the stack.

A time delay between the maximum current density and the maximum stack temperature occurs. The time-span between the highest current density and the peak temperature is governed by the mass and heat capacity of the solid stack components. The temperature of the gases at the outlets of anode and cathode is coupled with the stack temperature. On their passage through the stack the gases tend to heat up.

The electrical part of the model yields the stack voltage by subtracting the activation losses and the ohmic losses from the open circuit voltage. The evolution of the loss-terms is depicted in Fig. 5.10. The activation loss of the oxygen reduction reaction is the most important loss mechanism at small and medium current density. The ohmic loss is due to the limited protonic conductivity of the membrane. In the specific case that is simulated here, the humidity of the membrane and, hence, the conductivity is sufficient. Accordingly, the ohmic loss does not

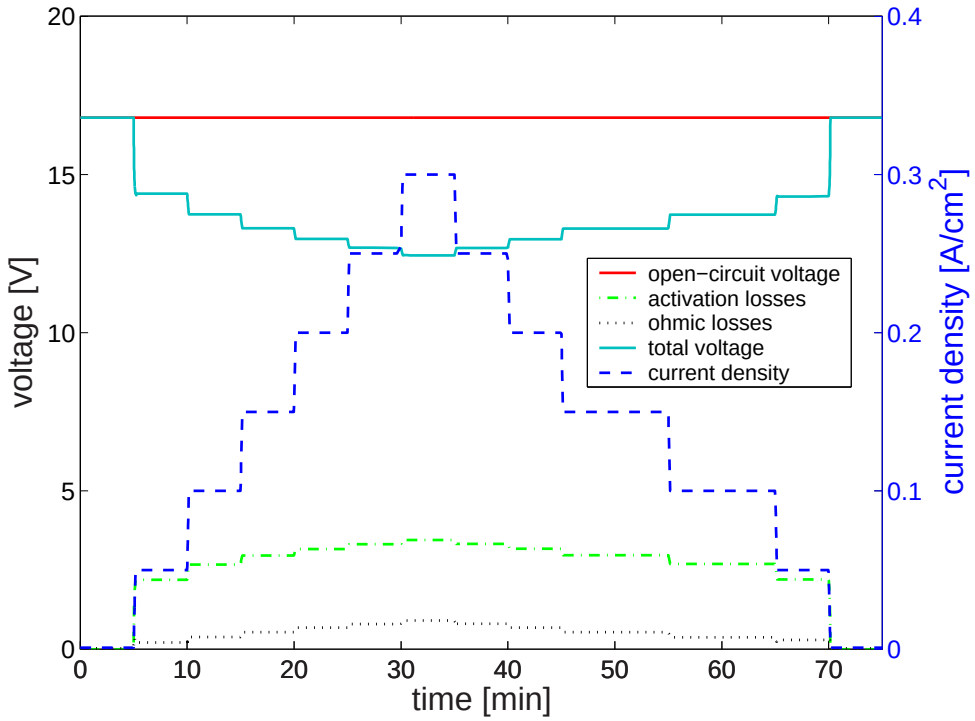

Figure 5.10: This graph shows the time-dependent evolution of the ohmic and activation losses in the fuel cell stack. The stack consists of 14 cells. The activation losses that are due to the oxygen reduction reaction are the most important loss mechanism at small and medium current density. They are indicated by green. The ohmic losses account for a minor part of the voltage drop since the humidification of the membrane is excellent in this case. The resulting stack voltage is indicated by light blue.

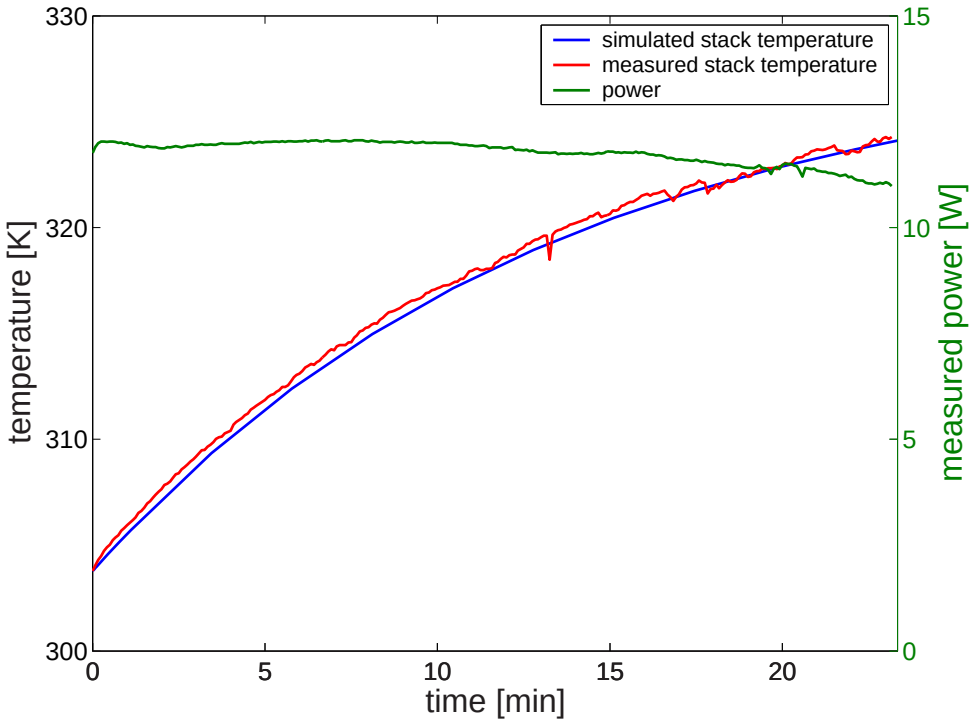

Figure 5.11: Monitoring the stack temperature is most important for the operational control of a fuel cell stack. The temperature is coupled with all phenomena that occur in a stack. For example, the electrochemical reactions and the conductivity of the membrane depend on the temperature. The graph shows excellent agreement between the measured temperature evolution and the simulated stack temperature. In the case shown here, the stack was operated at constant load.

account for a large part of the voltage drop inside the fuel cell stack.
Fig. 5.11 shows a comparison of the measured and the simulated stack temperature. The PEMFC stack that was used for the validation measurements is shown in Fig. 5.3. The stack has a nominal power of 30 W and a peak power of up to 70 W. The magnitude of the peak power depends on the operating conditions, such as the stack temperature and the humidification state, and can be maintained for a duration of several minutes. Due to its small size it is suitable for portable applications. The stack that is shown in Fig. 5.3 was operated at constant load, and the temperature evolution was recorded. Moreover, in Fig. 5.12 simulated and measured stack voltage are compared for a step-profile in the current density. The simulated stack voltage shows good agreement with the results of the measurement. The deviations between simulated and measured values are due to the occurrence of liquid water in the PEMFC stack. The generation and transport of

liquid water is not included so as to reduce the complexity of the model. This improves the numerical stability and allows for a fast solution of the equations. Until the highest current density is reached, the temperature of the stack is low enough to allow for the generation and accumulation of liquid water. Hence, the protonic conductivity of the MEA increases and leads to an increase of the stack voltage during each current step. When the current density is decreased the stack is still heating up. Eventually, this causes the MEA to dry out and the stack voltage to decrease during each step. The agreement of the simulation results with the measurements indicates that the model approach is appropriate for dynamic fuel cell stack simulation.
The model not only facilitates the simulation of the stack operation for long timespans, but also yields information about the short-time dynamic behavior. For example, Fig. 5.13 shows a step in the current density from 100 mA/cm^2 to 300 mA/cm^2. For numerical reasons the step is approximated by a short ramp of 0.5 s in the current density. The resulting stack voltage that is indicated by the red line decreases upon the increase of the current density. The trend of the stack voltage points to a time-dependent process other than the change of the current density which has an influence on the stack performance. In Fig. 5.14 the evolution of the molar flux of water vapor at the stack outlet as a result of the current ramp is shown. The red line indicates the cathode outlet, and the green line is the molar flux of water vapor at the anode outlet. Due to the increase of the current density the generation of water within the stack increases in accordance with Faraday's law. However, the increase of the water vapor flux at the anode side is delayed with respect to the current density. The water vapor flux at the outlet is an indicator of the relative humidity in the gas channels of the anode side. The relative humidity at both the anode and the cathode side determines the average water content of the membrane. Accordingly, the membrane water content, and thus the conductivity of the membrane, increase delayed with respect to the current density. This results in the trend of the stack voltage that is shown in Fig. 5.13.

5.7 Conclusion and outlook

An analysis of the dynamic behavior of a PEMFC stack is given based on a novel stack model. The mathematical formulation of the stack model is a coupled differential algebraic equation system. Ordinary differential equations in time describe the transport phenomena, and the oxygen reduction at the cathode is modeled by an algebraic relation. The model is physically detailed and considers the important couplings among the transport phenomena and the electrochemical reaction. At the same time, the model is computationally efficient.
The realistic simulation results show that the modeling approach is appropriate for

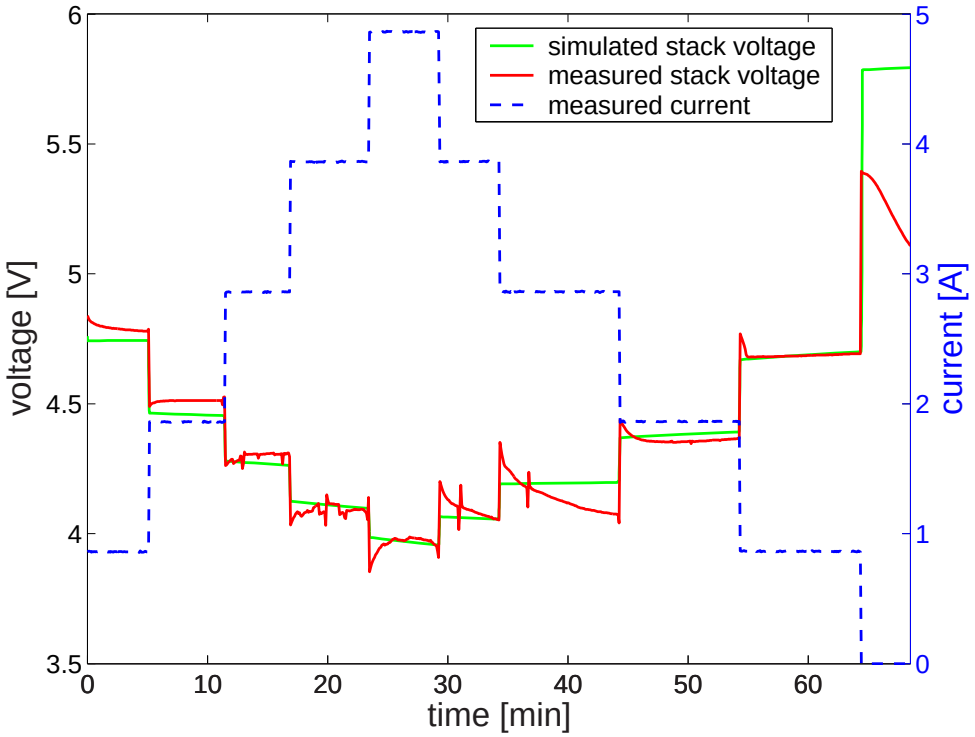

Figure 5.12: Comparison of simulated and measured stack voltage. The simulated stack voltage shows good agreement with the results of the measurement. The deviations between simulated and measured values are due to the occurrence of liquid water in the PEMFC stack. Until the highest current density is reached, the temperature of the stack is low enough to allow for the generation and accumulation of liquid water. Hence, the protonic conductivity of the MEA increases and leads to an increase of the stack voltage during each current step. When the current density is decreased the stack is still heating up. Eventually, this causes the MEA to dry out and the stack voltage to decrease during each step.

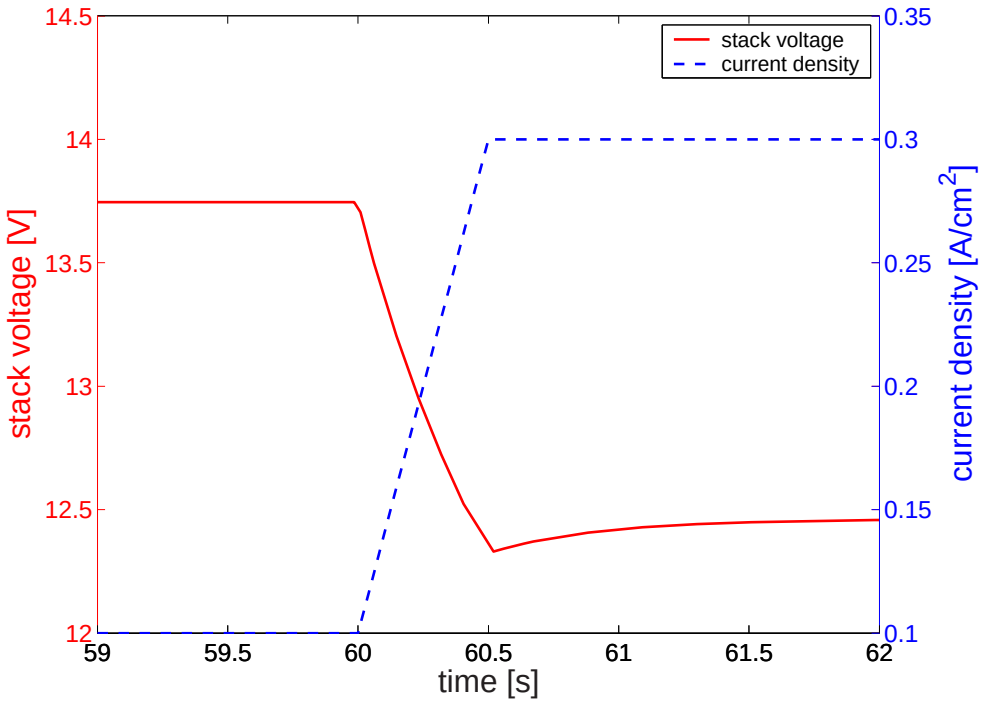

Figure 5.13: Simulation of a step in the current density on a short time scale. Using a high time-resolution it becomes evident that the stack voltage does not follow instantaneously upon a change in the current density. The stack voltage reaches a minimum value and subsequently relaxes to the new equilibrium value. This behavior is explained in Fig. 5.14

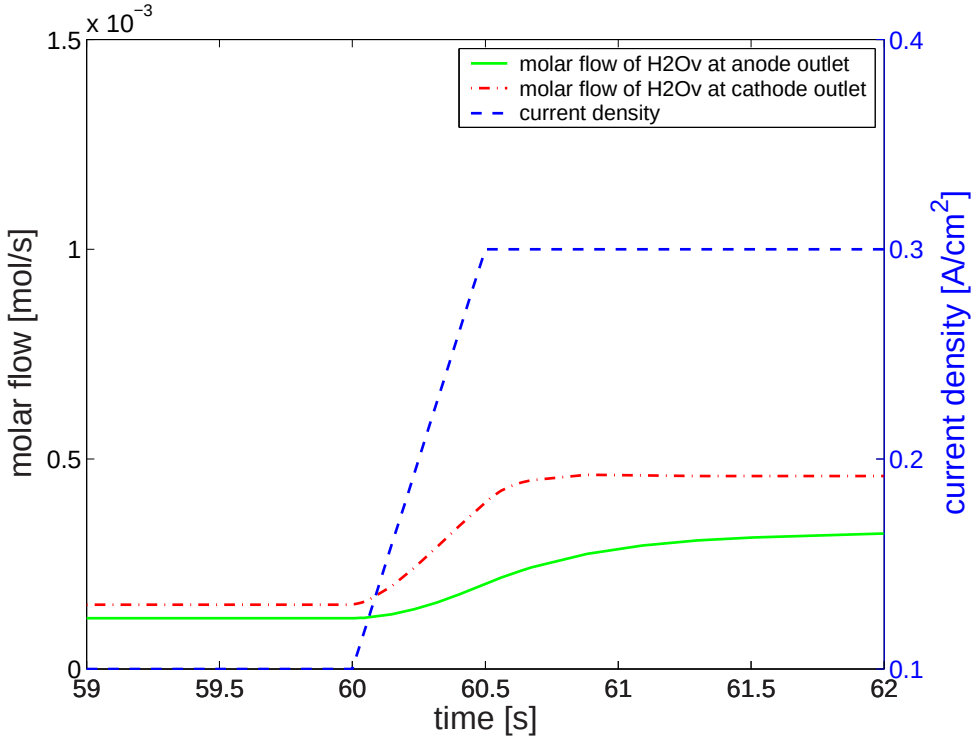

Figure 5.14: The same current step as in Fig. 5.13 is shown. The red and green curves indicate the molar flux of water vapor at the outlet of the cathode and the anode side, respectively. The humidity of both the anode and the cathode off-gas increases due to the increased generation rate of water vapor at higher current density. The humidity of the anode off-gas is delayed with respect to the step change of the current density. The water that is generated at the cathode side has to be transferred to the anode gas channels via the membrane. The water vapor concentration of both the anode and the cathode side influence the water content of the membrane. Thus, the protonic conductivity and, hence, the stack voltage increase delayed with respect to the step change of the current density.

the dynamic description of a PEMFC stack. The model can predict the stack voltage and the molar fluxes of hydrogen, oxygen, and water vapor given an arbitrary load profile. Moreover, the temperature of the off-gas and of the stack itself is calculated. The stack temperature is coupled with all other phenomena that occur in a fuel cell stack. For example, the protonic conductivity is treated as a function of the temperature, and its evolution is calculated.

A thorough understanding of the dynamic response of a PEMFC stack is crucial for the operation control of integrated fuel cell systems. The stack model is suitable for control applications, since the convergence behavior is excellent, as shown by the simulation of a current-step-profile. This model property allows one to examine a wide parameter range and to simulate different operating scenarios. Moreover, the model is computationally efficient. In a computing time of less than one second the dynamic response of the stack to varying load can be predicted for an operation time of more than one hour.

The model is validated by the comparison of the simulated and the measured stack temperature. A PEMFC stack constructed for use in portable applications was operated under constant load. The input parameters of the model were controlled by the software of the test stand. The simulation results agree with the results of the measurement.

The identification of the dominant time-dependent physical processes under changing load conditions and for different operating regimes is a capability of the stack model. For example the influence of the humidity of the inlet gases, or the heat flux that should be removed via the surface of the stack, can be simulated. By integrating the stack model into a system simulation environment, it can be utilized to study the dynamic interaction between the fuel cell stack and its peripheral components like pumps, fans, and valves. From the results of such a study guidelines for the optimization of fuel cell systems can be derived. The most important application is the model-based development of a control algorithm. Currently, the control of fuel cell systems is usually managed by algorithms that are based on empirical observations and practical experience. By developing a control scheme that is based on a physical fuel cell stack model the performance of fuel cell systems can be improved.

Chapter 6

Summary of Results and Conclusion

This chapter summarizes the most important results of this thesis. In addition, an outline is given of potential research issues in each field covered by the thesis.

6.1 Planar self-breathing fuel cells

Model concept and validation

In Chapter 3 a novel non-isothermal two-dimensional model of a planar and self-breathing fuel cell was presented. Migration of electrons and protons, multicomponent diffusion of the gaseous species according to Maxwell-Stefan, and diffusion and electro-osmotic drag of water across the membrane are considered in the mathematical description. The protonic conductivity of the membrane is included as a function of temperature and membrane water content. An agglomerate model is derived to take the microstructure of the electrodes into account. The heat transfer equation is solved, including the effects of resistive heating, reaction entropy, and heat losses to the surroundings. The model is validated by comparison of simulation results with experimental values. The reference cell used for the validation is a planar self-breathing fuel cell in PCB technology. The agreement between the predictions of the model and the measured overall cell performance is excellent.

Operating behavior and design guidelines

In general, the performance of the planar self-breathing fuel cell is determined by the competing effects of charge transfer and mass transfer. The most important factors are the conductivity of the membrane and the ionomer in the cathode catalyst layer. In current fuel cells this conductivity decreases rapidly if the relative humidity in the porous electrodes decreases. This effect limits the rate of the elec-

trochemical reactions, in particular at the cathode side, and leads to non-uniform activity of the catalyst layer in the through-plane direction, that is, perpendicular to the membrane. A higher conductivity at moderate relative humidity that avoids condensation of water would increase the performance substantially.
The design of the cathode influences the performance of the cell in several ways. The ribs in the cathode end-plate affect the potential distribution, resulting in a charge generation rate that is highest close to the ribs. The oxygen concentration is lowest under the middle of the ribs, thus reducing the charge generation rate in this region of the catalyst layer. Both, access to the oxygen supply and access to the electron supply, are important for efficient use of the catalyst layers. The fuel cell design studied in the base case leads to a charge generation rate that is best close to the edges of the ribs in the cathode end-plate. The rib is an obstacle for the diffusive outflux of the product water. Liquid water is expected to form under the rib first. In the cathode, the supply of electrons to the active regions between the ribs causes a strong non-uniformity in the current density distribution. Close to the ribs in the gas diffusion layer the current density is an order of magnitude higher than the average current density of the cell. This causes increased resistive heating in that part of the fuel cell.
However, the temperature distribution of the planar self-breathing fuel cell is governed by two other effects. The main source of heat is located in the active area of the cathode, leading to an increased temperature in the center of the cell sandwich. The ribs in the cathode act like cooling fins that remove the heat from the center of the cell. This results in a temperature that is lower underneath the ribs than in the areas between the ribs. The overall temperature difference in this type of cell is small, only about 1 K at an average current density of about 300 mA/cm^2. This is a result of the high surface-to-volume ratio, which allows for efficient heat removal mainly by free convection from the fuel cell to the surroundings. However, higher power densities can be reached using the concept of planar fuel cells. With increasing power density, resistive heating and the heat generated by the electrochemical reaction limit the cell performance.
At low current density, the mass transfer limitation is small and the use of wide ribs and thin gas diffusion layers is preferable. In the high current density regime, the ribs should be thin to reduce the mass transfer limitation. The lateral mass transfer resistance can be reduced further by a high effective lateral diffusivity. However, the lateral conductivity of the gas diffusion layer should be excellent to avoid significant charge transfer limitations between the ribs.

Future issues in validation and coupled modeling of PEMFCs

Fuel cell models are commonly validated by comparison with experimental results like the current-voltage characteristic or the impedance spectrum of a fuel

cell. When comparing simulation results with measurements there are some issues that need careful consideration.

To date, fuel cells are usually hand made and deviations in the behavior of cells with identical design are observed. Provided that the components like the membrane electrode assembly and the gas diffusion layer have constant properties, the main reason for this is the inability to apply the external mechanical pressure perfectly homogeneously. If the end-plates of the fuel cell are held together by screws, the overall electrical contact resistance can be controlled by measuring the ohmic resistance during the tightening of the screws. Similarly, one can assume that the overall thermal contact resistance due to the heat conduction from layer to layer can be reproduced. However, the distribution of the mechanical pressure might vary even if the overall resistance is unchanged. The inhomogeneity of the electrical and thermal contact resistance affects the potential and temperature distribution of the fuel cell and, hence, changes the operating behavior. High precision sealings are required in order to ensure a homogeneous and reproducible mechanical pressure distribution. For planar fuel cells the use of glue is an option for assembling the end-plates. The development of advanced gluing techniques is necessary to achieve reproducibility with respect to the mechanical pressure distribution inside the cell.

Associated with the mechanical pressure distribution is the issue of the deformation modulus of the components. The GDL is the most important component with respect to the deformation. Due to the external pressure, the ex-situ properties of the gas diffusion layer are altered. The pore size distribution, the porosity, and the permeability of a GDL change upon compression. The dependence of these variables on compression needs to be determined. This is important since these properties of the GDL can have a strong influence on the distribution of the gases and the liquid water inside a fuel cell.

Moreover, absolute permeability is usually treated as a scalar quantity. From TEM pictures it is known that common GDLs have highly anisotropic geometric features. Hence, the determination of the full permeability tensor is required. Similarly, the electrical and thermal conductivity of the components should be treated as three-dimensional tensors. Calculations based on the Lattice Boltzmann method using a geometric domain that resolves the microstructure of the GDL can be applied to determine the required quantities. Additionally, the in-plane and through-plane properties of the GDL can be measured using sophisticated ex-situ measurement techniques.

To improve the modeling of the fuel cell components, future models should contain the full electrical and thermal conductivity tensors and the absolute permeability tensor, including a parametrization with respect to the deformation of the material. The deformation can be calculated by using a mechanical model that considers the applied pressure and the deformation modulus of the components.

6.2 Two-phase dynamic modeling of PEMFCs

Model concept, validation, and behavior of PEMFCs in the two-phase flow regime

In Chapter 4, a dynamic model of a proton exchange membrane fuel cell has been developed. The model contains a description of the gas diffusion layers, the catalyst layers, and the membrane. The phase transition between water vapor and liquid water is considered. The model accounts for the transport of the gaseous species and the transport of liquid water. Furthermore, the charge transport and the electrochemical reactions are considered. The couplings between the different processes are included in the model. The model is one-dimensional and isothermal.

During the operation of the fuel cell, the product water accumulates in the GDLs and the porous electrodes. This process influences the transport of the fuel gases. The result is a current-voltage characteristic that is not stationary but dynamic. Most PEMFC models that can be found in the literature are based on a stationary description. However, a stationary model does not explain the experimentally observed behavior, which is time-dependent in the two-phase regime. The liquid water transport occurs on a time-scale of minutes. Flooding effects that are caused by liquid water accumulation are described by this model. The gas saturation is decreased by the presence of liquid water. An important feature of the model is that the reduction of the ionic current density due to the presence of liquid water is described and that the liquid water content in the electrodes is coupled to a dynamic transport process of liquid water in the porous layers.

The validity of the model approach is shown by a comparison with experimental results. For the first time, the results of a dynamic and two-phase model on a time-scale of minutes are shown and compared with time-dependent measurement data.

Cyclic voltammograms are simulated and measured. The influence of different gas flow rates and sweep rates on the results is investigated. The test cell has a small active area and is actively water-cooled. The shape of the current-voltage characteristic is predicted correctly by the model.

A pronounced hysteresis effect is observed in the cyclic voltammograms. The modeling results show that this hysteresis is caused by an increase in the mass transport limitation on the cathode side. This is due to the time-dependent accumulation of water on the cathode side. An important part of the mathematical model is the description of the polymer membrane. The model contains a time-dependent description of the concentration and pressure-driven water transport through the membrane. The membrane model is coupled with the two-phase flow equations in the electrodes. The validity of this novel model approach is shown

by the comparison of the measured and the simulated cell resistance.
The mathematical model that is presented in Chapter 4 explains the experimentally observed hysteresis behavior of cyclic voltammograms. Hence, it is concluded that the effective medium approach that is used for the description of the fuel cell components is suitable to describe the water transport in the porous regions. Moreover, the model can predict the impact of dynamic changes of the operating conditions on the fuel cell. For example, rapid load changes can be simulated. This topic is important during start-up and operation of a fuel cell system subjected to a dynamic load. The model was applied to simulate the low frequency impedance spectrum of a PEMFC. The occurrence of an arc in the sub-Hertz region can be explained by the excitation of the liquid water transport across the membrane.

Future issues regarding the two-phase flow modeling of PEMFCs

The model that is outlined in Chapter 4 can be extended to a more complete three-dimensional description of the PEMFC. Since the validity of the model approach is shown, the model concept can be transferred to the three-dimensional case. However, time-dependent three-dimensional models that contain all coupled transport phenomena require large computational resources. In this context, the scaling analysis of the model equations can predict important characteristic quantities, such as current density and temperature profiles, prior to numerical computations. Moreover, scaling analysis indicates which phenomena can be considered decoupled without a significant loss of accuracy.
The mathematical description of the liquid water transport has been transferred from the field of ground water flow. The porous media investigated in this field have much larger typical length scales than the GDLs and the electrodes of a PEMFC. In particular, the two-phase flow properties of the fuel cell components require detailed investigation.
The capillary pressure-saturation relation for the gas diffusion layers and catalyst layers commonly used in PEMFCs have to be determined. The functional relationship that describes the dependence of the capillary pressure on the liquid water saturation is specific to a certain material. Hence, the use of standard literature approaches reduces the predictive power of fuel cell models. Furthermore, the drainage and imbibition of a structure with irregular pore geometry is expected to cause a hysteresis in the capillary pressure-saturation curve that is not captured by current model approaches. The gas diffusion layer can be considered as a random fiber material that is surface-treated with Teflon. In the mathematical description of the capillary pressure the contact angle of the layer is used. The contact angle

is defined by the Laplace equation that is valid for a regular pore geometry and usually measured on smooth surfaces. Since the pores of the GDL have irregular shape and the coating with Teflon is inhomogeneous, the use of a single contact angle cannot describe the surface properties inside the porous structure accurately.
The catalyst layer contains ionomer and platinum catalyst particles, usually on carbon support. Thus the catalyst layer may have the property of mixed wettability, i.e. it can neither be considered to be simply hydrophilic nor hydrophobic. One could argue that the two-phase flow properties of the catalyst layer are of minor importance compared to the gas diffusion layer which is usually up to 30 times thicker than the catalyst layer. This is not the case, since the state of the catalyst layer determines the properties of the membrane. The membrane in turn is extremly important for the water distribution within the fuel cell. The catalyst layer is commonly modeled as a separate layer adjacent to the membrane on one side and to the gas diffusion layer on the other side. However, the polymer conducting phase of the membrane extends into the catalyst layer, resulting in an irregular interface rather than a well-defined boundary. Moreover, the polymer phase tends to swell due to the uptake of water, which gives rises to dynamic behavior on the part of the interface. Refined fuel cell models should consider this fact.
Recently developed gas diffusion media contain a so-called microporous layer that is inserted between the GDL and the catalyst layer. While experimental results indicate that the microporous layer can improve the durability and the performance of PEMFCs, the dynamic water transport properties are changed significantly. Hence, current empirical control approaches that have been developed for fuel cells without a microporous layer are insufficient and require major modifications. Accordingly, future models should integrate the microporous layer into the mathematical description.
When modeling the phase transition of water, evaporation and condensation rate constants are commonly used. Rather than using constants, more sophisticated models should contain a functional dependence of the evaporation and condensation rates. Condensation, for example, occurs on pre-existing liquid surfaces and, hence, the surface energy influences the condensation rate. Furthermore, the impact of the temperature, the average gas velocity, and the relative humidity should be studied in detail.
Furthermore, the physical phenomena at the interface between the GDL and the open gas channel require clarification. During operation, liquid water is generated in the fuel cell and transported through the GDL. During experiments, it has been observed in transparent fuel cells that droplets emerge and grow at the surface of the GDL. These droplets are eventually removed by the convective gas flux in the channels. Fluid dynamic calculations clarify some of the properties associated with the transport of droplets through the channels. For example, the moving droplets tend to accumulate at the bends of the flowfield due to the inhomogeneous

velocity and pressure field of the gas flux. However, it is an unresolved question how to couple the liquid water transport equations in the GDL with the convective transport processes in the open gas channel without improper simplification.

6.3 Dynamic fuel cell stack modeling

Modeling results and validation

An analysis of the dynamic behavior of a PEMFC stack is given based on a novel stack model. The mathematical formulation of the stack model is a coupled differential algebraic equation system. Ordinary differential equations in time describe the transport phenomena, and the oxygen reduction at the cathode is modeled by an algebraic relation. The model is physically detailed and considers the important couplings among the transport phenomena and the electrochemical reaction. At the same time, the model is computationally efficient.
The realistic simulation results show that the modeling approach is appropriate for the dynamic description of a PEMFC stack. The model can predict the stack voltage and the molar fluxes of hydrogen, oxygen, and water vapor, given an arbitrary load profile. Moreover, the temperature of the off-gas and, most important, of the stack itself is calculated. The stack temperature is coupled with all the other phenomena that occur in a fuel cell stack. For example, the protonic conductivity is treated as a function of the temperature and its evolution is calculated.
A thorough understanding of the dynamic response of a PEMFC stack is crucial for the operational control of integrated fuel cell systems. The stack model is suitable for control applications, since the convergence behavior is excellent, as shown by the simulation of a current-step-profile. This model property allows one to examine a wide parameter range and to simulate different operating scenarios. Moreover, the model is computationally efficient. In a computing time of less than one second the dynamic response of the stack upon varying load can be predicted for an operation time of more than one hour.
The stack temperature is one of the most important parameters during operation. Accordingly, the first step of the validation was to compare the simulated with the measured stack temperature. A PEMFC stack constructed for the use in portable applications was operated under constant load. The input parameters of the model were controlled by the software of the test stand. Agreement between the simulation results and the measurement is excellent. For the validation of the electrical model a comparison of simulated and measured stack voltage is given. Deviations between the predictions of the model and the experimental results are explained by the generation and accumulation of liquid water in the stack.

Model applications

The stack model is able to identify the dominant time-dependent physical processes under changing load conditions and for different operating regimes. For example, the influence of the humidity of the inlet gases, or the heat flux that should be removed via the surface of the stack, can be simulated. By integrating the stack model into a system simulation environment, it can be utilized to study the dynamic interaction between the fuel cell stack and its peripheral components like pumps, fans, and valves. From the results of such a study, guidelines for the optimization of fuel cell systems can be drawn up. The most important application is the model-based development of a control algorithm. Currently, the control of fuel cell systems is usually managed by algorithms that are based on empirical observations and practical experience. By developing a control scheme that is based on a physical fuel cell stack model the performance of fuel cell systems can be improved.

Future issues in PEMFC stack modeling

The water and heat management of the fuel cell stack is essential for the dynamic operation and the control of fuel cell systems. The time-dependent calculation of the stack temperature has been demonstrated with high accuracy. The model approach also describes the dry-out of the membranes within the stack.
However, during operation the breakdown of a single cell voltage in the stack was frequently observed. At low temperatures this is caused by the accumulation of liquid water in the cell. Due to the physical complexity and the computational expense involved, no fuel cell stack model is available that contains a dynamic description of the two-phase flow phenomena. This shortcoming of current fuel cell stack models could be overcome by the extension of the balance model presented in Chapter 5. To achieve this, the liquid water balance needs to be coupled with the mass transport equations of the gas components. Furthermore, the influence of varying liquid water saturation on the electrode activity is important. This requires the definition of an average liquid water saturation for each cell in the stack. The effective parameters that describe the liquid water transport in the stack could be derived from measurements that address the problem of flooding specifically. For example, the concept of the cyclic voltammograms introduced in Chapter 4 could be applied to fuel cell stacks.
Alternatively, the issue of flooding could be addressed by a different model approach that unifies both computational efficiency and physical completeness. A master-program could, for example, combine a balance-like description of a fuel cell stack as presented in Chapter 5 with a more detailed model that contains a spatial resolution of the cell components as developed in Chapter 4. This would

facilitate the fast computation of the fuel cell stack behavior in operation modes where the simplified stack model is sufficient. As soon as the reduced model approach fails, for example, when flooding occurs, the master-program could switch to the detailed level of one cell or specific cell components. Hence, the model would consider different scales, the stack scale and the component scale. Eventually this concept could be extended to comprise all levels between the micro scale that spatially resolves the microstructure of particular cell components and the system scale that contains all the components of a fuel cell system. A major issue of the multiscale approach is the management of the information exchange between the levels and the definition of criteria for switching from one level to another.

Appendix

Membrane boundary conditions of the planar cell model in Chapter 3

Appropriate definition of the boundary conditions is crucial for the numerical stability of the model. To improve the stability of this model we derived Eqs. (3.32), (3.44), (3.54) and (3.55).
In the following, M_i denotes the molar mass of species i. x_i is the molar fraction of species i. The superscripts a, c, and m denote anode, cathode, and membrane, respectively. The weight fraction of oxygen w_{O_2} in the cathode is given by

$$w_{O_2} = \frac{M_{O_2}\, x_{O_2}}{M_{H_2O}\, x^c_{H_2O} + M_{N_2}\left(1 - x^c_{H_2O} - x_{O_2}\right) + M_{O_2}\, x_{O_2}} \,. \tag{6.1}$$

The weight fraction of water vapor w_{H_2O} is

$$w^c_{H_2O} = \frac{M_{H_2O}\, x^c_{H_2O}}{M_{H_2O}\, x^c_{H_2O} + M_{N_2}\left(1 - x^c_{H_2O} - x_{O_2}\right) + M_{O_2}\, x_{O_2}} \,. \tag{6.2}$$

Combining Eq. (6.1) and Eq. (6.2) yields the following expression

$$x^c_{H_2O} = \frac{M_{N_2} M_{O_2} w^c_{H_2O}}{M_{N_2} M_{O_2} w^c_{H_2O} + M_{H_2O}\left(M_{N_2} w_{O_2} - M_{O_2}\left(w^c_{H_2O} + w_{O_2} - 1\right)\right)} \,. \tag{6.3}$$

In the membrane, the weight fraction of water is given by

$$w^m_{H_2O} = \frac{M_{H_2O}\, x^m_{H_2O}}{M_{H_2O}\, x^m_{H_2O} + M_{RSO}(1 - x^m_{H_2O})} \,. \tag{6.4}$$

If the membrane humidity λ is defined as the number of water molecules per sulfonic acid group, the molar fraction of water is

$$x^m_{H_2O} = \frac{\lambda}{1+\lambda} \,. \tag{6.5}$$

In this paper, a linear relation between the humidity of the membrane and relative humidity of the air is assumed

$$\lambda = Z\, \frac{P_{ref}\, x^c_{H_2O}}{P_{sat}} \,. \tag{6.6}$$

Z is a constant of proportionality. This assumption was proposed by Yi and Nguyen [34] to improve the numerical stability of the problem. According to [33], the saturation pressure of water P_{sat} is given by

$$\log P_{sat} = 2.95 \cdot 10^{-2}\, T - 9.18 \cdot 10^{-5}\, T^2 + 1.44 \cdot 10^{-7}\, T^3 - 2.18\ . \tag{6.7}$$

Combining Eqs.(6.3), (6.4), (6.5), and (6.6) yields Eq. (3.54). If Eq. (3.54) is solved for $w^c_{H_2O}$ Eq. (3.32) follows.
The molar fraction of water vapor in the anode is

$$x^a_{H_2O} = \frac{M_{H_2} w^a_{H_2O}}{M_{H_2O} + w^a_{H_2O}(M_{H_2} - M_{H_2O})}\ . \tag{6.8}$$

Again, a linear relation between λ and relative humidity within the anode is assumed,

$$\lambda = Z\ \frac{P_{ref}\ x^a_{H_2O}}{P_{sat}}\ . \tag{6.9}$$

Combining Eqs. (6.4), (6.5), (6.8), and (6.9) yields Eq. (3.55). Eq. (3.55) is solved for $w^a_{H_2O}$ to obtain Eq. (3.44).

Supporting equations of the stack model in Chapter 5

To calculate the open circuit voltage at different temperatures and pressures the Nernst Equation is used

$$V_{oc} = V^{ref}_{oc} + \frac{RT}{2F} ln\left(\frac{a_{H_2} a^{0.5}_{O_2}}{a_{H_2O}}\right), \tag{6.10}$$

where V^{ref}_{oc} is the open circuit voltage at standard temperature and pressure.
By assuming that the gases in the channels can be treated as ideal gases, the following equation can be used to transform the concentration $c_{k,i}$ into the molar flow $N_{q,i}$

$$c_{q,i} = \frac{N_{q,i}}{A_q v_{q,i}}\ . \tag{6.11}$$

The partial pressure p_i of the different species is calculated according to Dalton's law

$$p_i = \frac{N_{q,i}}{\sum N_{q,j}} P_q\ . \tag{6.12}$$

For the electro-osmotic drag coefficient the empirical equation of Springer [25] is used

$$n_{drag} = (5/44)\lambda_m \ . \tag{6.13}$$

The saturation pressure of water vapor is calculated using Eq. (6.7)
The diffusion coefficient of water in the membrane D_{m,H_2O} as a function of λ_m and T_{sol} is described by the following empirical equation in Golbert [82]

$$D_{m,H_2O} = n_{drag} D^{ref}_{m,H_2O} exp\left(2416\left(\frac{1}{T_{ref}} - \frac{1}{T_s}\right)\right) \ , \tag{6.14}$$

where D^{ref}_{m,H_2O} is the diffusion coefficient of water in the membrane.
The activity of water in the electrode q is modeled as follows [82]

$$a_q = \frac{N_{q,H_2O^v}}{\sum_i N_{q,i}} \frac{P_q}{P_{sat}} \ . \tag{6.15}$$

Table Ia. List of Parameters and Constants

Symbol	Explanation	Value	Unit	Ref.
A_q	cross-sectional area of gas channel in stack	$7 \cdot 10^{-7}$	m^2	meas.
A_s	cross-sectional area of cell	$5.5 \cdot 10^{-4}$	m^2	meas.
A_{sg}	heat exchange area per unit length between solid and gas	$3.4 \cdot 10^{-4}$	m	meas.
A_{ss}	heat exchange area per unit length between solid and surroundings	0.65	m	meas.
a	active surface area per unit volume	$1.1 \cdot 10^{7}$	m^{-1}	est.
C	fitted for BET adsorption isotherm	150		[70]
C_{H_2}	heat capacity of hydrogen	28.8	J/mol K	[14]
$C_{H_2O^v}$	heat capacity of water vapor	33.6	J/(mol K)	[14]
$C_{H_2O^l}$	heat capacity of liquid water	75.3	J/(mol K)	[14]
C_{N_2}	heat capacity of nitrogen	29.1	J/(mol K)	[14]
C_{O_2}	heat capacity of oxygen	29.3	J/(mol K)	[14]
C_s	average heat capacity of solid parts of stack	1000	J/(kg K)	meas.
D_A	diffusion constant within agglomerate particle	$5 \cdot 10^{-10}$	m^2/s	est.
D_{H_2}	diffusivity of hydrogen in gas	$3.5 \cdot 10^{-5}$	m^2/s	[14]
D_{H_2O}	diffusivity of water vapor in gas	$2.2 \cdot 10^{-5}$	m^2/s	[14]
$\mathcal{D}^0_{H_2O\ RSO}$	binary diffusion coefficient	$5.5 \cdot 10^{-11}$	m^2/s	[46]
D^{ref}_{m,H_2O}	diffusion coefficient of water in membrane	$5.5 \cdot 10^{-11}$	m^2/s	[82]
D_{O_2}	diffusivity of oxygen in gas	$1.8 \cdot 10^{-5}$	m^2/s	[14]
d	diameter of anodic gas channel	$1 \cdot 10^{-3}$	m	[44]
d_f	fiber diameter in gas diffusion layer	7	μm	est.
d_m	thickness of the membrane	$25 \cdot 10^{-6}$	m	meas.
d_y	scale factor for channel width	1		meas.
$E^A_{H_2O,RSO}$	activation energy	20.25	kJ/mol	[46]
EW	equivalent weight of the dry membrane	0.909	kg/mol	[46]
F	Faraday's constant	96485.3	C/mol	[15]
H_{O_2}	Henry's constant	$3.2 \cdot 10^{4}$	Pa m^3/mol	[14]
$[H_2]^{ref}$	reference hydrogen concentration	$21.9 \cdot 10^{-3}$	mol/m^3	[44]
h	channel height	$7 \cdot 10^{-4}$	m	meas.
$i_a, i_{0,a}$	anodic exchange current density	$1 \cdot 10^{3}$	A/m^2	est.
$i_c, i_{0,c}$	cathodic exchange current density	$1 \cdot 10^{-3}$	A/m^2	[87]
$K_{1,5}$	permeability of the GDL in the test cell	$1 \cdot 10^{-14}$	m^2	est.

Table Ib. List of Parameters and Constants

Symbol	Explanation	Value	Unit	Ref.
K_{GDL}	typical gas diffusion layer permeability	$1 \cdot 10^{-14}$	m^2	est.
$K_{2,4}$	permeability of the catalyst layers	$1 \cdot 10^{-14}$	m^2	ass.
K_{sat}	absolute permeability of liquid-filled membrane	$1.8 \cdot 10^{-18}$	m^2	[58]
$k_{1/8}$	thermal conductivity of fiberglass	0.18	W/(m K)	[88]
$k_{2/6}$	thermal conductivity of diffusion layer	1.67	W/(m K)	[32]
$k_{3/5}$	thermal conductivity of catalyst layer	0.67	W/(m K)	[89]
k_4	thermal conductivity of membrane	0.67	W/(m K)	[89]
k_c	condensation rate constant	$1 \cdot 10^4$	s^{-1}	est.
k_K	Kozeny constant	6		[66]
$k_{m,p}$	water permeability of membrane	$1.58 \cdot 10^{-18}$	m^2	[82]
k_s	heat conduction coefficient of solid	0.5	W/(m K)	[34]
k_v	evaporation rate constant	$5.1 \cdot 10^{-5}$	1/(Pa s)	[64]
L_{eff}	effective channel length	0.88	m	est.
l	length of anodic gas channel	$43 \cdot 10^{-3}$	m	[44]
M_{H_2}	molar mass of hydrogen	0.002	kg/mol	[14]
M_{H_2O}	molar mass of water	0.018	kg/mol	[14]
M_{O_2}	molar mass of oxygen	0.032	kg/mol	[14]
M_{N_2}	molar mass of nitrogen	0.028	kg/mol	[14]
M_{RSO}	equivalent weight of the polymer	0.909	kg/mol	[46]
n	total number of water layers inside pores at saturation	13.5		[70]
n_{cells}	number of cells in the stack	6		
n_{chan}	number of channels in one cell	4		
$[O_2]^{ref}$	reference oxygen concentration	$4.7 \cdot 10^{-3}$	mol/m^3	[44]
P_{ref}	gas pressure	101300	Pa	meas.
Δp	pressure drop along the channel	13.5	Pa	[44]
R	gas constant	8.314	J/(K mol)	[15]
R_{aggl}	mean agglomerate radius	$1 \cdot 10^{-7}$	m	[75]
s_l^{im}	immobile saturation	0.1		[66]
ΔS_a	reaction entropy of anodic reaction	0.104	J/(K mol)	[49]
ΔS_c	reaction entropy of cathodic reaction	-326.36	J/(K mol)	[49]
T	cell temperature in Chap. 4	313	K	meas.
T^0	reference temperature	298	K	[44]
T_{ref}	reference temperature	298	K	[71]
T_s	ambient temperature	298	K	[44]
t_m	thickness of membrane	$25 \cdot 10^{-6}$	m	meas.
U_0	amplitude of perturbation	$10 \cdot 10^{-3}$	V	

Table Ic. List of Parameters and Constants

Symbol	Explanation	Value	Unit	Ref.
U_{sg}	heat transfer coefficient between solid and gas	25	W/(m^2 K)	[34]
U_{ss}	heat transfer coefficient between solid and surroundings	25	W/m^2 K)	[34]
V_{cell}	cell potential in Chapter 3	0.4	V	
V_{oc}^{ref}	open-circuit voltage at standard temperature and pressure	1.1	V	[34]
v_{H_2}	diffusion volume of hydrogen	$7.07 \cdot 10^{-6}$	m^3/mol	[45]
v_{H_2O}	diffusion volume of water vapor	$12.7 \cdot 10^{-6}$	m^3/mol	[45]
v_{N_2}	diffusion volume of nitrogen	$17.9 \cdot 10^{-6}$	m^3/mol	[45]
v_{O_2}	diffusion volume of oxygen	$16.6 \cdot 10^{-6}$	m^3/mol	[45]
w	channel width	$1 \cdot 10^{-3}$	m	meas.
$w_{H_2}^{in}$	weight fraction of hydrogen at inlet	1		[44]
$w_{H_2O}^{in}$	weight fraction of water vapor	0.0098		[44]
$w_{O_2}^{in}$	weight fraction of oxygen at openings	0.2343		[44]
$x_{H_2}^{in}$	molar fraction of H_2 at inlet	0.98		est.
$x_{H_2}^{ref}$	reference molar fraction of H_2	1		ass.
$x_{H_2O}^{in}$	molar fraction of water vapor at inlet	0.014		est.
$x_{O_2}^{in}$	molar fraction of O_2 at inlet	0.15		est.
$x_{O_2}^{ref}$	reference molar fraction of O_2	1		[71]
Z	constant of proportionality	14		[34]
z_a	exchanged electrons at anode	2		ass.
z_c	exchanged electrons at the cathode in Chap. 3	2		[71]
z_c	exchanged electrons at the cathode for $\eta_c \leq 400\ mV$	2		[71]
z_c	exchanged electrons at cathode for $\eta_c > 400\ mV$	1		[71]
α_a	charge transfer coefficient at anode	0.3		[46]
α_c	charge transfer coefficient at cathode	0.5		[71]
α_w	heat transfer coefficient	20	W/(m K)	[90]
δ	mass accommodation coefficient	$7 \cdot 10^{-4}$		ass.
ΔH_{vap}	enthalpy of water evaporation	44000	J/mol	[14]
$\Delta\Phi_{a,eq}$	reference equilibrium potential	0	V	
$\Delta\Phi_{c,eq}$	reference equilibrium potential	1.229	V	[72]
ε_b	emittance	0.8		[90]
θ_a	activity coefficient	1		ass.

Table Id. List of Parameters and Constants

Symbol	Explanation	Value	Unit	Ref.
θ_a	apparent contact angle of catalyst layer	135	$^\circ$	meas.
$\theta_{1/5}$	contact angle of gas diffusion layers	115	$^\circ$	[66]
$\theta_{2/4}$	contact angle of catalyst layer	115	$^\circ$	meas.
θ_3	contact angle of membrane	90.02	$^\circ$	[58]
λ_l^{max}	membrane humidity in liquid water	22		[70]
λ_v^{max}	membrane humidity in saturated vapor	14		[70]
λ_m	water loading at monolayer coverage	1.8		[70]
μ	viscosity of hydrogen	$8.42 \cdot 10^{-6}$	Pa s	[14]
$\mu_{g,1/2}$	viscosity of hydrogen	$8.42 \cdot 10^{-6}$	Pa s	[14]
$\mu_{g,4/5}$	viscosity of air	$17.2 \cdot 10^{-6}$	Pa s	[14]
μ_l	viscosity of water	$3.56 \cdot 10^{-4}$	Pa s	[14]
ν	volume fraction of ionomer in the catalyst layer	0.4		est.
$\pi_{1/5}$	porosity of gas diffusion layer in Chap. 4	0.4		[91]
π_{GDL}	typical porosity of gas diffusion layer	0.4		[91]
$\pi_{2/4}$	porosity of catalyst layer in Chap. 4	0.4		[91]
$\pi_{2/6}$	porosity of gas diffusion layer in Chap. 3	0.4		[91]
$\pi_{3/5}$	porosity of catalyst layer in Chap. 3	0.4		[75]
ρ_l	density of water	996.56	kg/m^3	[14]
ρ_m	dry density of membrane	1980	kg/m^3	[54]
ρ_s	average density of stack material	1350	kg/m^3	est.
$\sigma_{e,2/6}$	conductivity of gas diffusion layer	1400	S/m	[91]
$\sigma_{e,3/5}$	conductivity of the catalyst layer	215	S/m	ass.
σ_{SB}	Stefan-Boltzmann constant	$5.67 \cdot 10^{-8}$	W/(m^2 K^4)	[15]
$\sigma_{e,1/5}$	conductivity of gas diffusion layer	1400	S/m	[91]
$\sigma_{e,2/4}$	conductivity of the catalyst layer	300	S/m	[75]
$\tau_{2/6}$	tortuosity of gas diffusion layer	2.6		[25]
$\tau_{3/5}$	tortuosity of catalyst layer	2.6		est.
ϕ_s	ratio of solid-liquid contact area to nominal base area of droplet	0.5		est.

Table IIa List of Symbols

Symbol	Explanation	Unit
A_{lg}	interfacial area between liquid and gas phase	m^2
A_{sf}	interfacial area between solid and fluid	m^2
a_{i0}	phenomenological coefficient	kg/(m s)
a_{ij}	phenomenological coefficient	kg^2/(m s J)
a_i	activity of species i	
a_q	activity of water vapor in electrode k	
c	concentration	mol/m^3
$c_{q,i}$	concentration of species i in electrode q	mol/m^3
$D_{GDL,l}$	generalized liquid water diffusion coefficient in the GDL	m^2/s
$D^m_{H_2O}$	diffusion coefficient of water vapor in the membrane	m^2/s
D_i	Fick diffusivity of species i	m^2/s
D_{ij}	multicomponent Fick diffusivity	m^2/s
$\mathcal{D}_{ij}$	Maxwell-Stefan diffusivity of species i, j	m^2/s
$\mathtt{D}_{ij}$	binary diffusivity	m^2/s
$D^{eff}_{i,\kappa}$	effective diffusivity of species i in subdomain κ	m^2/s
D^T_i	multicomponent thermal diffusion coefficient	kg/(m s)
D_{m,H_2O}	diffusion coefficient of water in membrane	m^2/s
$D_{m,l}$	generalized liquid water diffusion coefficient in the membrane	m^2/s
$\vec{d}_i$	diffusional driving force	m^{-1}
$\vec{E}$	electric field	V/m
$\vec{e}$	total energy flux	J/(m^2 s)
$e_{x/y}$	Cartesian normal vector	
f	volume fraction of water in the membrane	
f_l	maximum value of water volume fraction in liquid-filled membrane	
$\bar{G}$	partial molar enthalpy	J/mol
$\triangle G$	activation Gibbs energy	J/mol
g_i	external force per unit mass acting on species i	N/kg
g_s	entropy production rate	J/(K m^3 s)
$\vec{g}$	gravity vector	m/s^2
H	Heaviside function	
$\hat{H}$	enthalpy per unit mass	J/kg
$\bar{H}_i$	partial molar enthalpy	J/mol
$[H_2]^s$	concentration of hydrogen at agglomerate surface	mol/m^3
h	height of gas channel	m
I	current density in the fuel cell stack	A/m^2
i	current density at planar electrode	A/m^2

Table IIb List of Symbols

Symbol	Explanation	Unit
i_0	exchange current density	A/m^2
i_{aggl}	average current density at agglomerate surface	A/m^2
J	Leverett function	
$\vec{J}_i$	molar flux with respect to mass average velocity	mol/(m^2 s)
$\vec{J}^*$	molar flux with respect to $\vec{v}^*$	mol/(m^2 s)
$\vec{j}$	overall, measurable current density	A/m^2
j_0	perturbation amplitude	A/m^2
$\vec{j}_{c/a}$	ionic current density	A/m^2
$\vec{j}_D$	diffusion current density	A/m^2
$\vec{j}_E$	field current density	A/m^2
$\vec{j}_e$	electron current density	A/m^2
$\vec{j}_i$	diffusive mass flux of species i	kg/(m^2 s)
$\vec{j}_p$	proton current density	A/m^2
$\vec{j}_M$	diffusive mass flux with respect to $\vec{v}$	kg/(m^2 s)
$\mathbf{K}$	intrinsic permeability tensor	m^2
$\mathbf{K}_k$	conductivity of phase k	m^2
K_κ	scalar permeability of subdomain κ	m^2
k	thermal conductivity	W/(K m)
k_a'', k_{red}	reaction rate constant of hydrogen oxidation reaction	m/s
k_c'', k_{ox}	reaction rate constant of oxygen reduction reaction	m/s
k_k, k_{rk}	relative permeability of phase k	
M_a	molar mass of gas mixture on anode side	kg/mol
M_c	molar mass of gas mixture on cathode side	kg/mol
M_i	molar mass of species i	kg/mol
M_m	molar mass of polymer-water mixture in the membrane	kg/mol
$\vec{N}$	combined molar flux	mol/(m^2 s)
$N_{q,i}$	molar flow rate of species i in electrode q	mol/s
N_{H_2O}	molar flux of water	mol/(m^2 s)
N_{O_2}	oxygen diffusion flux	mol/(m^2 s)
$\vec{n}_i$	combined mass flux of species i	kg/(m^2 s)
$\vec{n}$	geometry boundary normal vector	
n_{aggl}	number of agglomerates per unit volume	1/m^3
n_{drag}	electro-osmotic drag coefficient	
n_{m,H_2O}	number of water molecules in the membrane	
n_{m,SO_3}	number of SO_3 groups in the membrane	
$[O_2]^s$	concentration of oxygen at agglomerate surface	mol/m^3
P_k	average pressure in electrode q	Pa
p	gas pressure	Pa

Table IIc List of Symbols

Symbol	Explanation	Unit
p_c	capillary pressure	Pa
$p_{H_2O}, p_{H_2O^v}$	water vapor partial pressure	Pa
p_i	partial pressure of species i	Pa
p_k	pressure of phase k	Pa
P_{sat}	saturation pressure	Pa
$Q_{c/a,C}$	charge generation rate	A/m^3
$Q_{c/a}^{mean}$	average charge generation rate	A/m^3
Q_C	charge source term	$C/(m^3\ s)$
Q_E	general heat source term	J/m^3
Q_M	mass source term	$kg/(m^3\ s)$
Q_m	molar source term	$mol/(m^3\ s)$
Q_{norm}^C	normalized charge generation rate	
$\vec{q}$	heat flux	$J/(m^2\ s)$
$\vec{q}_h$	measurable heat flux	$J/(m^2\ s)$
RH	relative humidity	
$RHS9$	right-hand side of Eq. (9)	A/m^3
$RHS13$	right-hand side of Eq. (13)	A/m^3
r_c	critical pore radius in the membrane	nm
r_i	rate of production due to reaction	$kg/(m^3\ s)$
S	fraction of expanded channels in the membrane	
S_{aggl}	outer surface area of single agglomerate particle	m^2
S_h	rate of energy production or consumption	W/m^3
S_{mean}	mean value of S	
$\hat{s}$	entropy per unit mass	J/(K kg)
$\vec{s}$	entropy flux	$J/(K\ m^2)$
s_k	volume saturation of phase k	
s_l^{avg}	average saturation of the GDL	
T	temperature	K
t	time	s
$\hat{U}$	internal energy per unit mass	J/kg
$\vec{u}$	velocity in anodic gas channel	m/s
$u_{x,y}$	Cartesian components of $\vec{u}$	m/s
V	unit volume	m^3
$\hat{V}$	volume per unit mass	m^3/kg
V_{cell}	cell voltage	V
V_{H_2O}	molar volume of water	m^3/mol
V_m	partial molar volume of dry membrane	m^3/mol
$V(r)$	normalized differential volume of channels	nm^{-1}

Table IId List of Symbols

Symbol	Explanation	Unit
$\vec{v}$	mass average velocity	m/s
$\vec{v}^*$	molar average velocity	m/s
$\vec{v}_{ak}$	average velocity of phase k	m/s
$\vec{v}_i$	velocity of species i	m/s
$\vec{v}_k$	Darcy velocity of phase k	m/s
v_m	molecular speed	m/s
$W_{ARa/c}$	molar rate of conversion in agglomerate particle	mol/s
x_i	molar fraction of species i	
x, y	Cartesian co-ordinates	m
z	number of exchanged electrons in rate-determining step	
Z	electrical impedance	Ω m^2

Table IIIa Greek Symbols

Symbol	Explanation	Unit
α_{net}	net water migration coefficient	
α	charge transfer coefficient	
α_g	vapor-equilibrated transport coefficient	$mol^2/(J\ m\ s)$
α_l	liquid-equilibrated transport coefficient	$mol^2/(J\ m\ s)$
Γ_{drag}	flux vector	$kg/(m^2\ s)$
η	overpotential	V
η_a	overvoltage at the anode	V
η_c	overvoltage at the cathode	V
θ	contact angle of water	$^\circ$
Λ	surface area of agglomerate per unit volume	m^2/m^3
λ	membrane humidity	
λ_v	membrane humidity for contact with water vapor	
μ	electrochemical potential	J/mol
μ_k	dynamic viscosity of phase k	kg/(m s)
ν	mobility	$m^2/(V\ s)$
ξ	electro-osmotic drag coefficient	
π	porosity	
π_k	volume fraction of phase k	
ρ	mass density	kg/m^3
ρ_a	density of gas mixture on anode side	kg/m^3
ρ_c	density of gas mixture on cathode side	kg/m^3
ρ_C	overall charge density	C/m^3
ρ_k	density of phase k	kg/m^3
ρ_m	density of polymer-water mixture in the membrane	kg/m^3
τ	viscous stress	$kg/(m\ s^2)$
τ_κ	tortuosity of subdomain κ	
$\tau_{GDL,l}$	time constant of liquid water transport across the gas diffusion layer	s
$\tau_{m,l}$	time constant of liquid water transport across the membrane	s
σ	conductivity	S/m
σ_{H_2O}	surface tension of water	N/m
σ_m	conductivity of membrane	
ψ	electrostatic potential	V
ϕ_e	electrochemical potential of the electrode	V
ϕ_p	electrochemical potential of the electrolyte	V
$\triangle\phi$	galvanic potential difference	V
Ω_κ	geometry subdomain κ	
ω_i	mass fraction of species i	

Table IIIb Greek Symbols

Symbol	Explanation	Unit
$\omega_{m,l}$	characteristic frequency of liquid water transport across the membrane	1/s
$\partial\Omega_\kappa$	geometry boundary κ	

Table IV Subscripts and Superscripts

Symbol	Explanation
0	equilibrium
a	anodic, oxidation, at the anode
C	charge
c	cathodic, reduction, at the cathode
D	diffusive
$drag$	electro-osmotic drag
E	driven by electric field
e	electronic, electron-conducting phase
eq	equilibrium
f	species index
g	gas phase
H	heat
i	species index, also denoting electron and proton-conducting phases
in	inlet
j	species index
k	phase index in multiphase flow equations
l	liquid phase
M	mass
m	molar
m	in the membrane
oc	open circuit
out	outlet
ox	oxidation, oxidized
p	protonic, electrolyte phase
q	in anode or cathode
red	reduction, reduced
ref	reference
sg	exchange between solid and gas
sol	solid material
ss	exchange between solid and surroundings
sur	surroundings
S	surrounding
vap	evaporation
$\bar{X}$	average value of X
κ	subdomain and boundary index

Abbreviations

Symbol	Explanation
ass.	assumption
DAE	differential algebraic equation
ESEM	environmental scanning electron microscope
est.	estimation
GDL	gas diffusion layer
MEA	membrane electrode assembly
meas.	measurement
ODE	ordinary differential equation
PCB	printed circuit board
PDE	partial differential equation
PEMFC	proton exchange membrane fuel cell
PTFE	polytetrafluoroethylene
REV	representative elementary volume
TEM	transmission electron microscope

Bibliography

[1] C. Dyer, Fuel cells for portable applications, Journal of Power Sources 106 (2002) 31–34.

[2] M. Broussely, G. Archdale, Li-ion batteries and portable power source prospects for the next 5-10 years, J. Power Sources 136 (2004) 386–394.

[3] E. Bostic, N. Siefer, C. Bolton, U. Ritter, T. Dubois, The US army foreign comparative test fuel cell program, J. Power Sources 137 (2004) 76–79.

[4] European Portable Fuel Cell Study, Fraunhofer ISE, Freesen and Partner, VDI/VDE-IT, 2003.

[5] J. Ogden, T. Kreutz, M. Steinbugler, Fuels for fuel cell vehicles, Fuel Cells Bulletin 3 (2000) 5–12.

[6] H. Schlesinger, H. Brown, A. Finholt, J. Gilbreath, H. Hoekstra, E. Hyde, Sodium borohydride, its hydrolysis and its use as a reducing agent and in the generation of hydrogen, J.Am.Chem.Soc. 75 (1953) 215.

[7] R. Aiello, J. Sharp, M. Matthews, Production of hydrogen from chemical hydrides via hydrolysis with steam, Int. J. Hydrogen Energy 24 (1999) 1123–1130.

[8] A. Dillon, K. Jones, T. Bekkedahl, C. Kiang, D. Bethune, M. Heben, Storage of hydrogen in single-walled carbon nanotubes, Nature 386 (1997) 377–379.

[9] M. Cropper, Fuel cells for people, Proceedings of The fuel cell world (2003) 43–54.

[10] A. Heinzel, C. Hebling, M. Müller, M. Zedda, C. Müller, Fuel cells for low power applications, J. Power Sources 105 (2002) 250–255.

[11] D. Rand, R. Dell, The hydrogen economy: a threat or an opportunity for lead-acid batteries?, J. Power Sources 144 (2005) 568–578.

[12] R. Dell, D. Rand, Clean Energy, The Royal Society of Chemistry, Cambridge, UK, 2004.

[13] A. Bard, L. Faulkner, Electrochemical Methods, 2nd ed., Wiley, New York, 2001.

[14] P. Atkins, Physical Chemistry, Oxford University Press, Oxford, 1994.

[15] R. Bird, W. Stewart, E. Lightfoot, Transport Phenomena, 2nd ed., Wiley, New York, 2001.

[16] N. Ashcroft, N. Mermin, Solid State Physics, Saunders College, Philadelphia, 1976.

[17] R. Helmig, Multiphase Flow and Transport Processes in the Subsurface, Springer, Berlin, 1997.

[18] S. Whitaker, Flow in porous media I: a theoretical derivation of Darcy's law, Transport in Porous Media 1 (1986) 3–25.

[19] J. Bear, Y. Bachmat, Macroscopic modelling of transport phenomena in porous media 2: applications to mass, momentum, and energy transport, Transport in Porous Media 1 (1998) 221–269.

[20] A. Scheidegger, The Physics of Flow Through Porous Media, University of Toronto Press, Toronto, 1974.

[21] J. Amphlett, R. Mann, B. Peppley, P. Roberge, T. Harris, Performance modeling of the Ballard Mark IV solid polymer electrolyte fuel cell, J. Electrochem. Soc. 142 (1995) 1–8.

[22] D. Bernardi, M. Verbrugge, A mathematical model of a solid polymer electrolyte fuel cell, J. Electrochem. Soc. 139 (1992) 2477–2491.

[23] D. Bernardi, M. Verbrugge, A mathematical model of a gas diffusion electrode bonded to a polymer electrolyte, AIChE J. 37 (1991) 1151–1163.

[24] L. Pisani, G. Murgia, M. Valentini, B. D'Aguanno, A working model of polymer electrolyte fuel cells, J. Electrochem. Soc. 149 (2002) A898–A904.

[25] T. Springer, T. Zawodzinski, S. Gottesfeld, Polymer electrolyte fuel cell model, J. Electrochem. Soc. 138 (1991) 2334–2341.

[26] T. Springer, M. Wilson, S. Gottesfeld, Modeling and experimental diagnostics in polymer electrolyte fuel cells, J. Electrochem. Soc. 140 (1993) 3513–3526.

[27] A. Kulikovsky, Performance of a polymer electrolyte fuel cell with long oxygen channel, Electrochemistry Communications 4 (2002) 527–534.

[28] R. Mann, J. Amphlett, M. Hooper, H. Jensen, B. Peppley, P. Roberge, Development and application of a generalised steady-state electrochemical model for a proton exchange membrane fuel cell, Journal of Power Sources 86 (2000) 173–180.

[29] C. Marr, X. Li, Composition and performance modelling of catalyst layer in a proton exchange membrane fuel cell, Journal of Power Sources 77 (1999) 17–27.

[30] J. Baschuk, X. Li, Modelling of polymer electrolyte membrane fuel cells with variable degrees of water flooding, Journal of Power Sources 86 (2000) 181–196.

[31] T. Fuller, J. Newman, Water and thermal management in solid-polymer-electrolyte fuel cells, J. Electrochem. Soc. 140 (1993) 1218–1225.

[32] A. Rowe, X. Li, Mathematical modeling of proton exchange membrane fuel cells, Journal of Power Sources 102 (2001) 82–96.

[33] T. Nguyen, R. White, A water and heat management model for proton-exchange-membrane fuel cells, J. Electrochem. Soc. 140 (1993) 2178–2186.

[34] J. Yi, T. Nguyen, An along-the-channel model for proton exchange membrane fuel cells, J. Electrochem. Soc. 145 (1998) 1149–1159.

[35] R. Bradean, K. Promislow, B. Wetton, Transport phenomena in the porous cathode of a proton exchange membrane fuel cell, Numerical Heat Transfer Part A, 42 (2002) 121–138.

[36] V. Gurau, H. Liu, S. Kakac, Two-dimensional model for proton exchange membrane fuel cells, AIChE J. 44 (1998) 2410–2422.

[37] A. Kulikovsky, J. Divisek, A. Kornyshev, Modeling the cathode compartment of polymer electrolyte fuel cells: dead and active reaction zones, J. Electrochem. Soc. 146 (1999) 3981–3991.

[38] S. Shimpalee, S. Dutta, Numerical prediction of temperature distribution in PEM fuel cells, Numerical Heat Transfer Part A, 28 (2000) 111–128.

[39] T. Berning, D. Lu, N. Djilali, Three-dimensional computational analysis of transport phenomena in a proton exchange membrane fuel cell, Journal of Power Sources 106 (2002) 284–294.

[40] S. Dutta, S. Shimpalee, J. van Zee, Numerical prediction of mass-exchange between cathode and anode channels in a proton exchange membrane fuel cell, International Journal of Heat and Mass Transfer 44 (2001) 2029–2042.

[41] W. k. Lee, S. Shimpalee, J. van Zee, Verifying predictions of water and current distributions in a serpentine flow field polymer electrolyte membrane fuel cell, J. Electrochem. Soc. 150 (2003) A341–A348.

[42] R. O'Hayre, D. Braithwaite, W. Hermann, S.-J. Lee, T. Fabian, S.-W. Cha, Y. Saito, F. Prinz, Development of portable fuel cell arrays with printed-circuit technology, Journal of Power Sources 124 (2003) 459–472.

[43] A. Schmitz, M. Tranitz, S. Wagner, R. Hahn, C. Hebling, Planar self-breathing fuel cells, Journal of Power Sources 118 (2003) 162–171.

[44] A. Schmitz, S. Wagner, R. Hahn, H. Uzun, C. Hebling, Stability of planar proton exchange membrane fuel cells in Printed Circuit Board technology, Journal of Power Sources 127 (2004) 197–205.

[45] J. Wesselingh, R. Krishna, Mass Transfer in Multicomponent Mixtures, Delft University Press, Delft, 2000.

[46] M. Woehr, K. Bolwin, W. Schnurnberger, M. Fischer, W. Neubrand, G. Eigenberger, Dynamic Modelling and Simulation of a Polymer Membrane Fuel Cell Including Mass Transport Limitation, Int. J. Hydrogen Energy 23 (1998) 213–218.

[47] FEMLAB is a registered trademark of COMSOL AB, www.comsol.com.

[48] P. Deuflard, A modified Newton method for the solution of ill-conditioned systems of nonlinear equations with application to multiple shooting, Numer. Math. 22 (1974) 289–315.

[49] M. Lampinem, M. Fomino, Analysis of the energy and entropy changes for half cell reactions, J. Electrochem. Soc. 140 (1993) 3537–3546.

[50] Z. Wang, C. Wang, K. Chen, Two-phase flow and transport in the air cathode of proton exchange membrane fuel cells, Journal of Power Sources 94 (2001) 40–50.

[51] L. You, H. Liu, A two-phase flow and transport model for the cathode of PEM fuel cells, Int. J. Heat and Mass Transfer 45 (2002) 2277–2287.

[52] N. Siegel, M. Ellis, D. Nelson, M. Spakovsky, A two-dimensional computational model of a PEMFC with liquid water transport, Journal of Power Sources 128 (2004) 173–184.

[53] T. Berning, N. Djilali, A 3D, multiphase, multicomponent model of the cathode and anode of a PEM fuel cell, J. Electrochem. Soc. 150 (2003) A1589–A1598.

[54] U. Pasaogullari, C. Wang, Liquid water transport in the gas diffusion layer of polymer electrolyte fuel cells, J. Electrochem. Soc. 151 (2004) A399–A406.

[55] A. Weber, J. Newman, Transport in polymer-electrolyte membranes, III. Model validation in a simple fuel cell model, J. Electrochem. Soc. 151 (2004) A326–A339.

[56] M. Ceraolo, C. Miulli, A. Pozio, Modelling static and dynamic behaviour of proton exchange membrane fuel cells on the basis of electro-chemical description, Journal of Power Sources 113 (2003) 131–144.

[57] K. Kühn, M. Ohlberger, J. O. Schumacher, C. Ziegler, R. Klöfkorn, A dynamic two-phase flow model of proton exchange membrane fuel cells, Proceedings of 2nd European PEFC forum 1 (2003) 283–296.

[58] A. Weber, J. Newman, Transport in polymer-electrolyte membranes, II. Mathematical model, J. Electrochem. Soc. 151 (2004) A311–A325.

[59] C. Wang, P. Cheng, A multiphase mixture model for multiphase multicomponent transport in capillary porous media, Int. J. Heat Mass Transfer 39 (1996) 3607–3618.

[60] M. Leverett, Capillary behavior in porous solids, Transactions of the AIME 142 (1941) 152–169.

[61] R. Brooks, A. Corey, Hydraulic properties of porous media, Hydrol. Pap. 3 (1964) 152–169.

[62] M. van Genuchten, A closed-form equation for predicting the hydraulic conductivity of unsaturated soils, Soil Sci. Am. J. 44 (1980) 892–898.

[63] IAPWS Release on Surface Tension of Ordinary Water Substance, International Association for the Properties of Water and Steam, London, 1994.

[64] T. Nguyen, Modeling two-phase flow in the porous electrodes of proton exchange membrane fuel cells using the interdigitated flow fields, The Electrochemical Society Proceedings 99-14 (1999) 222–241.

[65] N. Morrow, Irreducible wetting-phase saturation in porous media, Chem. Eng. Sci. 25 (1970) 1799–1815.

[66] J. Nam, M. Kaviany, Effective diffusivity and water-saturation distribution in single- and two-layer PEMFC diffusion medium, Int. J. Heat and Mass Transfer 46 (2003) 4595–4611.

[67] M. Eikerling, Y. Kharkats, A. Kornyshev, Y. Volfkovich, Phenomenological theory of electro-osmotic effect and water management in polymer electrolyte proton-conducting membranes, J. Electrochem. Soc. 145 (1998) 2684–2699.

[68] A. Weber, J. Newman, Transport in polymer-electrolyte membranes, I. Physical model, J. Electrochem. Soc. 150 (2003) A1008–A1015.

[69] P. Futerko, I. Hsing, Thermodynamics of water vapor uptake in perfluorosulfonic acid membranes, J. Electrochem. Soc. 146 (1999) 2049.

[70] T. Thampan, S. Malhotra, H. Tang, R. Datta, Modeling of conductive transport in proton-exchange membranes for fuel cells, J. Electrochem. Soc. 147 (2000) 3242–3250.

[71] A. Parthasarathy, C. R. Martin, S. Srinivasan, Investigations of the O_2 reduction reaction at the Platinum Nafion Interface using a solid state electrochemical cell, J. Electrochem. Soc. 138 (1991) 916–920.

[72] A. Parthasarathy, B. Dave, S. Srinivasan, A. Appleby, The platinum microelectrode/Nafion interface: an electrochemical impedance spectroscopic analysis of oxygen reduction kinetics and Nafion characteristics, J. Electrochem. Soc. 139 (1992) 1634–1641.

[73] A. Parthasarathy, S. Srinivasan, A. Appleby, Temperature dependence of the electrode kinetics of oxygen reduction at the platinum/Nafion interface, J. Electrochem. Soc. 139 (1992) 2530–2537.

[74] J. Ihonen, M. Mikkola, G. Lindbergh, Flooding of gas diffusion backing in PEFCs, J. Electrochem. Soc. 151(8) (2004) A1152–A1161.

[75] P. Gode, F. Jaouen, G. Lindbergh, A. Lundblad, G. Sundholm, Influence of the composition on the structure and electrochemical characteristics of the polymer electrolyte fuel cell cathode, Electrochimica Acta 48 (2003) 4175–4187.

[76] J. Bico, C. Marzolin, D. Quere, Pearl drops, Europhys. Lett. 47(2) (1999) 220–226.

[77] P. Ustohal, F. Stauffer, T. Dracos, Measurement and modeling of the hydraulic characteristics of unsaturated porous media with mixed wettability, Journal of Contaminant Hydrology 33 (1998) 5–37.

[78] T. Springer, T. Zawodzinski, M. Wilson, S. Gottesfeld, Characterization of polymer electrolyte fuel cells using AC impedance spectroscopy, J. Electrochem. Soc. 143 (1996) 587–599.

[79] J. Song, S. Cha, W. Lee, Optimal composition of polymer electrolyte fuel cell electrodes determined by the AC impedance method, Journal of Power Sources 94 (2001) 78–84.

[80] N. Wagner, W. Schnurnberger, B. Müller, M. Lang, Electrochemical impedance spectra of solid-oxide fuel cells and polymer membrane fuel cells, Electrochimica Acta 43 (1998) 3785–3793.

[81] J. Pukrushpan, A. Stefanopoulou, H. Peng, Modeling and control for PEM fuel cell stack system, in: American Control Conference, Anchorage, 2002, pp. 3117–3122.

[82] J. Golbert, D. Lewin, Model-based control of fuel cells: (1) Regulatory model, J. Power Sources 135 (2004) 135–151.

[83] J. Amphlett, R. Mann, B. Peppley, P. Roberge, A. Rodrigues, A model predicting transient responses of proton exchange membrane fuel cells, J. Power Sources 61 (1996) 183–188.

[84] D. Natarajan, T. Nguyen, A two-dimensional, two-phase, multicomponent, transient model for the cathode of proton exchange membrane fuel cell using conventional gas distributors, J. Electrochem. Soc. 148 (2001) A1324–A1335.

[85] D. Thirumalai, R. White, Mathematical modeling of proton-exchange membrane fuel cell stacks, J. Electrochem. Soc. 144 (1997) 1717–1723.

[86] J. Lee, T. Lalk, Modeling fuel cell stack systems, J. Power Sources 73 (1998) 229–241.

[87] A. Parthasarathy, B. Dave, S. Srinivasan, A. Appleby, The platinum microelectrode/Nafion interface: an electrochemical impedance spectroscopic analysis of oxygen reduction kinetics and Nafion characteristics, J. Electrochem. Soc. 139 (1992) 1634–1640.

[88] C. Harper, Handbook of Materials and Processes for Electronics, McGraw-Hill, New York, 1970.

[89] F. Incropera, D. DeWitt, Fundamentals of Heat and Mass Transfer, Wiley, New York, 1996.

[90] W. Rohsenow, J. Hartnett, E. Ganic, Handbook of Heat Transfer Fundamentals, McGraw-Hill, New York, 1985.

[91] W. Vielstich, A. Lamm, H. Gasteiger, Handbook of Fuel Cells, Wiley, New York, 2003.

Author's publications

Peer-reviewed journal articles

C. Ziegler, H.M. Yu, J.O. Schumacher
Two-phase dynamic modeling of PEMFCs and simulation of cyclo-voltammograms
J. Electrochem. Soc. 152 (2005) A1555-A1567

C. Ziegler, A. Schmitz, M. Tranitz, E. Fontes, J.O. Schumacher
Modeling planar and self-breathing fuel cells for use in electronic devices
J. Electrochem. Soc. 151 (2004) A2028-A2041

A. Schmitz, C. Ziegler, J.O. Schumacher, M. Tranitz, E. Fontes, C. Hebling
Modelling approach for planar self-breathing PEMFC and comparison with experimental results
Fuel Cells 4 (2004) 358-364

H. M. Yu, C. Ziegler, M. Oszcipok, M. Zobel, C. Hebling
Hydrophilicity and hydrophobicity study of catalyst layers in proton exchange membrane fuel cells
Electrochimica Acta, In Press, Corrected Proof, Available online 15 August 2005

C. Ziegler, S. Philipps, J. Niemeyer, J.O. Schumacher
Dynamic modeling of a PEM fuel cell stack
Fuel Cells, Submitted 29 July 2005

Conferences

Conference papers

C. Ziegler, H.M. Yu, J.O. Schumacher
Analysis of the PEM fuel cell dynamics
Proceedings of the 3rd European PEFC Forum, July 4-8, 2005, Lucerne

C. Ziegler, S. Philipps, J. Niemeyer, J.O. Schumacher
Dynamic modeling of a PEM fuel cell stack
Proceedings of the 3rd European PEFC Forum, July 4-8, 2005, Lucerne

A. Schmitz, C. Ziegler, J.O. Schumacher, M. Tranitz, E. Fontes, C. Hebling
Modelling of the planar self-breathing PEMFC
Proceedings of the 2nd European PEFC Forum, Lucerne,
European Fuel Cell Forum, 297-310 (2003)

K. Kühn, M. Ohlberger, J.O. Schumacher, C. Ziegler, R. Klöfkorn
A dynamic two-phase flow model of proton exchange membrane fuel cells
Proceedings of the 2nd European PEFC Forum, Lucerne,
European Fuel Cell Forum, 283-296 (2003)

E. Fontes, D. Gerteisen, A. Hakenjos, K. Kühn, M. Ohlberger, A. Schmitz, J.O. Schumacher, K. Tüber, C. Ziegler
Modelling of proton exchange membrane (PEM) fuel cells
Proceedings of Forum ECHEM 2003, Applied Electrochem., February 26-28, 2003, Vienna

C. Ziegler, M. Tranitz, J.O. Schumacher
A model for planar self-breathing proton exchange membrane fuel cells in FEMLAB
to be published in the Proceedings of the FEMLAB Conference, November 2-4, 2005, Frankfurt am Main

Oral presentations

C. Ziegler, H.M. Yu, J.O. Schumacher
Analysis of the PEM fuel cell dynamics
Oral presentation at 3rd European PEFC Forum
July 4-8, 2005, Lucerne

C. Ziegler, H. M. Yu, J.O. Schumacher
Simulation of cyclo-voltammograms in PEM fuel cells
Oral presentation at Computational Fuel Cell Dynamics III
March 19-24, 2005, Banff International Research Station

C. Ziegler, H. M. Yu, J.O. Schumacher
Investigation of the dynamics of the PEM fuel cell
Oral presentation at Grove Fuel Cell Conference
October 5-7, 2004, Munich

C. Ziegler
Dynamic two-phase modeling of the PEMFC
Oral presentation at 88. Bunsen-Kolloquium
June 14-15, 2004, Kloster Roggenburg

Poster presentations

C. Ziegler, S. Philipps, J. Niemeyer, J.O. Schumacher
Dynamic modeling of a PEM fuel cell stack
Poster presentation at 3rd European PEFC Forum
July 4-8, 2005, Lucerne

A. Schmitz, C. Ziegler, J.O. Schumacher , M. Tranitz, C. Hebling
Characterisation and modelling of planar self-breathing PEMFC
Poster presentation at Grove Fuel Cell Conference
September 24-26, 2003, London

A. Schmitz, S. Wagner, R. Hahn, G. Küstler, C. Ziegler, J.O. Schumacher, C. Hebling
Optimisation of microstructured flowfields for PEMFC
Poster presentation at Grove Fuel Cell Conference
September 24-26, 2003, London

A. Schmitz, C. Ziegler, J.O. Schumacher, M. Tranitz, E. Fontes, C. Hebling
Modelling of planar self-breathing PEMFC
Poster presentation at 2nd European PEFC Forum
June 30 - July 4, 2003, Lucerne

K. Kühn, M. Ohlberger, J.O. Schumacher, C. Ziegler, R. Klöfkorn
A dynamic two-phase flow model of proton exchange membrane fuel cells
Poster presentation at 2nd European PEFC Forum
June 30 - July 4, 2003, Lucerne